A DYNAMICAL STUDY OF 3-DIMENSIONAL OPTICAL ENVELOPE SOLITONS

by

Darran E. Edmundson
B.Sc., University of Waterloo, 1990

A THESIS SUBMITTED IN PARTIAL FULFILLMENT
OF THE REQUIREMENTS FOR THE DEGREE OF
DOCTOR OF PHILOSOPHY
in the Department
of
Physics

SIMON FRASER UNIVERSITY
April 1996

ISBN 0-612-16869-7

The American Physical Society

One Physics Ellipse, College Park, Maryland 20740-3844 (301) 209-3200

March 5, 1996 Code: 950305ED

Darran E. Edmundson
Simon Fraser University
Department of Physics
Burnaby, British Columbia
Canada V5A 1S6

Dear Darran Edmundson:

This is further to your request for permission to use materials from The American Physical Society (APS) journals.

Permission is hereby granted for the one time reproduction -- in print only and as per the requirements indicated below -- of the following figures:

Figure 3, *Phys Rev E*, Vol 50, pg 40-43 (1994)
Figure 10, *Phys Rev A*, Vol 44, pg 636-644 (1991)

to appear in your Ph.D. thesis "A dynamical study of 3-dimensional optical envelope solitons", and a non-exclusive licence for the National Library of Canada to microfilm the figure as part of the thesis and sell copies of the figure as part of the thesis in microform, paper or electronic formats on request.

[**XX**] 1. The following credit line must appear in all copies (please fill in the information in CAPITAL LETTERS): "Reprinted (abstracted) with permission from FULL CITATION. Copyright YEAR The American Physical Society."

[**XX**] 2. NOTE: This permission does not apply to figures, tables, or other materials credited to sources other than the APS.

[**XX**] 3. Obtain the authors' permission to use the material. The author's address can be obtained from the article.

[ ] 4. Remit a permissions fee of $_____. Please make check payable to The American Physical Society. **PLEASE NOTE: PERMISSION IS NOT VALID UNTIL PAYMENT IS RECEIVED.***

Thank you for requesting permission to use materials copyrighted by the APS. Please do not hesitate to contact us should you have further questions.

Maria L. Lebron, Ph.D.
Associate Publisher

THE AUSTRALIAN NATIONAL UNIVERSITY

Dr N.N.Akhmediev
Optical Sciences Center
Research School of Physical Sciences
Institute of Advanced Studies
Canberra ACT 0200
Australia

Telegrams & cables NATUNIV Canberra
Telex 107-19236 (via 021 in Australia only)
Facsimile 06-249 5184
Telephone 06-249 0191 (61-6- outside Australia)
06-249 2430 (Department Secretary)

Email: nna124@rsphy1.anu.edu.au

Mr. Darran E. Edmundson
Department of Physics
Simon Fraser University,
Burnaby, B.C.
Canada V5A 1S6

February 23, 1996.

Re: reproduction of figure from Phys. Rev. A paper

Dear Mr. Edmundson:

This letter is to confirm that I hereby grant permission to reproduce Figure 10 in the paper, J. M. Soto-Crespo, D. R. Heatley, E. M. Wright and N. N. Akhmediev, "Stability of the higher-bound states in a saturable self-focusing medium," Physical Review A, volume 44, pages 636-644 (1991) as part of the introduction to your PhD thesis.

In addition, I also grant the National Library of Canada a non-exlusive licence to microfilm the figure as part of the thesis and to sell copies as part of the thesis in microform, paper or electronic formats on request.

Sincerely yours,

Senior Fellow
Dr. Nail N. Akhmediev

Department of Physics
Simon Fraser University
Burnaby, British Columbia
Canada V5A 1S6

Academic Press Inc.
1250 Sixth Ave.
San Diego, California
U.S.A. 92101

February 7, 1996.

Dear Publisher,

I am a candidate for the Ph.D. degree in physics with a thesis entitled "A dynamical study of three-dimensional optical envelope solitons." As part of my introduction which reviews solitons in nonlinear optics, I wish to reprint several figures from Professor Agrawal's book, "Nonlinear Fiber Optics" (Academic, 1989). Specifically, I wish to reprint Figures 3.6 (page 66), 4.15 (page 98), 5.13 (page 132) and 5.14 (page 133).

I have already contacted Professor Agrawal by electronic mail who writes:

> From: Govind Agrawal <gpa@optics.rochester.edu>
> Date: Fri, 26 Jan 96 13:57:21 EST
> To: dedmunds@sfu.ca
> Subject: Re: reprinting "Nonlinear Fiber Optics" figures ...
>
> Dear Darran,
>
> Thanks for asking. Of course, you can include the figures you asked for in your thesis. Would you mind sending me a reprint of your 1995 paper?
>
> -Govind
>
> ---
>
> Prof. Govind P. Agrawal
> The Institute of Optics
> University of Rochester
> Rochester, NY 14627
>
> Phone: 716-275-4846
> FAX: 716-244-4936
>
> gpa@optics.rochester.edu
>
> ---

Does Academic Press concur? If so, could you please send me a letter of permission that will satisfy the following thesis guidelines, "such letters should not only allow inclusion of the copyrighted material in the thesis but should also allow the National Library of Canada the right to reproduce the thesis including the previously copyrighted material, for loan or sale to interested researchers."

Thank you very much for your attention in this matter.

Sincerely,

PLEASE TURN OVER

Darran E. Edmundson

PERMISSION GRANTED, provided that 1) complete credit is given to the source, including the Academic Press copyright notice; 2) the material to be used has appeared in our publication without credit or acknowledgment to another source; 3) if commercial publication should result, you must contact Academic Press again.

We realize that The National Library of Canada must have permission to sell copies of your thesis, and we agree to this. However, we must point out that we are not giving permission for separate sale of your article.

Cheryl A. Unger
Permissions Department
ACADEMIC PRESS, INC.
Orlando, Fl. 32887

From
Dr. J.S. Aitchison

UNIVERSITY
of
GLASGOW

Mr. Darran E. Edmundson,
Department of Physics,
Simon Fraser University,
Burnaby, B. C.
Canada.
V5A 1S6

ß

28th February, 1996

Re: reproduction of figure from J. Opt. Soc. Am. B paper

Dear Mr. Edmundson:

This letter is to confirm that I hereby grant permission to reproduce Figure 10 in the paper, J.S. Aitchison, Y. Silberberg, A.M. Weiner, D.R. Leaird, M.K. Oliver, J.L. Jackel, E.M. Vogel and P.W.E. Smith, "Spatial optical solitons in planar glass waveguides," Journal of the Optical Society of America B, volume 8, pages 1290-1297 (1991) as part of the introduction to your PhD thesis "A Dynamical Study of 3-Dimensional Optical Envelope Solitons."

In addition, I also grant the National Library of Canada a non-exlusive licence to microfilm the figure as part of the thesis and to sell copies as part of the thesis in microform, paper or electronic formats on request.

Sincerely,

Dr. J. S. Aitchison

DEPARTMENT OF ELECTRONICS AND ELECTRICAL ENGINEERING
Rankine Building, University of Glasgow, Glasgow, G12 8QQ
Head of Department: Prof. P.J.R. Laybourn Ext 4799
Telephone: 041-330-5230 Telex: 777070 UNIGLA Fax: 041-330-4907 E-Mail: S.Aitchison@elec.glasgow.ac.uk

The Australian National University

Optical Sciences Centre
Research School of Physical Sciences and Engineering
Canberra ACT 0200, Australia

Fax: (61)-(6)-249 5184
Telephone: (61)-(6)-249 2430
Telex: 10719236 Via 021
Email: ysk124@rsphysse.anu.edu.au

March 12, 1996

Mr. Darran E. Edmundson
Department of Physics
Simon Fraser University
Burnaby, B.C. Canada V5A 1S6

....

Re: reproduction of figure from Phys. Rev. E paper

Dear Mr. Edmundson:

This letter is to confirm that I hereby grant permission to reproduce Figure 3 in the paper, Yuri S. Kivshar and Yang Xiaoping *"Ring Dark Solitons"*, Physical Review E, **50**, pages 40-43 (1994) as part of the introduction to your PhD thesis.

In addition, I also permit the National Library of Canada to microfilm the figure as part of the thesis and to sell copies as part of the thesis in microform, paper or electronic formats on request.

Sincerely yours,

Yuri Kivshar, Senior Fellow

PARTIAL COPYRIGHT LICENSE

I hereby grant to Simon Fraser University the right to lend my thesis, project or extended essay (the title of which is shown below) to users of the Simon Fraser University Library, and to make partial or single copies only for such users or in response to a request from the library of any other university, or other educational institution, on its own behalf or for one of its users. I further agree that permission for multiple copying of this work for scholarly purposes may be granted by me or the Dean of Graduate Studies. It is understood that copying or publication of this work for financial gain shall not be allowed without my written permission.

Title of Thesis/Project/Extended Essay

A dynamical study of 3-dimensional optical envelope solitons.

Author:
(signature)

Darran Edmundson
(name)

26 March 1996
(date)

APPROVAL

Name: Darran E. Edmundson

Degree: Doctor of Philosophy

Title of thesis: A Dynamical Study of 3-Dimensional Optical Envelope Solitons

Examining Committee: Dr. Jeffrey R. Dahn
Chair

Dr. Richard H. Enns, Senior Supervisor

Dr. Mary-Catherine A. Kropinski, Supervisor

Dr. Sadanand S. Rangnekar, Supervisor

Dr. Klaus E. Rieckhoff, Supervisor

Dr. Keith S. Promislow, Internal Examiner

Dr. Alexander E. Kaplan, External Examiner,
the Johns Hopkins University

Date Approved: 12 March 1996

Abstract

The propagation of plane-polarized, picosecond timescale, three-dimensional optical envelopes travelling in a bulk dispersive dielectric medium which possesses an intensity dependent nonlinear refractive index is governed by the ubiquitous generalized nonlinear Schrödinger equation (GNLSE). It has been known since the early days of nonlinear optics that for the Kerr case characteristic of existing media (where the nonlinearity is proportional to the intensity), solitary wave structures in greater than one dimension are inherently unstable. A manifestation of this instability is that a sufficiently intense spherical pulse can undergo catastrophic collapse, a result which Silberberg envisioned as a method for producing extremely high electric field strengths in a localized volume. In conclusion, however, Silberberg noted that saturation of the nonlinearity could yield a stable self-trapped optical pulse - a "light bullet."

We have successfully numerically propagated light bullets for a number of qualitatively similar nonlinear index of refraction models that obey a simple stability criterion. While collision studies reveal radiative losses, the robustness of these entities pragmatically convinces us to label them solitons (much to the dismay of purists). Several novel effects are presented, some of which have no one-dimensional analogue, including soliton tunnelling and collisions at glancing incidence resulting in spiralling light bullets and eventual fusion into a rotating soliton state.

Our group having a long interest in bistable solitons in optical fibers, we have considered two models which admit bistable light bullets. Bistable solitons have the same energy content but radically different intensity profiles which make them natural carriers of binary information. We present results whereby relatively low intensity diffuse binary zeroes are induced through amplification to switch to higher intensity radially-compact binary ones, the energy difference between states being shed through a sequence of spherical radiative bursts.

To quantitatively understand the nature of the interaction, we have carried out a comprehensive series of numerical scattering experiments between two repulsive π-phase shifted light bullets at various velocities and impact parameters. With negligible radiative losses, we utilize an elastic scattering model and show that the interaction potential is of the Yukawa form which is consistent with an asymptotic expansion of the radial profile. Further, the scattering data scales correctly with velocity and the light bullet energy content plays the role of an effective mass.

Finally, the GNLSE admits higher bound states comprised of a bright central core surrounded by a number of spherical halos. In contrast to the Gaussian-like lowest bound states described above, these halo states are found to be transversely unstable to numerical noise, the spherical shells spontaneously clumping into a number of angularly separated fundamental light bullets. A complicated linear stability analysis of spherical harmonic modes is able to explain the initial stages of the evolution and the symmetry of the broken state.

Acknowledgements

First and foremost, I wish to thank my supervisor, Richard Enns, for five years of generous intellectual and financial support. I hope that the following pages serve as an adequate testament to the success of our relationship.

Computationally, the majority of this research was carried out at the High Performance Computing Centre in Calgary, Alberta under the auspices of the HPCC Graduate Scholarship Program. I am deeply grateful for three years of tremendous technical support. Locally, Academic Computing Services has also provided excellent support and reliable connectivity to the supercomputer centre. A special thanks to Norman Udey (HPCC) and Alan Rothenbush (ACS) for assistance far beyond what a reasonable person would expect.

I wish to thank fellow group member Sandra Eix for a thorough critical reading of the manuscript; that said, any remaining errors and obfuscations are solely my responsibility. Cathie Nielsen and Diarmid Lilly of SFU's Central Duplicating deserve medals for their unwavering assistance in having this document printed. I also wish to thank Dominic Mimnagh for encouraging and supporting my conversion to the OS/2 operating system.

The Internet never seems to be explicitly acknowledged and so I take this opportunity to do so. Whether it be tapping the knowledge of experts around the world or simply connecting to a remote and powerful machine, as a tool for doing research "the Net" is unsurpassed. This thesis would not have been possible without it.

Finally, I wish to thank my wife Kelley whose emotional support has increasingly sustained me over the past half-decade; I'm not sure I could have done it alone.

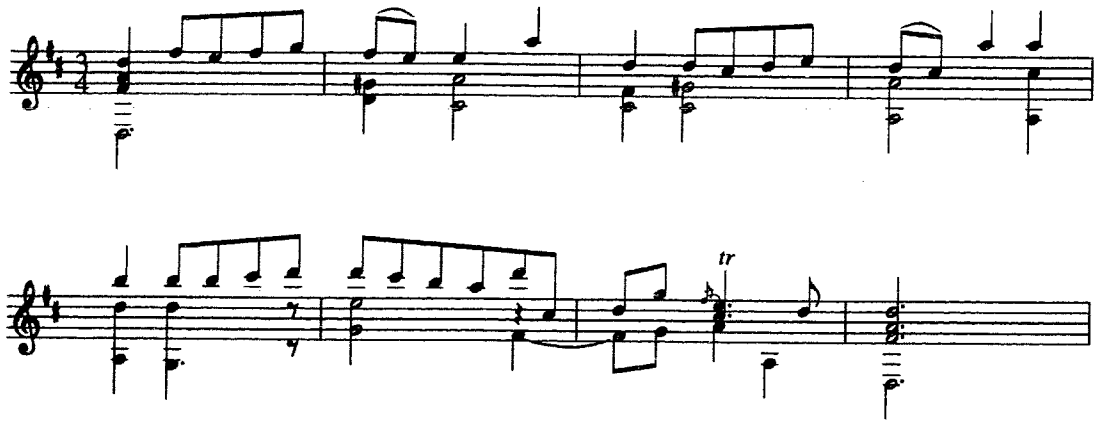

Sylvius Leopold Weiss (1686-1750)

Contents

List of Tables

List of Figures

Chapter 1

Introduction

In a recent issue of *Physics Today* [Kr91], the President of the American Physical Society stated "in my research over the past two decades, I have been fascinated by a set of developments in nonlinear science. A particularly remarkable manifestation is the entirely counterintuitive excitation called the soliton . . ." Indeed solitons, localized nonlinear waves possessing striking stability properties that allow them to propagate without change and survive massive perturbations in the form of collisions, play an important role in modern physics. The soliton has been invoked to explain such diverse phenomena as:

- The famous Fermi-Pasta-Ulam paradox [Fo92] wherein a nonlinearly coupled lattice of particles does not display the "expected" equipartition of energy among available modes.
- Magnetohydrodynamic and ion-acoustic waves in a plasma [In90].
- Energy storage and transport in proteins via the Davydov soliton [Cr94].
- The propagation of short laser pulses in optical fibers over long distances with negligible shape change [Ha73a, Mo80].
- The long lived "giant red spot" in the highly turbulent Jovian atmosphere [An86].

The most well-known system possessing soliton solutions is the Korteweg-de Vries (KdV) equation, derived at the end of the 19th century to model the 1834 observations of Scottish naval engineer J. Scott-Russell. In the less formal style of scientific reporting of the day, Scott-Russell wrote [Sc1845],

> I was observing the motion of a boat which was rapidly drawn along a narrow channel by a pair of horses, when the boat suddenly stopped – not so the mass of water in the channel which it had put in motion; it accumulated round the prow of the vessel in a state of violent agitation, then suddenly leaving it behind, rolled forward with great velocity, assuming the form of a large solitary elevation, a rounded smooth and well-defined heap of water, which continued its course along the channel apparently without change of form or diminution of speed. I followed it on horseback, and overtook it still rolling on at a rate of some eight or nine miles an hour, preserving its original figure some thirty feet long and a foot to a foot and a half in height. Its height gradually diminished, and after a chase of one or two miles I lost it in the windings of the channel. Such, in the month of August 1834, was my first chance[1] interview with that singular and beautiful phenomenon ...

For nearly seventy years, an article of faith in the physics community was that a collision involving two solitary waves would destroy the otherwise stable input pulses due to the nonlinear nature of the interaction. It was not until 1965 that Norman Zabusky and Martin Kruskal numerically discovered [Za65] that KdV solitary waves maintained their identity following collisions (Figure 1.1), the incredulous duo reporting that "[h]ere we have a nonlinear physical process in which interacting localized pulses do not scatter irreversibly." Zabusky and Kruskal coined the term "soliton" to reflect the particle-like nature of these robust travelling solitary waves. In 1967, this numerical curiosity was placed on a firm mathematical basis with Gardner *et*

[1]Apparently, luck was on Scott-Russell's side that fateful day. A 1984 attempt to repeat the experiment under similar conditions and at the same spot was a complete failure [In90]. However, a 1995 attempt was successful as described on the World Wide Web at <URL:http://www.ma.hw.ac.uk/solitons/press.html>.

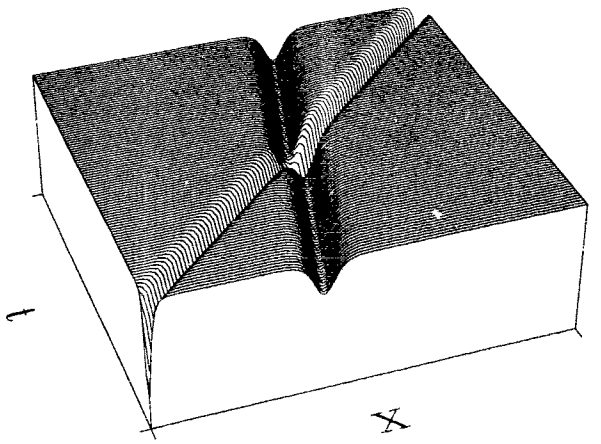

Figure 1.1: Two-soliton solution to the Korteweg-de Vries equation. (Of special interest is the phase shift at the crossing point.)

al.'s discovery [Ga67] of the inverse-scattering-transform (IST) method and its use in analytically solving the KdV equation for any finite number of interacting solitons.

Though it is usually avoided due to its inherent intractability, nonlinearity, embodied by the canonical Navier-Stokes equation, has always been an essential ingredient of hydrodynamics. In contrast, the field of classical optics, governed by Maxwell's equations, has for most of its life operated quite nicely in the linear regime. For a hundred years, due to the relatively weak electromagnetic field strengths available, analogues of the turbulence, complexity and downright nastiness that are quintessential features of a non-laminar fluid were all but absent in the world of light interacting with matter. However, with the advent of the laser as a source of coherent high-intensity radiation, this changed and physicists were treated to a wealth of nonlinear effects including harmonic generation, self-focusing, nonlinearly induced birefringence, self-phase modulation, etc.

Self-focusing, the NLSE and temporal solitons

In 1964, Chiao *et al.* [Ch64] provided a physically insightful but somewhat mathematically crude explanation for the "extremely-thin, long streaks of ionization spots and damage that sometimes occur in optical materials in which an intense laser beam is focused." Beyond the focal point, it was typical to find a several centimeter-long

straight filament of bubbles with a width of only a few optical wavelengths - under linear optics, such a squeezed beam would rapidly spread due to the effects of diffraction. However, by proposing that the refractive index n was dependent on the field strength

$$n = n_0 + n_2|E|^2 \tag{1.1}$$

(this fundamental form being known as the Kerr nonlinearity), Chiao *et al.* demonstrated that above a certain critical input power, a diffracting beam of arbitrary diameter would become self-trapped due to the induced increased refractive index across the beam profile. The stability of these solutions to small perturbations was not addressed. Soon after, Talanov [Ta65] and Kelley [Ke65] showed that the slowly-varying paraxial transverse beam envelope E was governed by the nonlinear Schrödinger equation (NLSE)

$$i\frac{\partial E}{\partial z} + \nabla^2 E + |E|^2 E = 0 \tag{1.2}$$

where ∇^2 is the transverse Laplacian. Above a critical power threshold, it was found that the cylindrical beam was unstable and would catastrophically collapse. Of course, at some point during the collapse process the physical approximations of the NLSE break down,[2] the collapse halts, and one or more stable filaments of light are formed, the number of filaments depending on the initial power [Ch66].

A key development in nonlinear optics came with Zakharov and Shabat's discovery [Za72] via the IST method that a one-dimensional version of the NLSE is a completely integrable system possessing multiple soliton solutions. As shown in Figure 1.2, in addition to initially infinitely separated solitons, one finds that initially overlapping solitary wave profiles also exhibit soliton-like behaviour. In Zakharov and Shabat's seminal work, it was pointed out for the first time that the NLSE also governs the temporal propagation of a quasi-monochromatic one-dimensional optical envelope in a dispersive medium possessing an instantaneous cubic nonlinearity. Almost twenty years later, this result - that the dynamics of one-dimensional spatial solitons are identical to the dynamics of one-dimensional temporal solitons - was exploited by

[2]See Ref. [Fe88] for an entry point into the literature on the topic of the NLSE's validity with regards to the self-focusing problem.

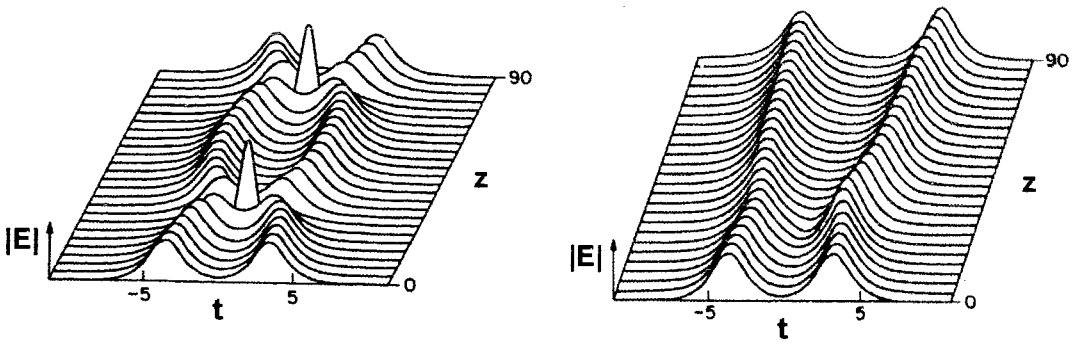

(a) (b)

Figure 1.2: The dynamics of overlapping NLSE solitons. (a) Initially in-phase solitons demonstrate lossless periodic collapse. (b) π-phase shifted solitons repulse. From Ref. [Ag89], by permission.

Yaron Silberberg of Bellcore in a paper [Si90] that provided the impetus for this thesis (a point that will be addressed in due course).

In 1973, Hasegawa and Tappert [Ha73a, Ha73b] showed theoretically and numerically that the one-dimensional NLSE

$$i\frac{\partial E}{\partial z} \pm \frac{1}{2}\frac{\partial^2 E}{\partial t^2} + |E|^2 E = 0 \tag{1.3}$$

described the propagation of optical pulses in low-loss dispersive dielectric fibers. Here, the plus and minus sign govern propagation in the anomalous and normal dispersion regimes respectively.[3] As will be discussed in Chapter 2, the NLSE is obtained from Maxwell's equations under certain assumptions. A key assumption is that the field is polarized in a specific direction which allows the vector wave equation to be written as a one-dimensional scalar partial differential equation (PDE).

Although Zakharov and Shabat had already analytically shown the existence of

[3]This terminology is explained in Chapter 2. Suffice it to say that there is nothing particularly "anomalous" about the former regime; dispersion of both types generally leads to temporal spreading of the wavepacket.

soliton solutions to Eq. (1.3) in the case of anomalous dispersion, experimental verification of the predicted soliton transmission did not occur until 1980 due to the exceedingly high loss in these early fibers. At this time, Mollenauer, Stolen, and Gordon [Mo80] reported the successful propagation of 7 picosecond pulses at the anomalously dispersive wavelength of 1.5 μm through 700 m of single-mode silica fiber with negligible shape change. Below the critical power necessary to form the fundamental soliton, Gaussian-like input pulses spread due to dispersion. Above this threshold, pulse narrowing occurred to form the characteristic hyperbolic-secant soliton profile consistent with the input power. In addition to such localized pulses with nonvarying temporal profiles, the NLSE also admits soliton solutions with periodic behaviour known as "breather modes." Breathers, characterized by pulses that alternate as they propagate between high-intensity spikes and relatively low-intensity pulses with varying numbers of side-lobes, contain considerably more power than the fundamental soliton. As expected, Mollenauer *et al.* experimentally witnessed higher-order soliton formation (breathers) when they increased the input power.

This experimental success and the obvious technological benefits of temporal solitons as information carriers in long-distance communication systems provoked a flood of work on one-dimensional temporal solitons in optical fibers, the quantity of work in this area being so vast that nonlinear fiber optics now qualifies as a field in its own right. As an applied example, recently workers at BellCore succeeded in 5 Gigabit/second soliton transmission through 10,000 km of fiber using erbium doped fiber amplifiers to compensate for the low but non-negligible loss [Mo88].

Optical switching and bistability

Another application of the temporal soliton in optical fibers is the possibility of producing all-optical digital logic devices. Electronic transistor-transistor logic (TTL) digital circuits utilize a signal generally in the vicinity of 3.6 Volts to represent a logic '1' and a voltage in the neighbourhood of 0 Volts to represent a logic '0'. The obvious optical parallel is to use a soliton or gap (zero background) to represent a 1 or 0 respectively such that a string of solitons and gaps would encode a binary message.

One method of switching utilizes evanescent coupling between the input fiber and a signal fiber carrying a retarded pulse that drags on the input pulse, shifting it from its expected location and leaving a gap. Unfortunately, such one-dimensional dragging gates typically are sensitive to minute phase differences between the pulses.

A major drawback of the preceding communication and digital switching schemes is that the logic '0' (representing, on average, half of the information) is carried by something that, by definition, is nonexistent. Of course, this necessitates a highly accurate synchronous system whereby gaps can be presumed to represent binary zeroes.

An alternative approach is to use two different soliton shapes to represent the binary logic states. For example, one could use a short squat soliton to represent a logic '0' and a tall narrow soliton to represent a logic '1'. While (above the power threshold for soliton formation) Kerr media admit a continuous spectrum of fundamental soliton shapes, such solutions are not suitable for two reasons: (i) for sufficient peak-height contrast between the logic states, the tall '1' soliton will have significantly greater energy content than the short '0' soliton, and (ii) as a continuous spectrum of stable intermediate profiles is available, there is no natural division between the two states. However, as Kaplan has demonstrated [Ka85a, Ka85b], both of these deficiencies can be removed by considering non-Kerr media of the form

$$n = n_0 + n_2 F(|E|^2) \tag{1.4}$$

where $F(|E|^2)$ is a nonlinear refractive index function, appropriately chosen to yield *bistable* solitary waves. Bistable solitary waves have the same energy content but radically different profiles.[4] In addition to the attractive property that the two logic states have equal energy content, a natural result of bistability is the existence of an unstable intermediate regime separating the low and high states. While not the focus of this thesis, bistable models are considered and are dealt with in some detail in Chapter 3 on refractive index model construction.

At this point, a brief semantic diversion is in order. An immediate consequence of

[4]Recently, a second definition of bistability has been introduced into the literature [Ga91, Ei93] corresponding to pulses of equal duration but different peak intensities.

considering a non-Kerr medium is that NLSE soliton solutions are not solutions to the modified equation; thus, one no longer has analytical proof of soliton existence. While the new solitary waves are often stable to small perturbations, massive perturbations in the form of collisions (see, e.g., Refs. [En87a, En87b]) frequently yield radiative losses. These semi-stable nonlinear waves are *not* solitons in the strict mathematical sense. However, despite the radiative losses, one often finds that the pulses survive collisions, thus behaving in a quasi-soliton fashion. Despite the protestations of a few purists, the prefix "quasi" is usually dropped in the research literature and such semi-stable entities have pragmatically come to be known simply as solitons.

While the unfortunate price to pay for bistability is the sacrifice of the integrable Kerr NLSE characteristic of many existing media, physical intuition suggests that such an unbounded nonlinearity must saturate at high field strengths,[5] leading one to consider a model of the form

$$F(I=|E|^2) = \frac{I}{1+I/I_{\text{sat}}} \tag{1.5}$$

which is Kerr-like at low intensity I and saturates at the value I_{sat}. Materials with saturable nonlinearities are known to exist [Co91] and Enns and Edmundson [En93] have recently shown how an appropriate mixture of saturable models can produce media which support bistable solitons.

While the stable propagation of bistable pulses is eminently desirable for long distance communication purposes, another important application is the creation of all-optical digital logic circuits. For example, a NOT gate (inverter) should take low-state '0' solitons as input and produce high-state '1' solitons as output, and vice-versa. It has been shown that up and down-switching between bistable soliton states can be induced by amplification or damping of the input [En92b]. More recently, numerical and theoretical work has shown that passive NOT and AND gates can be created by using evanescent coupling between adjacent fibers [Ei96].

[5] Of course, there is an alternative to saturation: dielectric breakdown and irreversible damage to the medium.

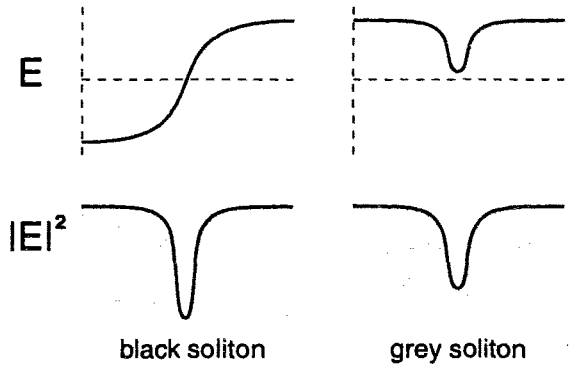

Figure 1.3: Theoretical black and grey soliton profiles along with their respective intensity profiles.

Despite the obvious technological applications of bistable solitons, to date they remain experimentally unverified, awaiting the necessary advances in materials science.

Dark temporal solitons

To this point, all of the solitons presented are qualitatively similar, consisting of a localized Gaussian-like[6] pulse on a zero background. In optics, this qualitative shape is known as a bright soliton. However, in the case of normal dispersion, the NLSE becomes

$$i\frac{\partial E}{\partial z} - \frac{1}{2}\frac{\partial^2 E}{\partial t^2} + |E|^2 E = 0 \tag{1.6}$$

which permits [Za73, Ha73b] a different class of soliton solutions. Figure 1.3 schematically shows such solutions for the field E along with their respective intensity patterns $|E|^2$. Referring to the intensity profiles, such localized depressions in a constant intensity background are known as grey or black dark solitary waves depending on whether or not the intensity dips to zero at its lowest point. An obvious practical drawback of dark solitons is that the integrated intensity of such a pulse is infinite. Due to the intrinsic difficulty of creating such input profiles, definitive[7] experimental verification of the dark soliton did not occur until 1988 when Weiner *et al.* [We88] propagated

[6] "Gaussian-like" is meant to be taken extremely loosely and denote any profile that is bright at the origin and decreases monotonically and asymptotically to zero. Unfortunately, "sech-like," a better approximation, hasn't yet become part of the vernacular.

[7] Previous workers [Em87, Kr88] had suggestive evidence for dark and grey soliton propagation.

185 femtosecond dark pulses riding on a bright 1-4 picosecond Gaussian background in a normally dispersive single-mode fiber.

Building on their work in the bright case, Enns and Mulder [En89] have considered modifications to the NLSE necessary to produce bistable dark solitary waves. The soliton character of these entities was confirmed through numerical switching simulations.

Higher-order corrections to the NLSE

As shown by the experimental successes in the bright and dark cases, the one-dimensional NLSE accurately governs the propagation of picosecond pulses in dispersive fibers possessing a Kerr nonlinearity. However, with the inevitable push towards progressively shorter pulses, higher-order corrections to the NLSE must be considered. In 1987, Kodama and Hasegawa [Ko87] used a perturbative approach to rigorously[8] derive the generalized NLSE,

$$i\frac{\partial E}{\partial z} \pm \frac{1}{2}\frac{\partial^2 E}{\partial t^2} + |E|^2 E - \frac{i}{6}\beta_3 \frac{\partial^3 E}{\partial t^3} + i a_1 \frac{\partial}{\partial t}\left(|E|^2 E\right) - a_2 E \frac{\partial |E|^2}{\partial t} = i\Gamma E \qquad (1.7)$$

The term proportional to β_3 results from including higher-order dispersion and becomes important both in the picosecond regime when operating with pulses centred at the zero dispersion wavelength, and in the propagation of ultra-short (femtosecond) pulses. As shown in Figure 1.4(a), it has the effect of creating asymmetry in the pulse with the eventual formation of diminishing oscillatory sidelobes on the leading or trailing edge of the pulse, depending on the sign of β_3 [Ag89]. The term proportional to a_1 results from considering time dependence of the nonlinear polarization. It is a "shock" term, and, as shown in Figure 1.4(b), results in self-steepening of the pulse edge [Ag89]. The final term on the left side of Eq. (1.7) results from considering noninstantaneous nonlinear response and is responsible for self-frequency shift of the pulse [Go86]. Physically, this term reflects the transfer of energy from one frequency

[8]The general structure of this equation follows quite naturally from keeping higher-order terms in the more transparent derivation of Chapter 2.

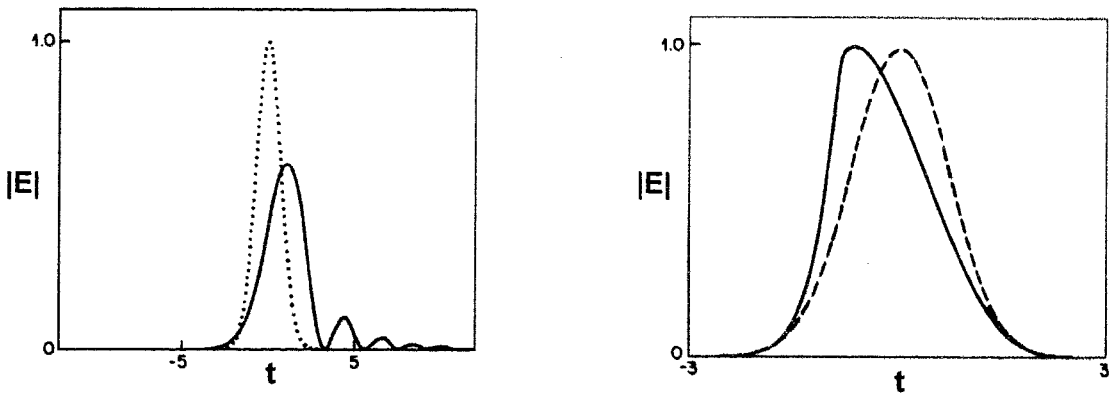

(a) Higher order dispersion leads to oscillatory side-lobe formation.

(b) "Shock" term leads to self-steepening of the pulse edge.

Figure 1.4: Typical effect of higher order terms in the NLSE on an originally Gaussian input pulse (dashed curve). Solid curve: field profile at a later time. From Ref. [Ag89], by permission.

component of the pulse to a lower frequency component, the energy difference being carried off by an optical or acoustical phonon. With $\Gamma < 0$, the term on the right-hand side is a phenomenological damping term used to account for energy losses due to both Rayleigh scattering and other loss mechanisms during pulse propagation.

Spatial solitons

As stated, it has been known since 1972 that the NLSE admits soliton solutions. Perhaps because of the technological ramifications, an enormous amount of effort was subsequently expended on the study of temporal solitons in optical fibers, ignoring the fact that the NLSE was originally derived to explain two-dimensional *spatial* self-focusing. The NLSE describing the evolution of the beam front of a one-dimensional spatial envelope E is

$$i\frac{\partial E}{\partial z} + \frac{1}{2}\frac{\partial^2 E}{\partial x^2} \pm |E|^2 E = 0 \tag{1.8}$$

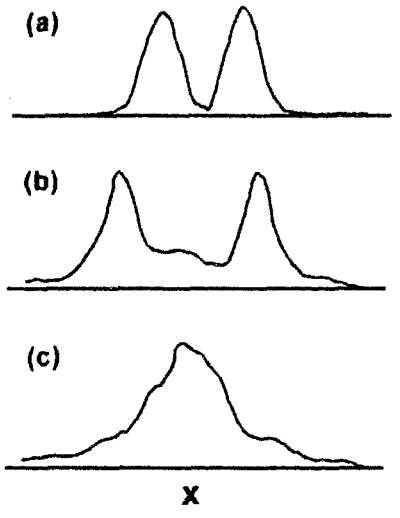

Figure 1.5: Experimental observation of spatial solitons in a planar glass waveguide. (a) Overlapping initial input solitons. (b) Repulsion in the case of a π phase difference. (c) Attractive solitons with zero phase shift. Scale width is 100μm. Compare, e.g., with theoretical predictions shown in Figure 1.2. From Ref. [Ai90], by permission.

where x is the transverse spatial coordinate, z is the beam propagation direction and the plus and minus sign of the final term refers to the case of a self-focusing or self-defocusing nonlinearity, respectively. While two-dimensional beam propagation in a Kerr medium was known to be unstable from the early days of nonlinear optics, confinement to one transverse spatial coordinate should yield spatial analogues of temporal solitons. A bright spatial soliton is a self-trapped beam that maintains a perfect balance between the spreading effect of diffraction and the effect of self-focusing due to the induced increased index of refraction. Conversely, a dark spatial soliton consists of a dip in a constant intensity background and survives as a stable trapped state due to a balance between diffraction and self-defocusing. It was not until 1985 that experimentalists observed bright spatial solitons in a transversely quasi-one-dimensional system, namely a multi-mode liquid CS_2 filled planar waveguide [Ba85, Ma88a, Ma88b]. More recently, a comprehensive set of experiments on interacting spatial solitons in a planar glass waveguide was reported [Ai90]. Figure 1.5 shows the experimentally observed intensity patterns for two initially overlapping spatial solitons (top) with a π-phase shift leading to repulsion (middle) and no phase shift leading to periodic collapse (bottom). These examples are extremely important because they demonstrate the novel possibility of "light guiding light" whereby one light beam can be steered with another as part of an all-optical device. One's intuition with respect

to such interactions can be led by recourse to a simple Snell's law-type argument. In the early stages of periodic collapse, each soliton "sees" an index of refraction gradient due to the presence of the other pulse's tail, the beam bending in the direction of the increased index. Of course, complete reemergence of each pulse from the nonlinear collapse with no radiative release is surprising and can only be understood in terms of soliton theory. In the case of a π-phase difference, the presence of the other pulse decreases the local index of refraction and the solitons repel one another.

In 1991, one-dimensional spatial dark solitons[9] were observed by Swartzlander *et al.* [Sw91] in the transverse profile of a laser beam that passes through a wire mesh and self-defocusing medium. A striking feature of this experiment is that the stable dark soliton stripes which develop evolve from a decidedly non-soliton initial state; the wire mesh used to mask the uniform input beam creates crude dark stripes which evolve to the one-dimensional NLSE dark soliton profiles. That is, it is often *not* necessary to begin with an exact soliton input profile, instead the soliton acts as an attractor for input states that are suitably nearby. Such attractor-like behaviour is very important from a practical point of view where a reasonable degree of system robustness to initial perturbations is desired.[10]

Unstable Kerr beams revisited

Solitons in the optical systems considered so far share the common trait that the electric field oscillating beneath the envelope is plane-polarized, i.e., as depicted in Figure 1.6(a), the electric field is assumed to oscillate in a fixed direction. This is not a physical requirement but rather, as mentioned earlier, a means of reducing the vector wave equation to a more tractable scalar form from which the relatively simple (soliton-admitting) NLSE eventually emerges.

Recall that the two-dimensional plane-polarized bright circular beam in a Kerr medium was known to be unstable from the early days of nonlinear optics. In 1992, Snyder *et al.* [Sn92] considered alternative reductive polarizations of the circularly

[9]See, e.g., Ref. [Ki93] for a review of spatial dark solitons.

[10]This issue was recently addressed in the context of this thesis by McLeod and *et al.* [Mc95].

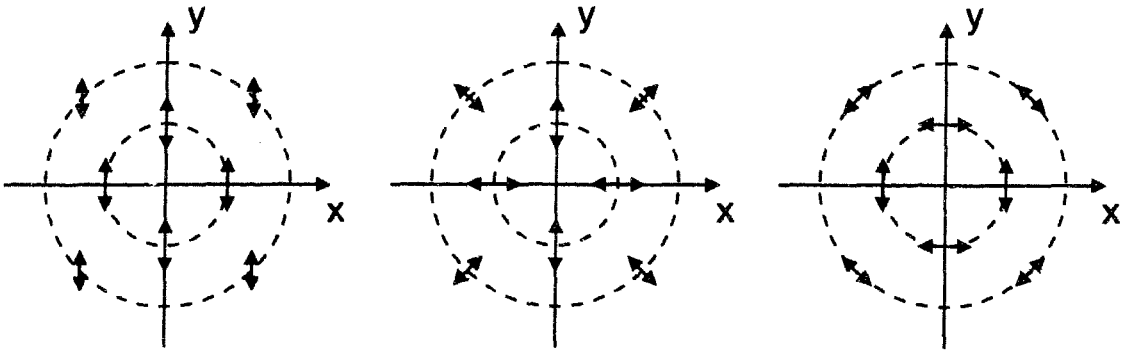

Figure 1.6: Schematic representations of three reductive electric field polarizations for the dark beam. (a) plane polarized. (b) radially polarized. (c) azimuthally polarized. (For clarity, only sample polarizations at two beam radii are shown.)

symmetric beam, two of which being the radially polarized TM_{01} mode and the azimuthally polarized TE_{01} mode shown schematically in Figure 1.6 (b) and (c) respectively. While no mathematical restrictions are placed on the resulting envelope equation, uniqueness of the underlying vector field requires that the envelope be zero-valued at the origin. Thus, with the field being "black" at the beam centre, it is natural to look for a dark solitary wave profile. Such profiles exist and, due to the non-plane polarization, are (in staunch contrast to the bright case) found to be stable. These dark optical vortex solitons were subsequently observed experimentally by Swartzlander and Law [Sw92]. As Snyder and co-workers comment, this is a very important result because it "paves the way for numerous [greater than one spatial-dimensional] all-optical devices in which light itself directs and manipulates light in a bulk [Kerr] material without any intervening structures." As an example, they envision a strong dark pump beam guiding a weak signal beam through an ordinarily isotropic uniform bulk medium by virtue of the (linear) waveguide it induces.

In 1994, Kivshar and Yang [Ki94] theoretically predicted the existence of stable plane-polarized two-dimensional structures for the Kerr nonlinearity characteristic of existing media. It has been known since 1988 that dark soliton strips are unstable

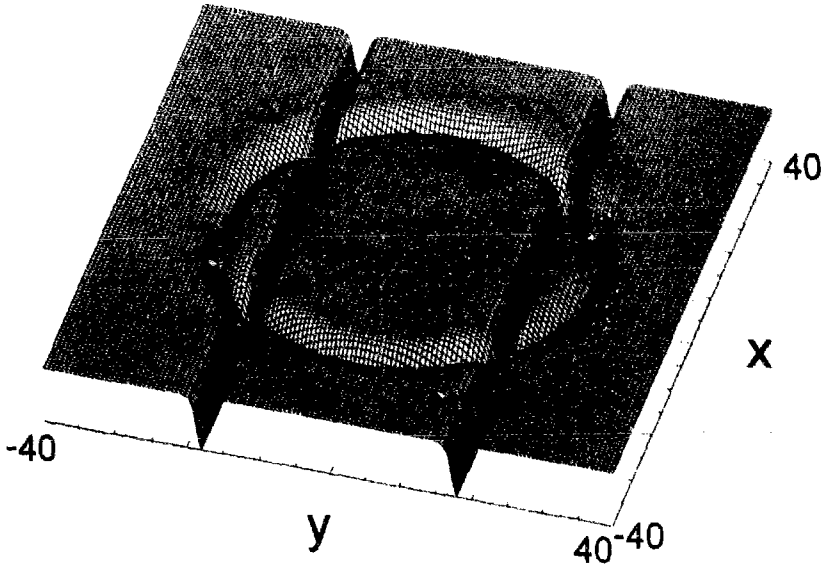

Figure 1.7: Interaction of a ring dark solitary wave with a pair of dark-soliton strips. From Ref. [Ki94], by permission.

to long-wavelength perturbations [Ku88], later numerical simulations [Mc93, La93] revealing that the strips decay into a sequence of optical vortex solitons of opposite polarities. Kivshar and Yang realized that this transverse instability could potentially be averted by forming a closed dark loop with a circumference less than the critically unstable wavelength. The authors found that in the small-amplitude limit, the loop is governed by the cylindrical KdV equation which is known to admit cylindrical and spherical pulse solitons [Ma74]. As shown in Figure 1.7, numerical simulations of the governing wave equation reveal the ring dark soliton to be a stable entity, undergoing elastic collisions with dark soliton strips. This exciting new Kerr spatial soliton was recently observed experimentally by Baluschev and co-workers [Ba95].

Stability in higher dimensions: Non-Kerr media

An alternative method of creating stable two (and higher) dimensional spatial structures is to allow for deviations from Kerr-like behaviour. For example, while it has long been known in plasma physics that saturation of the nonlinearity can induce radial stability for otherwise unstable systems [Ka75, Wi75, In90], only recently has this principle been applied to the types of optical systems discussed above.

As shown by Snyder *et al.* [Sn91, Po91], the unstable bright circular beam originally considered in the early days of nonlinear optics [Ch64, Ke65] becomes theoretically stable when the nonlinearity is sufficiently saturable. In fact, as will be shown in Chapter 3, the precise form of the nonlinearity is unimportant, a simple stability criterion and set of scaling laws [Ko73, Wi75, La84] implying that *any* model displaying suitable saturation at high intensities will yield radially stable bound states. (This criterion does not guarantee stability against transverse perturbations or collisions.)

In addition to the now familiar bright circular beam that is maximal at the beam centre and decreases monotonically with increasing radius, there also exists higher bound states that consist of a bright central spot surrounded by a number of concentric bright rings. Soto-Crespo and co-workers [So91] demonstrated by means of linear stability analysis and numerical experiment that such states are unstable to angular perturbations, the initially symmetric rings breaking up into a number of equispaced filaments (Figure 1.8). Very recently, Atai *et al.* [At94] considered the closely related problem of an azimuthally polarized field with a dark spot surrounded by rings of varying intensities in a saturable medium; not surprisingly, this system was also found to be unstable to transverse perturbations.

Self-trapped three-dimensional pulses: light bullets

In his Ph.D. dissertation [Za66], V. Zakharov pointed out the now well-known result that the dynamics of one-dimensional spatial pulses are identical to those of one-dimensional temporal envelopes, both being governed by the nonlinear Schrödinger equation. As stated in a recent review paper [Mc95], "one simply needs to replace

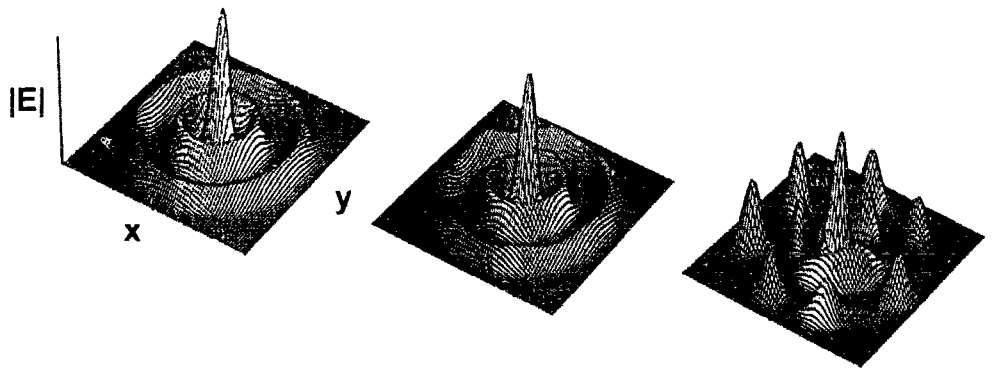

Figure 1.8: Transverse instability of the 2nd higher bound state in a saturable self-focusing medium. From Ref. [So91], by permission.

the spatial quantities of nonlinear self-focusing, diffraction, and spatial frequency (angle) with their temporal analogues of nonlinear pulse compression, anomalous group-velocity dispersion, and temporal frequency (color)." Thus, it is surprising that twenty years passed before it was proposed [Ma88c, Si90] that these effects be considered in tandem, viz.

$$i\frac{\partial E}{\partial z} + \frac{1}{2}\left(\frac{\partial^2 E}{\partial t^2} + \frac{\partial^2 E}{\partial x^2} + \frac{\partial^2 E}{\partial y^2}\right) + |E|^2 E = 0 \tag{1.9}$$

to govern the propagation of plane-polarized three-dimensional envelopes in an anomalously dispersive bulk medium. This remarkable equation, and its generalization to an arbitrary refractive index function, permits solitary waves solutions that are self-trapped both in space and time. However, as with the bright case in two-dimensions, Kerr solitary waves are found to be unstable. Above a critical power, Yaron Silberberg predicted [Si90] that a spherical localized pulse could symmetrically collapse in space and time under the combined effects of self-focusing and temporal nonlinear compression. While mathematically the collapse is unbounded, physically the assumptions used in deriving the NLSE will break down and either higher-order effects or dielectric breakdown will avert the singularity. Silberberg did not attempt to avoid this collapse, envisioning it as a means of producing exceptionally high, localized, electric fields. In conclusion though, Silberberg did note that "saturation of the nonlinear

index [could] bound the collapse and lead to the formation of stable, nondiffracting and nondispersing pulses: light bullets."

Soon afterward, Blagoeva *et al.* [Bl91] published the first theoretical and numerical work on light bullets. The system they proposed consisted of signal pulses travelling down a waveguide induced by a relatively large and powerful pump pulse. While such stable localized three-dimensional signal pulses are confined in time and space, they are not *self*-trapped. In addition, such a configuration does not allow non-zero impact parameter bullet-bullet interactions, copropagation of different sized pulses, etc. In a sense, this work is a generalization of Snyder's proposal for one beam steering another; however, in this case the weak signal beam is a finite duration pulse.

Light bullets, the topic of this thesis, have been the focus of much theoretical work over the past five years. Nail Akhmediev and co-workers [Ak92] predicted that a continuous-wave bright beam travelling in a bulk saturable medium would be susceptible to a temporal modulation instability which would likely cause the formation of a train of light bullets - the optical machine gun - a prediction later confirmed by numerical experiment [Ak93a].

Enns and Rangnekar [En92a], following up on Silberberg's stability conjecture and their earlier work on one-dimensional bistability, devised two non-Kerr models that would support bistable light bullets, trapped three-dimensional pulses with the same energy content but radically different radial profiles. In the first numerical confirmation of these objects, Edmundson and Enns (Ref. [Ed92] and Chapter 4) demonstrated the soliton-like nature of colliding light bullets and also induced a low-state bistable light bullet to switch to a high-state bullet.

Recall that in the normal dispersion regime, the one-dimensional NLSE admits a temporal dark soliton. Hayata and Koshiba [Ha93] considered Eq. (1.9) with normal dispersion and derived an approximate form for a *symbion* solitary wave, a mixed separable profile consisting of a dark soliton in the temporal direction multiplied by a trapped two-dimensional bright beam in the spatial direction. The topic of symbion stability was not addressed nor were symbions propagated numerically - they are undoubtedly unstable in the Kerr case.

Edmundson and Enns reported a set of novel numerical experiments (Ref. [Ed93]

and Chapter 4), some of which have no one-dimensional analogue. Making use of the disparate sizes of bistable light bullets, soliton tunnelling was observed whereby a small high-state bullet burrows through a much larger low-state bullet. In addition, breaking the cylindrical symmetry, collisions were reported at non-zero impact parameter.

In early 1995, generalizing the work of Snyder *et al.* [Sn92] who predicted stable black beams with azimuthal polarization in two-dimensional Kerr media, Chen and Atai [Ch95] discovered the analogous dark optical bullet in an anomalously-dispersive self-defocusing bulk Kerr medium. As in two dimensions (and in stark contrast to the bright Kerr case), these entities are theoretically predicted to be stable.

In one dimension, introduction of a π-phase difference between solitons leads to repulsion (refer back to Figure 1.2(b)). The same is true of light bullets with the exception that one is not confined to "head-on" collisions. Edmundson and Enns [Ed95] performed a series of scattering experiments at various impact parameters and incident velocities for the modified GNLSE with a saturable nonlinearity. As discussed in Chapter 5, this scattering data can be used to successfully extract the force law between two interacting bullets with overlapping tails.

In addition to the fundamental bound state, there also exist halo states comprised of a bright central core surrounded by a number of bright spherical halos. As discussed in Chapter 6 and Ref. [Ed96], this author has recently confirmed that these states are unstable to transverse perturbations. By virtue of the structure of the NLSE in three dimensions (and in contrast to the situation in two dimensions), the stability analysis yields the result that entire families of modes are unstable, a result that leads to complex pattern formation. These findings were corroborated by direct simulation of the governing envelope equation.

Finally, the possible technological applications of one-dimensional temporal solitons (long distance communications, fiber-coupler logic gates) and spatial solitons (optical storage, all-optical switches) are well known and are likely the impetus for much of the work[11] that has transpired in the last two decades. On the other hand, the applications for light bullets are not so obvious. In an exciting new paper entitled

[11] Or, at the very least, the source of funding.

"(3+1)-dimensional optical soliton dragging logic," McLeod and co-workers [Mc95] make a strong case for the use of light bullets as the basic element of all-optical digital logic gates. By considering the interaction of orthogonally-polarized bullets, it is shown that a phase-insensitive high-gain cascadable gate can be produced. In conclusion, these workers optimistically opine that "the possibility of constructing all-optical, light-bullet dragging logic circuits with millions of gates operating at (terahertz) clock speeds is strong motivation for the continued materials, theoretical, and systems research necessary to realize these devices."

In the chapters that follow, we will present a detailed account of our contributions to the light bullet problem. First, however, we begin with a physically transparent derivation of the (3+1)-dimensional generalized nonlinear Schrödinger equation and the numerical method used for its solution.

Chapter 2

Optical envelope propagation in bulk media

As can be gathered from the introduction, the generalized nonlinear Schrödinger equation (GNLSE) plays a central role in nonlinear optics, describing the evolution of plane, radial, and azimuthally polarized envelopes in one, two, and three-dimensional systems possessing an intensity dependent refractive index. The aim of this chapter is to present a concise and physically transparent derivation of the three-dimensional GNLSE, to understand the general effect of the linear and nonlinear contributions, and to develop a beam propagation method necessary for its numerical solution.

2.1 Derivation of the propagation equation

Due to its importance, a derivation of the NLSE is available in any self-respecting nonlinear optics textbook (e.g., see Refs. [Ag89, Bo92, Ne92]). While a thorough treatment that rigorously takes into account higher order effects was recently published by Kodama and Hasegawa [Ko87], the more concise derivation presented here follows that of McLeod and co-workers [Mc95].

Naturally enough, one begins with Maxwell's equations in SI units

$$\nabla \times \vec{\mathcal{E}} = -\frac{\partial \vec{\mathcal{B}}}{\partial T} \tag{2.1}$$

$$\nabla \times \vec{\mathcal{H}} = \frac{\partial \vec{\mathcal{D}}}{\partial T} + \vec{\mathcal{J}}_{\mathrm{f}} \tag{2.2}$$

$$\nabla \cdot \vec{\mathcal{D}} = \rho_{\mathrm{f}} \tag{2.3}$$

$$\nabla \cdot \vec{\mathcal{B}} = 0 \tag{2.4}$$

where $\vec{\mathcal{E}}$ and $\vec{\mathcal{H}}$ are the electric and magnetic field vectors, respectively, $\vec{\mathcal{D}}$ and $\vec{\mathcal{H}}$ are the corresponding electric and magnetic flux densities, and the time T is taken to be in upper-case in anticipation of future normalization. In a dielectric, the current density $\vec{\mathcal{J}}_{\mathrm{f}}$ and free charge density ρ_{f}, which serve as external sources that drive the field, are zero. Coupling of the applied fields to the medium is included through the constitutive equations

$$\vec{\mathcal{D}} = \epsilon_0 \vec{\mathcal{E}} + \vec{\mathcal{P}} \tag{2.5}$$

$$\vec{\mathcal{B}} = \mu_0 \vec{\mathcal{H}} + \vec{\mathcal{M}} \tag{2.6}$$

where ϵ_0 is the vacuum permittivity, μ_0 is the vacuum permeability, and $\vec{\mathcal{P}}$ and $\vec{\mathcal{M}}$ are the induced electric and magnetic polarizations. The electromagnetic quantities ϵ_0 and μ_0 are related to the speed of light via $1/c^2 = \epsilon_0 \mu_0$. For the non-magnetic media considered in this thesis, $\vec{\mathcal{M}} \equiv 0$.

Taking the curl of Eq. (2.1), the time derivative of Eq. (2.2), and making use of the constitutive equations and a well known vector identity, one obtains the relation

$$\nabla(\nabla \cdot \vec{\mathcal{E}}) - \nabla^2 \vec{\mathcal{E}} = -\mu_0 \frac{\partial^2 \vec{\mathcal{D}}}{\partial T^2} \tag{2.7}$$

In the effective index approximation, $\nabla(\nabla \cdot \vec{\mathcal{P}}) \simeq 0$ and the first term in Eq. (2.7) disappears by virtue of Eq. (2.3) and Eq. (2.5). Assuming that the input field is plane-polarized and that the dielectric medium is isotropic and polarization preserving

reduces the vector equation (2.7) to

$$\nabla^2 \mathcal{E} = \mu_0 \frac{\partial^2 \mathcal{D}}{\partial T^2} \tag{2.8}$$

Rather than consider the polarization explicitly, we will write the constitutive equation for $\mathcal{D}$, Eq. (2.5), as

$$\mathcal{D} = \epsilon_0 \epsilon \, \mathcal{E} \tag{2.9}$$

where $\epsilon = \epsilon(\omega, |\mathcal{E}|^2)$ is the relative permittivity that is both frequency and field dependent such that Eq. (2.8) becomes

$$\nabla^2 \mathcal{E} = \frac{1}{c^2} \frac{\partial^2 (\epsilon \mathcal{E})}{\partial T^2} \tag{2.10}$$

Assuming that the relative permittivity can be separated into linear and nonlinear parts

$$\begin{aligned} \epsilon &= \epsilon_{\mathrm{L}}(\omega) + \epsilon_{\mathrm{NL}}(\mathcal{E}) \\ &= \epsilon_{\mathrm{L}} + (\omega - \omega_0) \left. \frac{\partial \epsilon_{\mathrm{L}}}{\partial \omega} \right|_{\omega_0} + (\omega - \omega_0)^2 \left. \frac{\partial^2 \epsilon_{\mathrm{L}}}{\partial \omega^2} \right|_{\omega_0} + \chi^{(3)} \, F(|\mathcal{E}|^2) \end{aligned} \tag{2.11}$$

where $\epsilon_{\mathrm{L}}(\omega)$ has been Taylor expanded to second order under the assumption that the bandwidth of the pulse is limited to a small range of frequencies centred about the frequency ω_0. The first term ϵ_{L} is the familiar linear dielectric constant of the medium. The second term determines the group velocity v_{g}, the speed at which the optical envelope travels. The subsequent expression is the group velocity dispersion (GVD) and, as discussed in Section 2.2, is responsible for temporal spreading of the wavepacket. (For the case of extremely short pulses or when operating near the zero-dispersion wavelength, one must consider the effects of higher order dispersion.) The nonlinear term is free of dispersion as it contains no ω dependence. This is equivalent to stating that the nonlinear response of the medium is instantaneous, a reasonable assumption for picosecond pulses when the electronic response is on the femtosecond timescale. We allow for arbitrary nonlinearities by virtue of the function F. There

is no term proportional to $|E|$ due to the existence of an inversion symmetry at the molecular level of most dielectrics. Note that $\chi^{(3)}$, generally a fourth-rank tensor, has been written as a scalar quantity for the case of an isotropic polarization preserving medium.

The familiar optical refractive index is defined by the equation $n \equiv \sqrt{\epsilon}$. With the reasonable assumption that $\epsilon_{\mathrm{NL}} \ll \epsilon_{\mathrm{L}}$, to first order

$$n = n_0 + \frac{1}{2n_0}(\omega - \omega_0)\left.\frac{\partial \epsilon_{\mathrm{L}}}{\partial \omega}\right|_{\omega_0} + \frac{1}{4n_0}(\omega - \omega_0)^2\left.\frac{\partial^2 \epsilon_{\mathrm{L}}}{\partial \omega^2}\right|_{\omega_0} + n_2\, F(|\mathcal{E}|^2) \tag{2.12}$$

where $n_0 = \sqrt{\epsilon_{\mathrm{L}}}$ and the nonlinear coefficient $n_2 = \chi^{(3)}/(2n_0)$.

It is useful to isolate the relatively slow modulations of $\mathcal{E}$ from the underlying fast oscillations at frequency ω_0 by separating the field into an envelope and plane-wave carrier in the propagation direction Z

$$\mathcal{E} = \Phi(X, Y, Z, T)\, \mathrm{e}^{i(k_0 Z - \omega_0 T)} \tag{2.13}$$

with the central wavevector $k_0 = n_0\omega_0/c$.

With ϵ being frequency dependent, we make use of the Fourier identity $\partial/\partial T \rightarrow -i(\omega - \omega_0)$ in order to write the wave equation (2.10) in the time domain

$$\left(\frac{\partial^2\Phi}{\partial X^2} + \frac{\partial^2\Phi}{\partial Y^2} + \frac{\partial^2\Phi}{\partial Z^2} + 2ik_0\frac{\partial\Phi}{\partial Z} - {k_0}^2\Phi\right)\mathrm{e}^{i(k_0 Z - \omega_0 T)} - \frac{1}{c^2}\frac{\partial^2}{\partial T^2}\left[\left(\epsilon_{\mathrm{L}} - i\frac{\partial \epsilon_{\mathrm{L}}}{\partial \omega}\frac{\partial}{\partial T} - \frac{1}{2}\frac{\partial^2 \epsilon_{\mathrm{L}}}{\partial \omega^2}\frac{\partial^2}{\partial T^2} + \chi^{(3)}F(|\Phi|^2)\right)\Phi \mathrm{e}^{i(k_0 Z - \omega_0 T)}\right] = 0 \tag{2.14}$$

In order to simplify this equation, it is usual to assume the slowly varying envelope approximation

$$\left|\frac{\partial^2\Phi}{\partial Z^2}\right| \ll 2k_0\left|\frac{\partial\Phi}{\partial Z}\right|$$

wherein the second-derivative term above is neglected, to neglect all time derivatives higher than second order in the cross term and to make the slowly varying nonlinearity

approximation

$$\frac{\partial^2}{\partial T^2}\left[F(|\Phi|^2)\Phi\right] = -{\omega_0}^2 F(|\Phi|^2)\Phi$$

Under these approximations, Eq. (2.14) becomes

$$2ik_0\left(\frac{\partial\Phi}{\partial Z}+\frac{1}{v_g}\frac{\partial\Phi}{\partial T}\right)+\frac{\partial^2\Phi}{\partial X^2}+\frac{\partial^2\Phi}{\partial Y^2}+k_0 D\frac{\partial^2\Phi}{\partial T^2}+\frac{2{k_0}^2 n_2}{n_0}F(|\Phi|^2)\Phi=0 \tag{2.15}$$

where the group velocity

$$\frac{1}{v_g}\equiv\left.\frac{\partial k}{\partial\omega}\right|_{\omega_0}=\left(\frac{n_0}{c}+\frac{\omega_0}{c}\frac{\partial n_0}{\partial\omega}\right)=\frac{1}{n_0 c}\left(\epsilon_L+\frac{\omega_0}{2}\frac{\partial\epsilon_L}{\partial\omega}\right) \tag{2.16}$$

and the group velocity dispersion (GVD) coefficient

$$D\equiv-\left.\frac{\partial^2 k}{\partial\omega^2}\right|_{\omega_0}=\frac{1}{{v_g}^2}\frac{\partial v_g}{\partial\omega}=\frac{1}{\omega_0 n_0 c}\left(\epsilon_L+2\omega_0\frac{\partial\epsilon_L}{\partial\omega}+\frac{{\omega_0}^2}{2}\frac{\partial^2\epsilon_L}{\partial\omega^2}\right) \tag{2.17}$$

When $D<0$, the material is said to exhibit normal dispersion whereas for $D>0$, the case considered in this thesis, the material is said to display anomalous dispersion.

Using the scalings [Si90]

$$\begin{aligned}
t &\equiv \frac{1}{\sigma}\left(T-\frac{1}{v_g}Z\right)\left(\frac{k_0}{D}\right)^{\frac{1}{2}}\\
(x,y) &\equiv \frac{1}{\sigma}k_0\,(X,Y)\\
z &\equiv \frac{1}{\sigma^2}k_0\,Z\\
E &\equiv \sigma\left(\frac{n_2}{n_0}\right)^{\frac{1}{2}}\Phi\\
f(|E|^2) &\equiv \sigma^2\frac{n_2}{n_0}F(|\Phi|^2)
\end{aligned} \tag{2.18}$$

where σ is a dimensionless scale factor that sets the pulse duration, Eq. (2.15) can be transformed into its final dimensionless form

$$i\frac{\partial E}{\partial z}+\frac{1}{2}\left(\frac{\partial^2 E}{\partial t^2}+\frac{\partial^2 E}{\partial x^2}+\frac{\partial^2 E}{\partial y^2}\right)+f(|E|^2)E=0 \tag{2.19}$$

Equation (2.19) is commonly referred to as the generalized nonlinear Schrödinger equation (GNLSE) and governs the propagation of plane-polarized optical envelopes in an anomalously-dispersive bulk medium.

Before proceeding, let us make contact with reality and discuss the transformation from Eq. (2.15) to the dimensionless GNLSE. The definition of t is a shift into a reference frame moving with the pulse at the group velocity (normalized by k_0 and the GVD coefficient). In addition, the laboratory spatial coordinates (X, Y, Z) have been scaled by the mean wave number to define a dimensionless position vector (x, y, z). Immediately, we are struck by the complete symmetry between the scaled transverse coordinates and the retarded time which explicitly demonstrates the equivalence between spatial self-focusing and temporal compression. In addition, the (scaled) GNLSE contains no explicit dependence on the strength of the nonlinearity. Thus, remarkably, solutions to Eq. (2.19) are unaffected by a change in n_2, the sole influence being a rescaling of the electric field and a resultant change in the pulse's energy content. As values of n_2 can span several orders of magnitude, so can the self-trapped energy.[1] A brief glance through this thesis reveals that in dimensionless units, the solitary waves that we consider are spherically symmetric. What do such pulses look like in the laboratory frame? Admittedly, the answer to this question will depend on the specific medium, but as an illustrative example, let us consider silica[2] at the anomalously dispersive wavelength of 1.5 μm for which $D \simeq 1.8 \times 10^{-26}$ s^2/m and the group velocity $v_g \simeq 2 \times 10^8$ m/s. From the scalings above, the conversions from simulation values to real distances, times and field strengths are given by

$$(\Delta X, \Delta Y) = \frac{\sigma}{k_0}(\Delta x, \Delta y)$$

[1] For example, Silberberg [Si90] and McLeod *et al.* [Mc95] calculate pulse energies of 80 μJ and 25 pJ, respectively, by varying the material parameters and pulse duration while still remaining faithful to the assumptions used in deriving the GNLSE.

[2] Note, silica possesses a Kerr-like nonlinear refractive index, $f(|E|^2) = |E|^2$, which is characteristic of many existing materials. Unfortunately, as demonstrated by Silberberg [Si90] (and explained at length in Chapter 3), Kerr-like media cannot support stable three-dimensional pulses! Still, as we will be considering deviations from Kerr behaviour, silica serves as a reasonable and familiar baseline.

$$\begin{aligned} \Delta T &= \sigma \left(\frac{D}{k_0}\right)^{\frac{1}{2}} \Delta t \\ \Delta Z &= \sigma^2 \frac{1}{k_0} \Delta z \\ \Phi &= \frac{1}{\sigma} \left(\frac{n_0}{n_2}\right)^{\frac{1}{2}} E \end{aligned} \tag{2.20}$$

where the scale factor σ is determined from the definition of the retarded time and is found to be

$$\sigma = \left(\frac{k_0}{D}\right)^{\frac{1}{2}} \frac{\Delta T}{\Delta t} \tag{2.21}$$

For the parameters of silica, a 1 ps pulse spanning $\Delta t = 1$ in simulation units yields a scale factor $\sigma = 2.3 \times 10^4$. Thus, $|E| = 1$ corresponds to a real field strength of $|\Phi| = 4.8$ MV/m which is easily obtainable with existing laser systems. What length of bulk material is required for these specific parameter values and pulse duration? For the parameters of silica, one finds that every $z = 1$ travelled in simulation units corresponds to a real distance of $Z = 53$ m. Admittedly this is a prohibitively large value for a bulk dielectric, however, as Z scales like σ^2, this length can be reduced to centimeter distances by considering shorter pulse envelopes modulating a lower frequency carrier in the presence of larger GVD. (Of course, in doing so, one must be careful to remain reasonably faithful to the assumptions used in deriving the propagation equation.)

In rescaled units our profiles are spherically symmetric so that $\Delta x = \Delta y = \Delta t$, which, in combination with the above conversion relations yields

$$(\Delta X, \Delta Y) = (k_0 D)^{-\frac{1}{2}} \Delta T \tag{2.22}$$

for the transverse size. With the pulse length in the propagation direction given by $\Delta Z = v_g \Delta T = 0.2$ mm, in the transverse direction $(\Delta X, \Delta Y) = 3.6$ mm. Therefore, while the solitary waves are taken to be spherical in our dimensionless units, in the laboratory frame they exist as highly squashed ellipsoidal pulses (at least for this particular choice of D, k_0 and v_g).

As shall be demonstrated in the chapters that follow, for a general class of index

of refraction models, the GNLSE supports the propagation of highly stable spherical self-trapped spatio-temporal solitons more commonly referred to as "light bullets." Defining the normalized distance $r = \sqrt{t^2 + x^2 + y^2}$, spherically symmetric solitary wave profiles are found by substituting the assumed form

$$E(r, z) = U(r) \exp(i\beta z) \tag{2.23}$$

into Eq. (2.19), yielding a second-order ordinary nonlinear differential equation for the radial profiles, viz.

$$\frac{\mathrm{d}^2 U}{\mathrm{d}r^2} + \frac{2}{r}\frac{\mathrm{d}U}{\mathrm{d}r} + 2U\left[f(U^2) - \beta\right] = 0 \tag{2.24}$$

The adjustable propagation constant β dictates a shift away from the central wavevector; mathematically, β is the eigenvalue that governs the general shape of the resultant solitary wave. Generally speaking, Eq. (2.24) is analytically intractable and must be solved numerically.

2.2 A balance of forces: dispersion, diffraction, and self-phase modulation

In order to study the dynamics of a given envelope, it is necessary to integrate Eq. (2.19) forward in z. Unfortunately, this cannot be done analytically and therefore we must evolve the initial condition numerically as described in Section 2.3. However, while the full GNLSE is analytically intractable, it is instructive to separately examine the effects of the linear and nonlinear terms.

Consider first the GNLSE without the nonlinearity,

$$i\frac{\partial E}{\partial z} + \frac{1}{2}\left(\frac{\partial^2 E}{\partial t^2} + \frac{\partial^2 E}{\partial x^2} + \frac{\partial^2 E}{\partial y^2}\right) = 0 \tag{2.25}$$

If we introduce the Fourier transform[3] of E

$$\tilde{E}(f_t, f_x, f_y, z) = \int\int\int E(t, x, y, z)\, e^{2\pi i f_t t}\, e^{2\pi i f_x x}\, e^{2\pi i f_y y}\, dt\, dx\, dy \tag{2.26}$$

then in frequency space the linear operator

$$\nabla^2 \equiv \frac{\partial}{\partial t^2} + \frac{\partial}{\partial x^2} + \frac{\partial}{\partial y^2} \rightarrow (2\pi i)^2 \left[f_t^{\,2} + f_x^{\,2} + f_y^{\,2} \right] \tag{2.27}$$

becomes simply a scalar phase factor. This being the case, Eq. (2.25) can be written as

$$i\frac{\partial \tilde{E}}{\partial z} + \frac{1}{2}(2\pi i)^2 f_T \tilde{E} = 0 \tag{2.28}$$

where we have defined $f_T{}^2 \equiv f_t{}^2 + f_x{}^2 + f_y{}^2$. This equation is easily solved to give

$$\tilde{E}(z) = e^{i\frac{1}{2}(2\pi i)^2 f_T{}^2 z}\, \tilde{E}(0) \tag{2.29}$$

While the power spectrum of the pulse $|\tilde{E}|^2$ is unchanged by dispersion - the effect being a frequency dependent modification of the phase of the spectral components - this has definite consequences for the real space profile $E(z)$ which can be extracted by means of the inverse Fourier transform

$$E(t, x, y, z) = \int\int\int \tilde{E}(f_t, f_x, f_y, z)\, e^{-2\pi i f_t t}\, e^{-2\pi i f_x x}\, e^{-2\pi i f_y y}\, df_t\, df_x\, df_y \tag{2.30}$$

As a simple yet illustrative example, if the initial pulse shape (in our dimensionless coordinates and moving reference frame) is a spherical Gaussian

$$E(r, z{=}0) = e^{-r^2} \tag{2.31}$$

the profile at any later distance z is found to be

$$E\,(r, z) = \frac{1}{\sqrt{1 + 2iz}}\, e^{-\frac{r^2}{1+2iz}} \tag{2.32}$$

[3]Theoreticians might puzzle over the choice of this cumbersome definition - it is the *de facto* implementation for numerical Fourier Transform packages.

The pulse's behaviour can be made more transparent by writing E as a real amplitude multiplied by a complex phase,

$$E(r,z) = \frac{1}{\sqrt{1+4z^2}} \, \mathrm{e}^{-\frac{r^2}{1+4z^2}} \, \mathrm{e}^{-\frac{ir^2}{2z+1/2z} - i\tan^{-1} 2z} \tag{2.33}$$

which demonstrates that as the pulse propagates, its peak intensity drops monotonically while, due to the decreasing decay constant $1/(1+4z^2)$, the pulse width concomitantly broadens by the same factor. Dispersion is understood on the physical grounds that since the velocity of a given frequency component is itself frequency dependent, the various components that comprise the pulse will travel at different speeds, resulting in a general spreading of the initial envelope. In particular, in the anomalous dispersion regime, red-shifted components (with respect to the central wavelength λ_0) travel more slowly than their blue-shifted counterparts. Diffraction appears in Eq. (2.25) in a mathematically equivalent way and therefore also leads to a general spreading of the pulse in the transverse coordinates.

Let us next consider the effect of the nonlinearity alone such that the GNLSE becomes

$$i\frac{\partial E}{\partial z} + f(|E|^2)E = 0 \tag{2.34}$$

which is readily solved, yielding

$$E(r,z) = \mathrm{e}^{if(|E(r,0)|^2)z} \, E(r,0) \tag{2.35}$$

Equation (2.35) reveals that the nonlinearity alone does not affect the envelope shape $|E|$ although it does produce an intensity-dependent phase shift known as *self-phase modulation* (SPM) [Ag89, Sh89]. Such a temporally varying phase implies that the instantaneous frequency differs across the pulse from its central value of ω_0, the shift being given by

$$\Delta\omega = -\frac{\partial f(|E|^2)}{\partial t} z \tag{2.36}$$

where the minus sign is due to our (conventional) choice of $\exp(-i\omega_0 t)$ for the time portion of the rapidly varying plane carrier wave. For the $f(|E|^2)$ considered in

Chapter 3, $\Delta\omega < 0$ (red-shift) on the leading edge of the pulse and $\Delta\omega > 0$ (blue-shift) on the trailing edge. While nonlinearity alone does not modify the pulse shape, SPM effectively leads to pulse compression as it continually wavelength-shifts the leading and trailing pulse edges which are then decelerated and accelerated respectively as a result of anomalous dispersion. Compression in the transverse direction is more easily understood based on the arguments presented in the introduction. With $\mathrm{d}f/\mathrm{d}|E|^2 > 0$, the refractive index increases towards the pulse centre. This gradient induces a curvature of the phase front as the beam edge travels faster than the beam interior. In the language of geometrical optics, such a refractive index gradient leads to focusing of the light rays perpendicular to the phase front.

Based on the above arguments, we see that dispersion/diffraction and SPM/self-focusing play the role of opposing "forces" acting on the pulse envelope. With a proper balance, it is at least conceivable that the result could be the propagation of a stable three-dimensional optical envelope soliton - a light bullet.

2.3 Numerical method

We turn now to the numerical method used to propagate a configuration of envelopes forward in z according to Eq. (2.19). For the one-dimensional NLSE, it is possible to use explicit finite-difference methods, however, in three dimensions, the short timesteps required to maintain accuracy and numerical stability become computationally prohibitive. Therefore, the method used in this thesis is a simple extension of the split-step Fourier method [Ag89, Fe78] to three dimensions.

One begins by noting that the GNLSE, Eq. (2.19), has a formal solution

$$E(t,x,y,\Delta z) = \mathrm{e}^{i\left[\frac{1}{2}\nabla^2\Delta z + \int_0^{\Delta z} f(|E|^2)\mathrm{d}z\right]} E(t,x,y,0) \tag{2.37}$$

where ∇^2 is the Laplace operator in the t,x,y cartesian coordinate system and the exponential function is defined by its power series expansion.

The exponential can be approximated as

$$e^{i(\hat{a}+\hat{b})} \simeq e^{\frac{i}{2}\hat{a}}\, e^{i\hat{b}}\, e^{\frac{i}{2}\hat{a}} \tag{2.38}$$

where the operator $\hat{a} = \nabla^2 \Delta z$ and $\hat{b} = \int_0^{\Delta z} f(|E|^2) \mathrm{d}z$. This expression is accurate to order $(\Delta z)^3$ as can be seen by Taylor expanding both sides. For small Δz, we can reasonably approximate $\hat{b} = f(|E|^2)\, \Delta z$. This being the case, to the order specified the formal solution of Eq. (2.37) becomes

$$E(t,x,y,\Delta z) \simeq e^{i\nabla^2 \frac{\Delta z}{2}}\, e^{i\, f(|E|^2)\, \Delta z}\, e^{i\nabla^2 \frac{\Delta z}{2}}\, E(t,x,y,0) \tag{2.39}$$

Interpreted physically, in order to evolve the solution a distance Δz, the numerical scheme (i) uses only dispersion and diffraction for a distance $\Delta z/2$ (ii) applies a nonlinear correction using the midpoint value of the field E applied over the full range Δz (iii) continues for the final half-step using only dispersion and diffraction. Numerically, the advantage of the split step Fourier method is the tremendous speed increase[4] one obtains by taking large "time"-steps and using the Fast Fourier Transform (FFT) [Co65] to solve the linear dispersive/diffractive problem.

Denoting $\mathcal{F}$ and $\mathcal{F}^{-1}$ as the forward and reverse Fourier transforms respectively, Eq. (2.39) can be written as

$$E(t,x,y,\Delta z) = \mathcal{F}^{-1} e^{-2\pi^2 i f_T{}^2 \Delta z} \mathcal{F}\, e^{i\, f(|E|^2)\, \Delta z}\, \mathcal{F}^{-1} e^{-2\pi^2 i f_T{}^2 \Delta z} \mathcal{F}\; E(t,x,y,0) \tag{2.40}$$

To evolve the solution forward to $2\Delta z$, one simply concatenates the string of Fourier and exponential operators

$$\begin{aligned} E(t,x,y,2\Delta z) \;=\; & \mathcal{F}^{-1} e^{-2\pi^2 i f_T{}^2 \Delta z} \mathcal{F}\, e^{i\, f(|E|^2)\, \Delta z}\, \mathcal{F}^{-1} e^{-2\pi^2 i f_T{}^2 \Delta z} \mathcal{F}\mathcal{F}^{-1} e^{-2\pi^2 i f_T{}^2 \Delta z} \\ & \mathcal{F} e^{i\, f(|E|^2)\, \Delta z}\, \mathcal{F}^{-1} e^{-2\pi^2 i f_T{}^2 \Delta z} \mathcal{F}\, E(t,x,y,0) \end{aligned} \tag{2.41}$$

[4]See Ref. [Ta84] for a quantitative evaluation of various finite-difference and spectral methods applied to the one-dimensional NLSE. To achieve the same degree of accuracy, one often realizes time savings of two orders of magnitude over conventional finite difference methods.

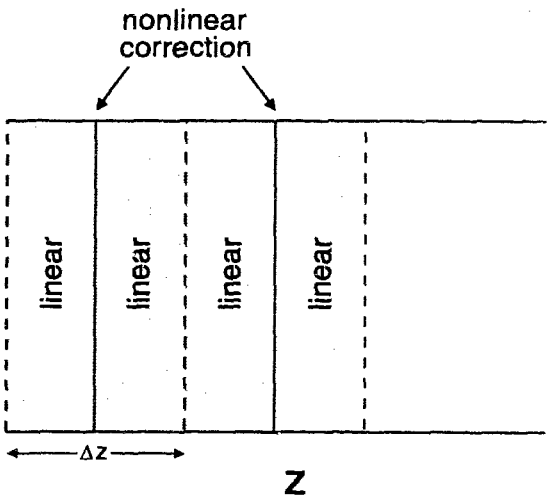

Figure 2.1: Propagation using the split-step Fourier method.

The occurrence of

$$\mathcal{F}^{-1}\, \mathrm{e}^{-2\pi^2 i f_T{}^2 \Delta z}\, \mathcal{F}\mathcal{F}^{-1}\, \mathrm{e}^{-2\pi^2 i f_T{}^2 \Delta z}\, \mathcal{F} \tag{2.42}$$

simplifies to

$$\mathcal{F}^{-1}\, \mathrm{e}^{-4\pi^2 i f_T{}^2 \Delta z}\, \mathcal{F} \tag{2.43}$$

Thus, one begins and ends the calculation with a half step of dispersion and diffraction, the intermediate stages being full Δz steps of alternating nonlinear corrections and dispersive/diffractive advance as schematically depicted in Figure 2.1.

All of the simulations in this thesis were performed on three-dimensional rectangular meshes, either 140^3, $140 \cdot 70^2$, 128^3 or $256 \cdot 128^2$, depending on the nature of the problem and the machine used. LBC, the propagation code, was implemented in standard Fortran 77 using existing FFT libraries. The Scientific Subroutine Library (SSLII) FFT package was utilized for the simulations performed on the 2.5 Gigaflop (peak speed) Fujitsu VPX 240/10 vectorizing supercomputer at the High Performance Computing Centre (HPCC) in Calgary, Alberta.[5] For earlier simulations performed on an IBM RISC/6000 workstation, we used a highly optimized radix-two scalar FFT package written by Leonard Gomelsky of NASA Ames Research Center.

[5]The majority of the simulations in this thesis were carried out under the auspices of the HPCC graduate research scholarship program. HPCC maintains a World Wide Web presence at <URL:http://www.hpc.com/>.

In addition to the core routines that handle the alternating stages of dispersion/diffraction and nonlinear advance, there exist subroutines for monitoring the accuracy of the evolving solution. The accuracy subroutines calculate the conserved quantities of Eq. (2.19), viz.

$$J_1 \equiv \int |E|^2 \mathrm{d}^3 r \tag{2.44}$$

$$J_2 \equiv i \int \left(E \frac{\partial E^*}{\partial t} - E^* \frac{\partial E}{\partial t} \right) \mathrm{d}t \tag{2.45}$$

$$J_3 \equiv \int \left(\left| \frac{\partial E}{\partial t} \right|^2 - \int_0^I f(s)\, \mathrm{d}s \right) \mathrm{d}t \tag{2.46}$$

corresponding to conservation of the total power, total momentum, and total energy of the field. The J_i can either be kept within a predefined tolerance by step-size control or reviewed after the simulation.

Periodic boundary conditions are implicit in the Fourier transform method of solving the dispersive/diffractive advance. As a consequence, outgoing radiation that would otherwise physically escape to infinity, instead re-enters the system from the opposing face of the computational mesh. In one-dimensional problems, infinite boundaries (often called radiation boundary conditions) are achieved by the application of a suitably crafted damping function over a range of gridpoints near the mesh edge [Is81]. This is problematic in three dimensions where, on a coarse grid, one typically cannot afford to sacrifice a sizeable volume of surrounding grid points; the naive approach of setting only the boundary to zero simply results in reflection of the outgoing wave.[6] After much experimentation we chose to simply accept periodic boundaries as a necessary unpleasantness.

Let us now turn our attention to building refractive index models that will support stable light bullets - models whose stability properties and soliton dynamics will be examined using the numerical code described above.

[6] An additional consequence of applying a sponge filter is that the integrated energy $J_1 \equiv \int |E|^2 \mathrm{d}^3 r$ is no longer numerically conserved.

Chapter 3

Towards stable light bullets: model building

This chapter begins with a discussion of unstable Kerr model light bullets, next discusses construction of the simplest physically realizable model that supports stable bullets, and concludes with a discourse on the creation of bistable light bullets. As mentioned in the introduction, bistable solitons as defined by Kaplan [Ka85a, Ka85b] have the same energy content but radically different radial profiles and are thus natural carriers of binary information.

3.1 The unstable Kerr model

It has long been known that plane-polarized optical solitary wave structures in greater than one-dimension are unstable. In 1990, Silberberg predicted [Si90] that a suitably intense spherical three-dimensional pulse propagating in a bulk anomalously dispersive Kerr medium could undergo symmetric radial collapse. While this thesis is concerned with the propagation of *stable* light bullets, it is worthwhile first considering Kerr model light bullets for two reasons: (i) to verify the predicted instability, and (ii) as a pedagogical device for demonstrating how one can construct a refractive index model that will support stable light bullets.

For the case of the Kerr model, $f(I) = I$, the generalized nonlinear Schrödinger

equation, Eq. (2.19), becomes

$$i\frac{\partial E}{\partial z} + \frac{1}{2}\left(\frac{\partial^2 E}{\partial t^2} + \frac{\partial^2 E}{\partial x^2} + \frac{\partial^2 E}{\partial y^2}\right) + |E|^2 E = 0 \tag{3.1}$$

As mentioned in the last chapter, in order to find spherical solitary wave solutions to Eq. (3.1), one substitutes the assumed form

$$E(r,z) = U(r)\ \exp(i\beta z) \tag{3.2}$$

into the GNLSE yielding the nonlinear ordinary differential equation

$$\frac{\mathrm{d}U}{\mathrm{d}r^2} + \frac{2}{r}\frac{\mathrm{d}U}{\mathrm{d}r} - 2\beta U + 2U^3 = 0 \tag{3.3}$$

Under the assumption that the real amplitude U has its maximum value at $r = 0$, while $\mathrm{d}U/\mathrm{d}r,\ \mathrm{d}^2U/\mathrm{d}r^2 \to 0$ as $r \to \infty$, Eq. (3.3) constitutes a two-point boundary value problem. While the Kerr case admits the familiar sech soliton in one-dimension, here it admits no known closed form solution and must be solved either numerically or approximated using traditional techniques [Ha92].[1] We use a standard shooting method [Pr86] whereby, fixing the propagation parameter β, we search via bisection for the $U(0)$ value that when used as an initial condition to Eq. (3.3), yields a profile satisfying the above boundary conditions.

For example, Figure 3.1 shows three sample radial field profiles from among the infinite spectrum of allowed states. (The steep slope apparent at the origin for the top two profiles is an artifact of the horizontal plot scale; a closer view reveals that $\mathrm{d}U/\mathrm{d}r \to 0$ as $r \to 0$.) As shown in the inset, while the peak intensity rises with increasing β, the pulse width narrows as the profiles become more tightly bound. An

[1] A new and conceptually novel approach to finding stationary solutions has been introduced into the literature by Alan Snyder and co-workers [Sn91, Sn93, Sn95]. The problem of determining the mode structure of a guided wave in a linear medium having a known transverse refractive index $n(x)$ is a familiar and often tractable (linear) problem. Their insight was to recognize that since every soliton is a mode of the linear waveguide that it induces, its profile can be determined via an elementary self-consistency condition: the soliton induces $n(x)$ which can then be thought of as a linear mode-structure problem whose solution has to be the original profile!

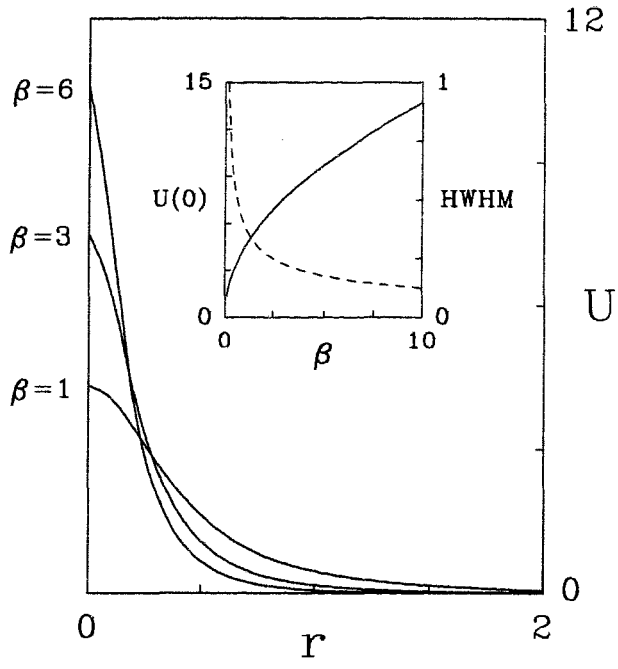

Figure 3.1: Sample Kerr model radial field profiles. Inset: Peak height (solid curve) and half-width at half-maximum (dashed line) versus β.

obvious question then arises: what does the total pulse energy (normalized power)

$$P(\beta) = \int_0^\infty U(\beta)^2 \, r^2 \, \mathrm{d}r \tag{3.4}$$

look like as a function of β? Calculating P for a range of β values, the result is plotted in Figure 3.2, where it is found that despite their higher peak intensity, larger β value light bullets have relatively lower energy content than their lower β siblings. This can be seen analytically by realizing that Eq. (3.3) possesses a remarkable set of scaling relationships. A three-dimensional radially symmetric solitary wave can be scaled by a factor τ via the relations

$$\begin{aligned} \tilde{U}(r) &= \tau \, U(\tau r) \\ \tilde{\beta} &= \tau^2 \, \beta \\ \tilde{P} &= \tau^{-1} \, P \end{aligned} \tag{3.5}$$

Thus, for example, beginning with the $\beta = 1$ profile, the $\beta = 6$ profile can be generated from this solution by virtue of the above relations with $\tau = \sqrt{6} \simeq 2.45$. This new profile will then have a peak height 2.45 times the original pulse but a power reduced

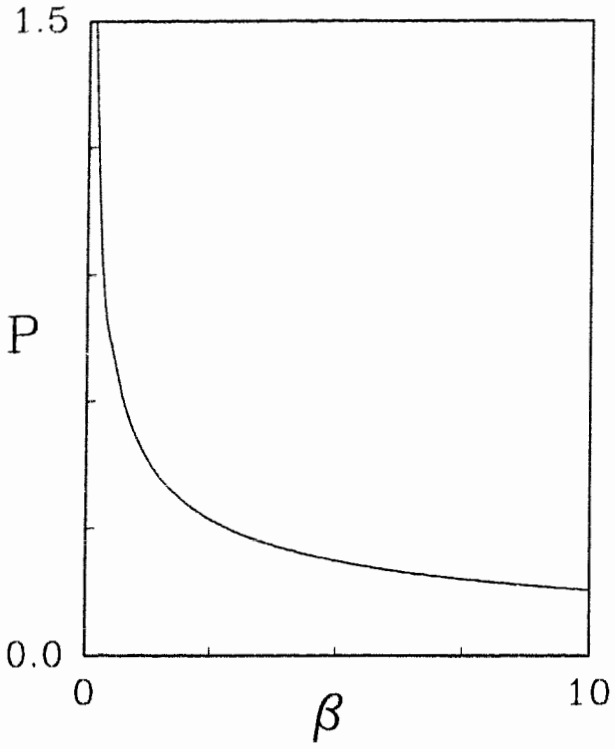

Figure 3.2: Integrated pulse intensity versus propagation parameter for Kerr model light bullets.

by the same factor. These scaling relations are ideal for producing small, intense (but relatively low energy) pulses.

The scaling relations also allow one to understand the qualitative shape of the P-β energy curve. If (β_0, P_0) is a point on this curve, the τ value for any other point β is given by $\tau = \sqrt{\beta/\beta_0}$ which leads to the power function

$$P(\beta) = \left(\frac{\beta}{\beta_0}\right)^{-\frac{1}{2}} P_0 \tag{3.6}$$

the slope of this curve being given by

$$\frac{\mathrm{d}P}{\mathrm{d}\beta} = -\frac{1}{2}\left(\frac{\beta}{\beta_0}\right)^{-\frac{3}{2}} \frac{P_0}{\beta_0} \tag{3.7}$$

which is negative for *all* β values. Kolokolov has shown via a linear stability analysis [Ko73] that when $\mathrm{d}P/\mathrm{d}\beta < 0$, the solitary waves are intrinsically radially unstable to propagation. Conversely, solitary waves for which $\mathrm{d}P/\mathrm{d}\beta > 0$ are found to be

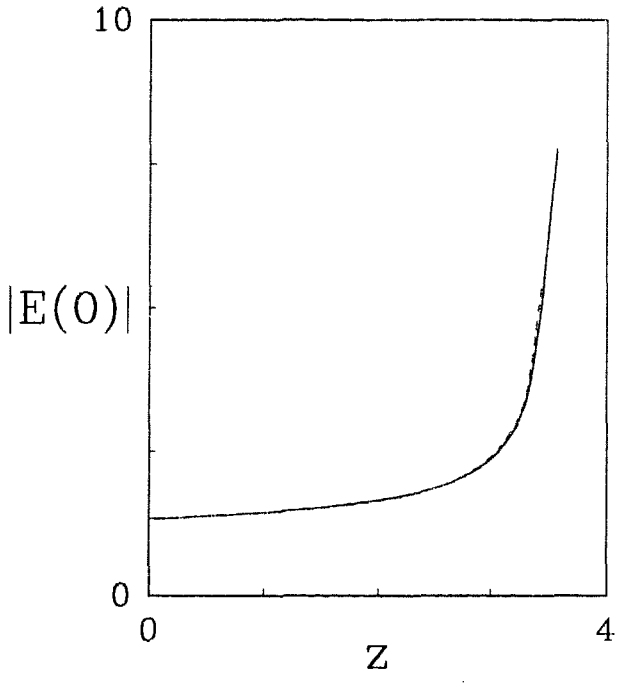

Figure 3.3: Peak field versus propagation distance z for $\beta = 0.1$ simulation. Solid line: $-6 \leq (t, x, y) \leq 6$ domain. Dashed line: $-8 \leq (t, x, y) \leq 8$ domain.

radially stable to small perturbations, although they may or may not be stable to large perturbations in the form of collisions [En87a, En87b]. Thus, with reference to the Kerr model energy curve in Figure 3.2, one expects that, in contrast to the well-known one-dimensional NLSE soliton solutions, all spherical three-dimensional solitary waves will be unstable. Indeed, numerically we find this to be the case.

As an illustrative example, Figure 3.3 plots the peak field $|E(0,0,0)|$ versus z for the $\beta = 0.1$ solitary wave positioned at the centre of a 140^3 mesh. The GNLSE conserves the integrated envelope intensity so the rise in the pulse's peak field is accompanied by a general narrowing of the pulse width. As the evolution code does not have an adaptable mesh, the simulation results become inaccurate when the size of the collapsing bullet shrinks to the scale of the intramesh spacing. This is a separate issue from the physical validity of the equation itself. At some point during the collapse process the assumptions used in deriving the GNLSE become untenable and higher-order corrections should be taken into account. (Recently, Akhmediev *et al.* [Ak93b] have demonstrated that in the case of critical self-focusing, one cannot even assume that the propagation parameter β is constant and independent of z.)

The pulse collapse of Figure 3.3 was observed for various computational domain

sizes (for clarity, only two are shown), the larger domain simulation necessarily terminating earlier due to the coarser mesh. Until this point, however, both curves show excellent agreement which instills a certain amount of faith in the numerical validity of the result.

With the instability of Kerr model light bullets suitably demonstrated, we proceed to developing non-Kerr models that *will* support stable three-dimensional optical solitons.

3.2 Stable light bullets via saturation

As mentioned in the previous section, a necessary condition for radial stability is that the P-β energy curve possess a region of positive slope [Ko73, Wi75]. While this was not possible for the Kerr model, this section will show how to design generic models that do possess positive slope branches.

Consider a model of the form

$$f\left(I=|E|^2\right) = I^n \tag{3.8}$$

such that the ordinary differential equation which governs spherical solitary wave profiles becomes

$$\frac{\mathrm{d}^2U}{\mathrm{d}r^2} + \frac{2}{r}\frac{\mathrm{d}U}{\mathrm{d}r} - 2\beta U + 2U^{2n+1} = 0 \tag{3.9}$$

The modified scaling relationships for Eq. (3.9) are

$$\begin{aligned} \tilde{U}(r) &= \tau^{\frac{1}{n}}\, U(\tau r) \\ \tilde{\beta} &= \tau^2\, \beta \\ \tilde{P} &= \tau^{\frac{2}{n}-3}\, P \end{aligned} \tag{3.10}$$

Then, if (β_0, P_0) is a point somewhere on the P-β curve,

$$P(\beta) = \left(\frac{\beta}{\beta_0}\right)^{\frac{1}{n}-\frac{3}{2}} P_0 \tag{3.11}$$

the slope of which is given by

$$\frac{\mathrm{d}P}{\mathrm{d}\beta} = \left(\frac{1}{n} - \frac{3}{2}\right)\left(\frac{\beta}{\beta_0}\right)^{\frac{1}{n}-\frac{5}{2}} \frac{P_0}{\beta_0} \tag{3.12}$$

with

$$\mathrm{sign}\left(\frac{\mathrm{d}P}{\mathrm{d}\beta}\right) = \begin{cases} -, & n > 2/3 \\ +, & n < 2/3 \end{cases} \tag{3.13}$$

Based on the positive slope stability criterion, one then expects that in three dimensions an I^n model with $n < 2/3$ will yield stable light bullets for all allowable β values, although a model with explicit sub-linear behaviour is not very physically realistic. However, if we are content with a subset of propagation constants, one can postulate a model that is Kerr-like at low intensities ($n = 1$ yielding negative slope at low β) but saturates at higher intensities. Bullets with peak intensities in this latter region will experience sub-($n = 2/3$) behaviour giving rise to a positive slope branch on the energy curve. A natural choice is the saturable model

$$f(I) = \frac{I}{1 + aI} \tag{3.14}$$

which is Kerr-like at low I but saturates at the value $1/a$. The inset of Figure 3.4 shows three solitary wave profiles[2] for $\beta = 0.138$, $\beta = 1.03$ and $\beta = 4.0$ with associated normalized energies as shown in the main figure. As expected, solitary waves with low β values (which have correspondingly small peak intensities) "see" a refractive index model that is Kerr-like and are thus located on the negative slope of the resultant energy curve. Conversely, saturation of the nonlinearity at higher intensities leads to a positive slope branch of (presumably) stable light bullets.

Before proceeding to numerically evolve these solutions, it is worth noting that while the quantitative form of the energy curve is a-dependent, the qualitative U-shaped behaviour is characteristic of all models that are Kerr-like for small I but behave like I^n with $n < 2/3$ at higher intensities, for example, Figure 3.5 shows the U-shaped energy curves obtained for varying degrees of saturation.

[2]The inset symbols simply identify a particular $U(r)$ profile.

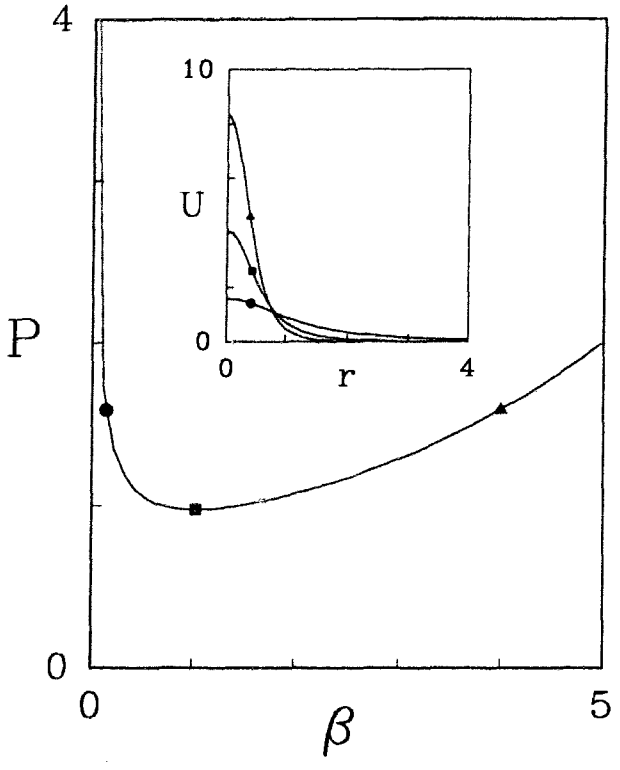

Figure 3.4: Energy curve for saturable model with $a = 0.05$. Inset: Sample radial field profiles for three β values.

An interesting feature of these curves is that they each possess a minimum indicating that there is a minimum energy required for light bullet formation. This fact and the need for the additional scaling relation $\tilde{a} = \tau^{-2}a$ implies that a power scaling relationship for a specific medium does not exist. That is, for a fixed 'a' value and a given β, one cannot scale to another bullet profile containing arbitrarily small energy content.

As predicted, numerical evolution of various saturable model bullets reveals that solitary waves residing on the negative slope of the energy curve are unstable, their field profiles changing with propagation distance z. Typically one observes a gradual decrease in the central intensity accompanied by a general spreading of the pulse. (It is important to note that the U-shaped energy curve should *not* be thought of as a potential well description in which the negative slope bullets "slide" down to the minimum position.) For example, Figure 3.6 shows surface plots of the field values $|E(t, x, y = 0)|$ corresponding to a slice through the centre of the rectangular mesh in the t-x plane for the negative slope light bullet $\beta = 0.138$. (The ring patterns in

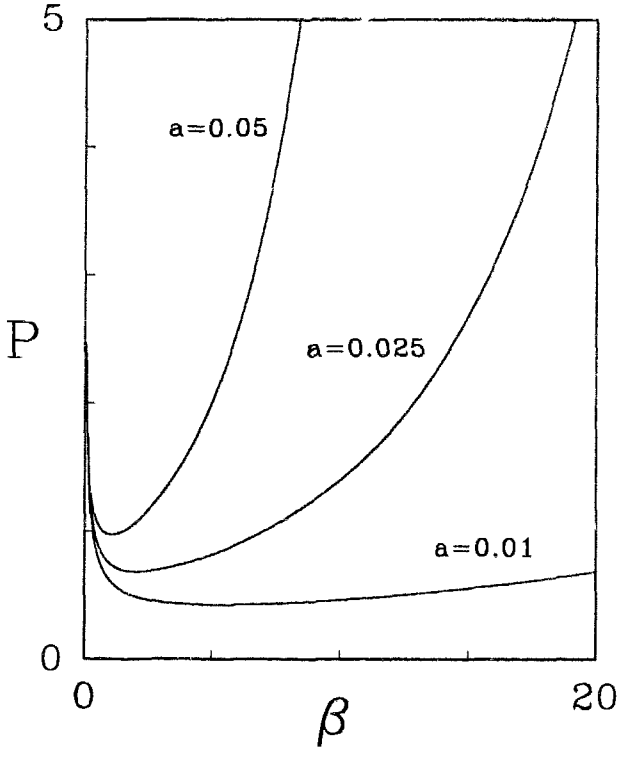

Figure 3.5: Saturable model energy curves for varying degrees of saturation.

frames (a)–(c) are artifacts of the plotting process.) While self-focusing effects are not sufficient to prevent the decay of the negative slope solitary waves, the nonlinearity does serve to at least impede the process. This can be seen in Figure 3.7 where the peak height of the radial profile is plotted versus propagation distance both for the simulation above and in the case of a linear medium in which self-focusing effects are absent leading to a rapid decay of the initial field. (The irregularity in the linear case is due to interference effects as the expanding wavefront crosses the periodic boundary.)

We turn now to the positive slope branch of Figure 3.4 with the hope of finally creating a stable solution. Propagation of the $\beta = 4.0$ light bullet indicated yields the desired result - a self-trapped three-dimensional optical soliton - stable at least to small perturbations in the form of numerical noise.[3] (Pictorially, a single stable bullet is unexciting as the input field simply remains constant in z.) A systematic exploration of the positive slope branch for both the $a = 0.05$ case depicted above

[3]While the noise referred to is the inherent numerical noise due to round-off error and truncation, addition of random noise does not alter the stability.

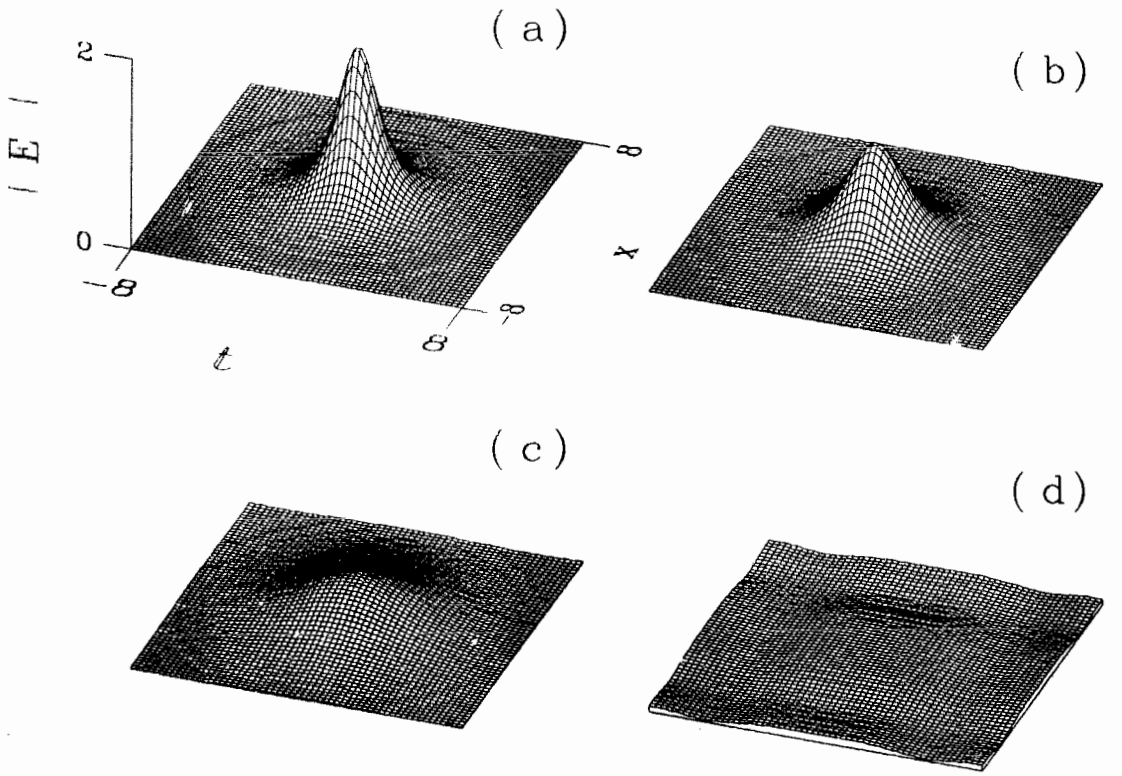

Figure 3.6: Evolution of the negative slope $\beta = 0.138$ light bullet for (a) $z=0$, (b) $z = 14.8$, (c) $z = 20$, and (d) $z = 30$.

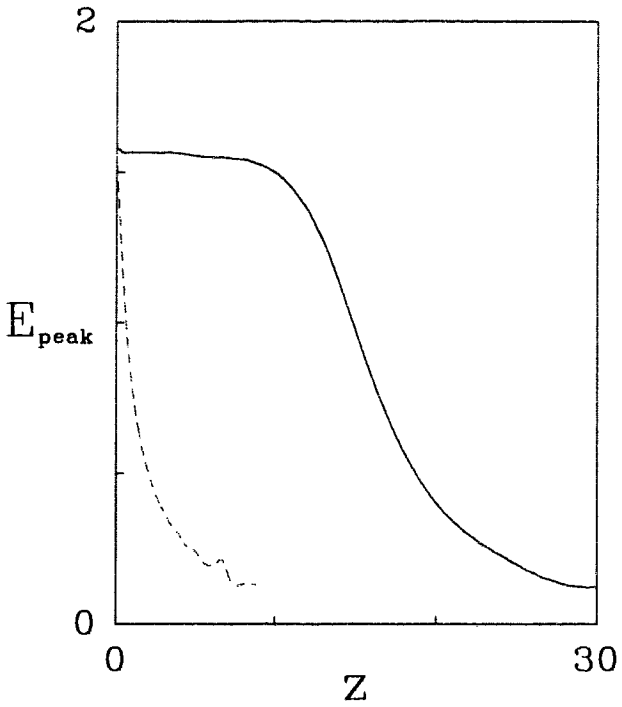

Figure 3.7: Peak height versus z for both the simulation depicted in Figure 3.6 (solid curve) and the corresponding linear medium (dashed curve).

and a selection of other saturation values leads us to conclude that this is a generic result: all pulses living in the $dP/d\beta > 0$ region are inherently stable to propagation, at least for the saturable model in the presence of small amounts of numerical noise.

The bullets propagated so far have all been exact solutions to the ODE that determines the solitary wave radial profile. An obvious and experimentally important question then arises: while positive slope guarantees stability for the propagation of exact initial conditions, what occurs for profiles that are perturbed with respect to these initial states? In the one-dimensional Kerr case, one generally finds that solitons act as attractors for nearby states - arbitrary pulses with energies greater than the soliton threshold self-stabilize, dissipating excess energy as a radiation continuum.[4] While we cannot test the infinite number of allowable (relatively large) perturbations to an exact solitary wave profile, four years of light bullet work by a number of authors [Ak93a, Ed93, Ed96, Mc95] has shown that the light bullet is an extremely robust particle-like entity that spontaneously forms in a saturable medium with sufficient

[4]This attractor-like behaviour seems to be a general feature of nonlinear systems that support solitons. E.g., the seminal Zabusky and Kruskal paper [Za65] on the KdV equation examines the case of a train of solitons emerging from one period of a cosine initial condition.

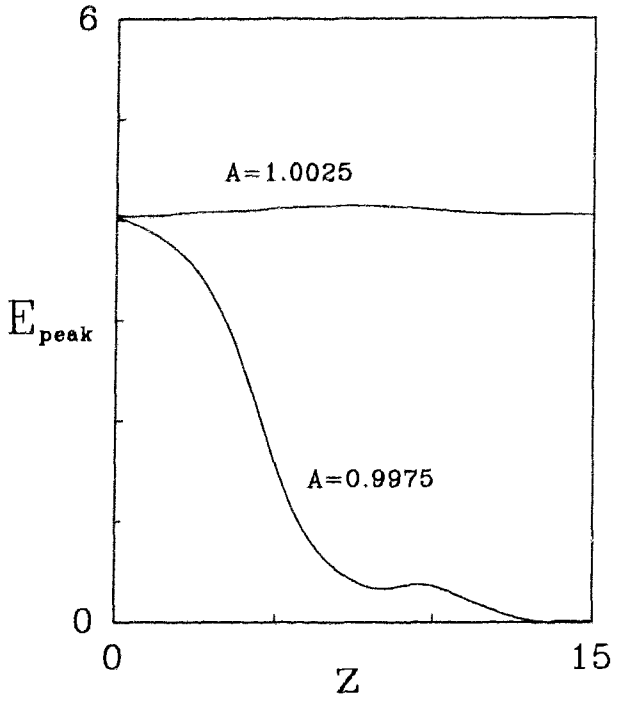

Figure 3.8: Peak height versus z for two amplified profiles bracketing the marginally stable $\beta = 1.03$ light bullet.

localization of energy. The most dramatic examples of this behaviour occur when a radically different envelope configuration leads to light bullet formation as discussed in the literature [Ak92, Ak93a, Ed96] and Chapters 4 and 6 of this thesis.

Of course, if there is insufficient energy available to form the fundamental soliton, decay of the solution is inevitable.[5] As an example, consider the marginally stable solitary wave in Figure 3.4 with $\beta = 1.03$. We can construct nearby initial profiles by letting

$$U(r) \to A\,U(r)$$

where A is a real amplification factor. Figure 3.8 plots the peak height $|E(0,0,0)|$ versus z for two amplitudes bracketing the true solitary wave solution. The profile with $A = 0.9975$ has an energy below that required to form a soliton and so disperses. Conversely, the $A = 1.0025$ pulse has excess energy and drops onto the energy curve, the peak height ringing ever so slightly with behaviour characteristic of one-dimensional breather modes.

[5] Or, at the very least, one cannot form a soliton with a profile that fulfills the spherically symmetric ansatz. However, our experience has been that such solutions disperse into the background.

The ultimate test of solitonic behaviour is stability against massive perturbations in the form of collisions. To study rudimentary collisions, two bullets with propagation constants β_1 and β_2 respectively are placed onto the computational mesh and offset in the t direction at the initial locations $\pm t_0$. Recalling that the mesh is already moving at the group velocity, small deviations[6] from v_g can be introduced by taking input profiles of the form

$$E(t,x,y,z) = U(t-vz,x,y)\,\exp(ivt)\,\exp(i\beta z) \tag{3.15}$$

Substitution of Eq. (3.15) into the GNLSE reveals that with a minor rescaling of the propagation constant β, these travelling solitary waves obey the same radial profile ODE as their stationary counterparts. In order to collide two light bullets, one therefore has the freedom to multiply the individual profiles by $\exp(iv_1t)$ and $\exp(iv_2t)$ with $v_1 \neq v_2$.

Before presenting the results of such a collision, a brief digression on data visualization is necessary. To visualize the dynamics of the simulations in this thesis, volumes of $|E|$ data are stored at equispaced steps in z. These datasets are then volume rendered and concatenated into animations[7] from which selected frames of interest can be printed. A potentially misleading artifact of the rendering process is that in order to peer through the low levels of radiation that permeate the computational mesh, it is necessary to choose a $|E|$ cutoff such that voxels[8] having a field value below this level are rendered transparent. Consequently, the bullets will appear to have well defined edges, however, in order to understand the origin of bullet-bullet interactions, it is important to remember that optical solitons actually have infinitely long tails.

Figure 3.9 shows a sample saturable model collision for two $\beta = 4.0$ light bullets initially positioned at $t_0 = \pm 2$ with opposing velocities $v = \pm 2.0$. (Mesh locations

[6]Using the scaling relationships, Eq. (2.18), one can easily show that in real units, the fractional deviation from the group velocity $(v_g - v_{new})/v_g \simeq v_g v\sqrt{k_0 D}/\sigma$. For the parameters of silica and a 1 ps pulse, $v = 1$ corresponds to a fractional velocity change of only 10^{-6}!

[7]Selected light bullet animations are available on the World Wide Web and can be accessed from <URL:http://www.sfu.ca/~renns/lbullets.html>.

[8]Voxels are the three-dimensional analogue of pixels, or picture elements.

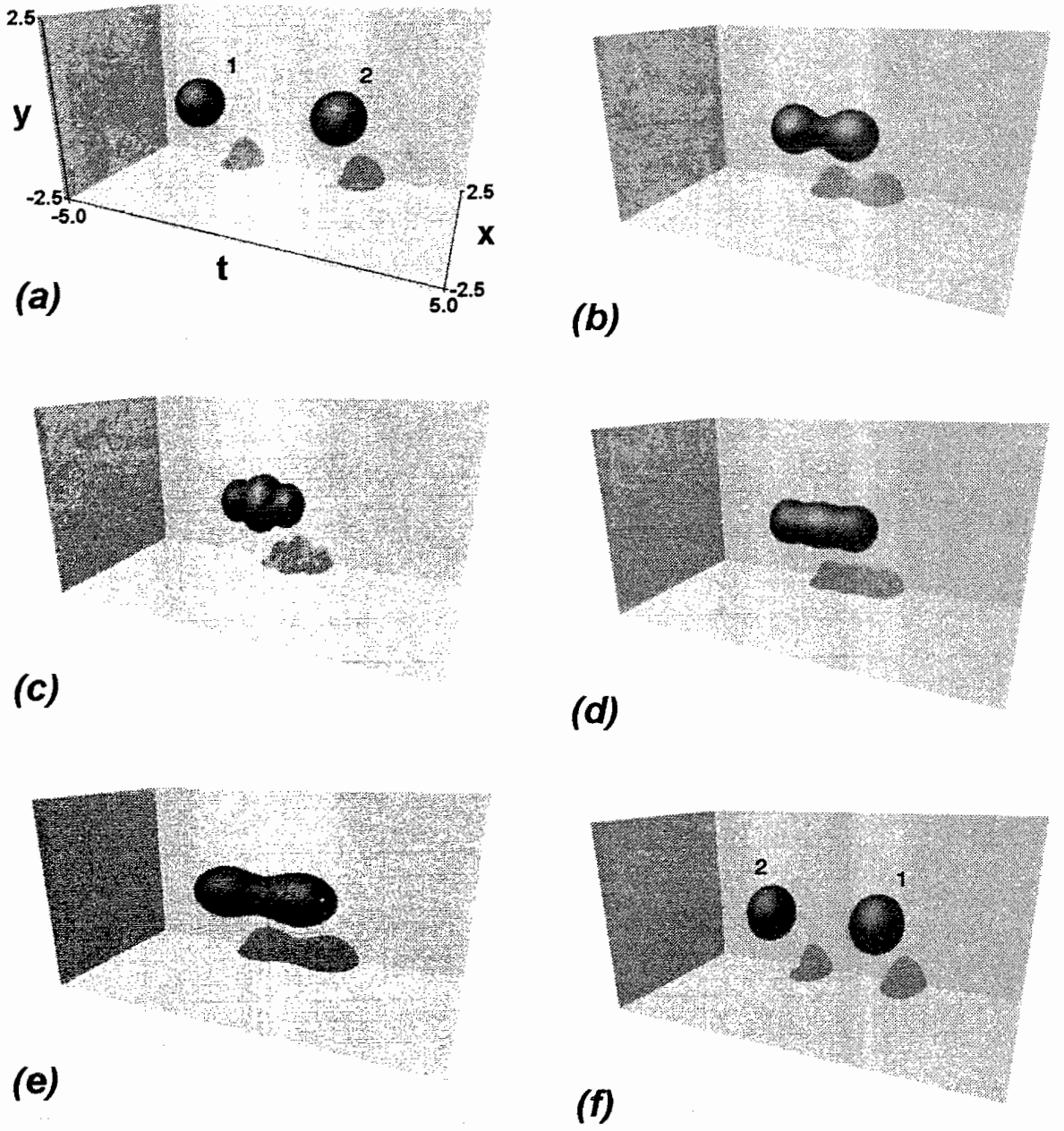

Figure 3.9: Sample collision of two $\beta = 4$ saturable model light bullets demonstrating quasi-soliton behaviour. (a) $z = 0$, (b) $z = 0.61$, (c) $z = 0.85$, (d) $z = 1.12$, (e) $z = 1.55$ and (f) $z = 2.00$. Peak field $|E_{\text{peak}}| = 13.6$ with a transparency cutoff at 5% $|E_{\text{peak}}|$.

of the volume-rendered three-dimensional images with $|E| < 5\%\ |E_{\text{peak}}|$ have been rendered transparent.) Initially in frame (a) the bullets are well separated but moving towards each other such that by frame (b) the pulses are about to collide. Appreciable interaction has already commenced as the leading-edges constructively overlap, raising the local field strength above the visualization threshold. The peak $|E| = 13.6$ value is reached in frame (c) where the central cores of the two solitons completely overlap. The nonlinear nature of the interaction is evident from the two pinched side-lobes that appear and the observation that the peak field is less than twice the initial $U(0)$ values of the isolated solitons although negligible radiation has been shed by this stage of the simulation. By frame (d), the solitons have passed through each other, the left and right-hand lobes moving apart although most of the original energy is still confined to the central bulge.

A three-dimensional animation of the simulation clearly demonstrates the attractive nature of the interaction[9] as the solitons struggle to escape each other before finally separating and regaining their spherical profiles. Viewing such three-dimensional rendered images can easily give the impression that this simulation represents a lossless soliton interaction with equal initial and final states. This is untrue as can be seen by viewing equivalent surface plots of the field values $|E(t, x, y=0)|$. As the collision possesses cylindrical symmetry about the t axis, no loss of information occurs if we take this approach, although visually the explicit three-dimensional character of the light bullets is sacrificed. Surface plots corresponding to the visualizations presented above are displayed in Figure 3.10 and confirm that the final states are reduced in intensity with respect to the initial profiles, the missing energy being shed in the form of radiation faintly visible as small ripples on the surface at frames (e) and (f). The two (small) radiation ripples in frame (e) running parallel to the t-axis are interference effects due to the periodic nature of the boundary. This effect manifests itself first in the t direction due to the shorter transverse distance but is visible in the perpendicular direction at the later frame (f).

[9]To a certain degree, the reader must accept such statements on faith with the understanding that viewing the colour-coded three-dimensional animations of these dynamical simulations truly *does* make the professed behaviour apparent.

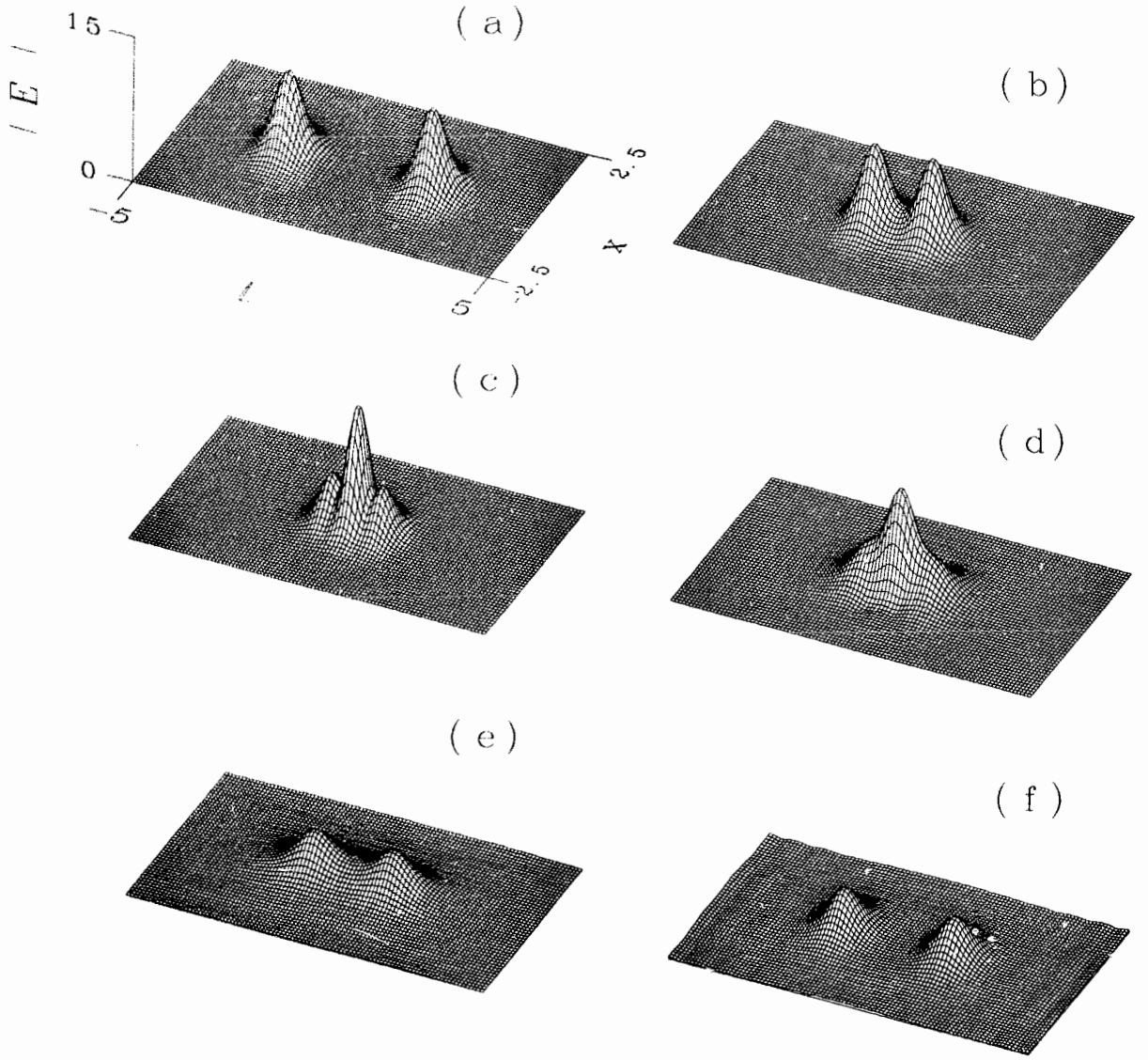

Figure 3.10: Surface plots through the middle of the rectangular mesh in the t-x plane corresponding to Figure 3.9.

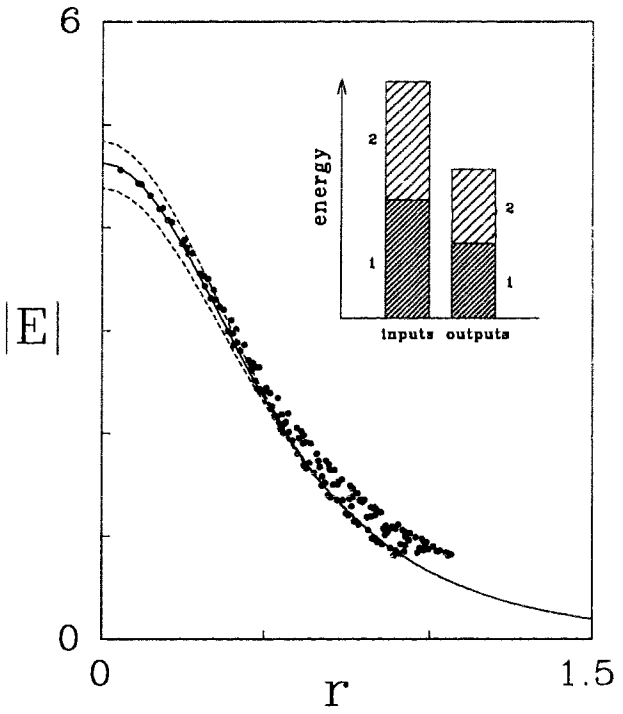

Figure 3.11: $\beta = 1.34$ least-squares fit to the originally right-most $\beta = 4.0$ light bullet in Figure 3.9 after the collision has occurred. Upper and lower dashed lines correspond to profiles with β values $\pm 10\%$ of the fit value. Inset: comparison of energy contained in the input and output states.

Although radiation is shed during the collision process and in the strict sense of the word the emerging light bullets are not true solitons, the wavepackets are certainly soliton-like as they retain their identities after a massive perturbation in which they undergo a strong nonlinear interaction. The output states can be identified by realizing that the only allowable spherical solitons for this medium are characterized by the single parameter β. As β decreases with decreasing energy for stable bullets, the final states should be β-downshifted with respect to the original pulses. Figure 3.11 shows the field data as a function of r for the originally right-most light bullet after the collision at $z = 2.0$. The solid line is a weighted least-squares fit[10] to the $|E(r)|$ data for a downshifted propagation constant $\beta = 1.34$. The upper and

[10]It is tempting to label this process a one-parameter fit in β. Strictly speaking, this is not true as the origin r_0 is also a fitting parameter. That is, on a coarse grid, the peak numerical $|E|$ value does not necessarily occupy the $r = 0$ location for the underlying continuous function it represents. This is equivalent to allowing for uncertainity in the locations of r with the caveat that all mesh locations shift in the same direction and by the same amount. Rather than treat the origin as an explicit fitting parameter for the least squares merit function, we choose r_0 to make the data as smooth as possible without reference to the fitting function. A standard one-parameter least-squares fit then determines the propagation constant. Note, this ordeal is usually not a consideration in low-dimensional problems where the function spans many mesh points.

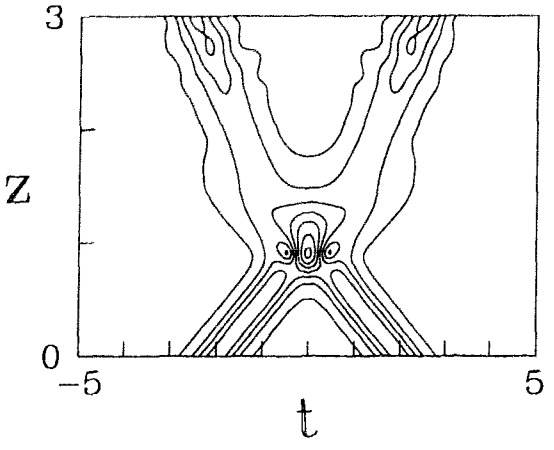

Figure 3.12: Topological soliton track plot for the collision shown in Figure 3.9. Contours begin at $|E| = 1$ and rise by odd integer values.

lower dashed curves have β values with $\pm 10\%$ of this value respectively and serve to indicate the goodness of fit. The left-hand stacked bar in the figure inset depicts the energy contained in the two input pulses (with the numerical labels corresponding to those of Figure 3.9) while the right-hand column plots the energy contained in the two downshifted output pulses,[11] the difference reflecting the amount of the original energy that has been radiated into the background.

A final method of visualizing the collision is the traditional topological soliton "track" plot shown in Figure 3.12. This plot is created from the line of field values $|E(t, 0, 0)|$ as a function of propagation distance z.[12] Before the collision occurs, the light bullet profiles are moving at a constant velocity as indicated by the fixed slope of their respective tracks. After the collision, the solitons emerge travelling at a steeper slope corresponding to a reduced velocity. It is worth noting that this reduced velocity is not required on energy considerations alone as the input velocity v is (within reason) a free parameter and, unlike the KdV soliton, is not correlated to β which determines the radial profile (and thus the energy content). The pulsing behaviour of each light bullet at the top of the plot is due to interactions with the background radiation permeating the computational mesh.

The above simulation suggests many more computational experiments. However,

[11] After fitting the output radial profile to determine β, the pulse energy is obtained from the saturable model energy curve, Figure 3.4.

[12] For three-dimensional simulations, obviously such a plot does result in loss of information.

as this chapter is mainly concerned with the construction of stable light bullet models, further exploration and systematic studies are delayed until the following chapters as we turn now to the construction of bistable light bullet models.

3.3 Bistable light bullets

Bistable solitons have the same energy content but radically different field profiles and are thus the natural carriers of binary information. In fact, we have already encountered an example of bistable solitary waves with the saturable model. Referring back to Figure 3.4, note that the left and right-most solitary waves possess the same energy content but, as shown in the figure inset, have very different radial profiles. Unfortunately, the negative slope solitary wave is radially unstable and thus cannot be put to practical use. To create bistable solitons, it is necessary for the pulses to reside on separate positive slope branches of the energy curve. In order to have pulses with identical energy content, we therefore require a skewed-N-shaped energy curve with two positive slope legs separated by a connecting negative slope branch.

Recall that the sign of $\mathrm{d}P/\mathrm{d}\beta$ is negative, zero, and positive for an I^n model with $n > 2/3$, $n = 2/3$ and $n < 2/3$, respectively. Qualitatively, we therefore require a model that behaves like $I^{2/3}$ or flatter in two regions of intensity with an intervening steep section to create the necessary negative slope leg.

3.3.1 SLSS model

We begin with a somewhat unphysical model that satisfies the above qualitative criterion. The sub-linear + smooth-step (SLSS) model,

$$f(I) = \begin{cases} \mu\sqrt{\frac{I}{I_0}}, & I \leq I_0 \\ 1 - (1-\mu)\sqrt{\frac{I_0}{I}}, & I \geq I_0 \end{cases} \tag{3.16}$$

with $0 < \mu < 1$ has explicit $I^{1/2}$ behaviour at low intensity, a steep portion beginning at $I = I_0$ to yield a negative slope branch, and then saturation at even higher intensities (Figure 3.13). Despite the non-Kerr behaviour near the origin and a cusp

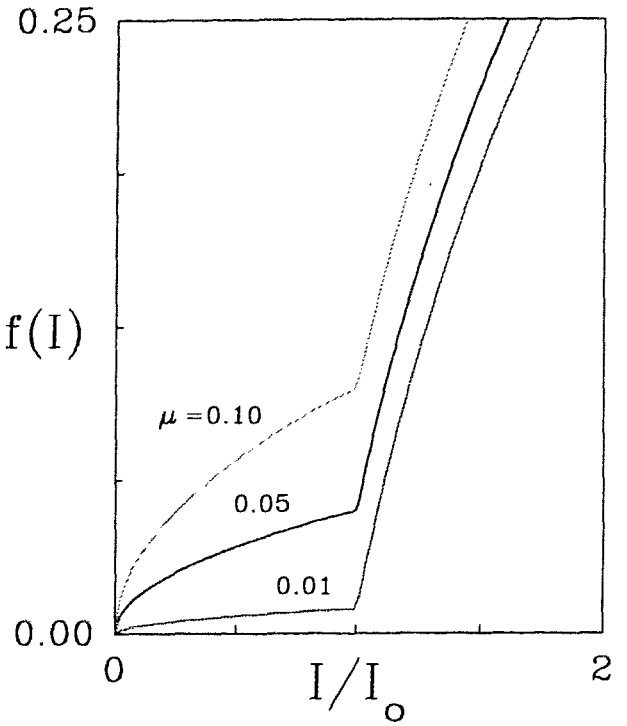

Figure 3.13: The sub-linear + smooth-step (SLSS) nonlinearity ($I_0 = 5$).

at $I = I_0$, the SLSS model is a reasonable starting point in the search for bistable solitons. (As we shall see, a common theme of this thesis is that while the quantitative bullet behaviour may be model dependent, qualitative features such as general stability and interactions are largely model-independent.) Figure 3.14 plots the resultant energy curve for the case of $\mu = 0.05$ and $I_0 = 5$. As expected, the model possesses two regions of positive slope with an intervening negative slope branch. The discontinuity is an artifact of the $f(I)$ cusp at $I = I_0$ and, as will be seen shortly, is easily removed. The two β values indicated have equal energy but, as shown in the figure inset, radically different radial profiles. Solitary waves belonging to the left-most branch are referred to as *low-state* light bullets and are characterized by relatively low intensity centres and wide profiles. Conversely, right-most branch solitary waves are denoted *high-state* light bullets and have very intense centres but relatively compact size.

As this model explicitly fulfills the guidelines for bistability mentioned previously, the qualitative shape of the energy curve is insensitive to the choice of parameters. Figure 3.15 shows energy curves for the three values of μ shown in Figure 3.13.

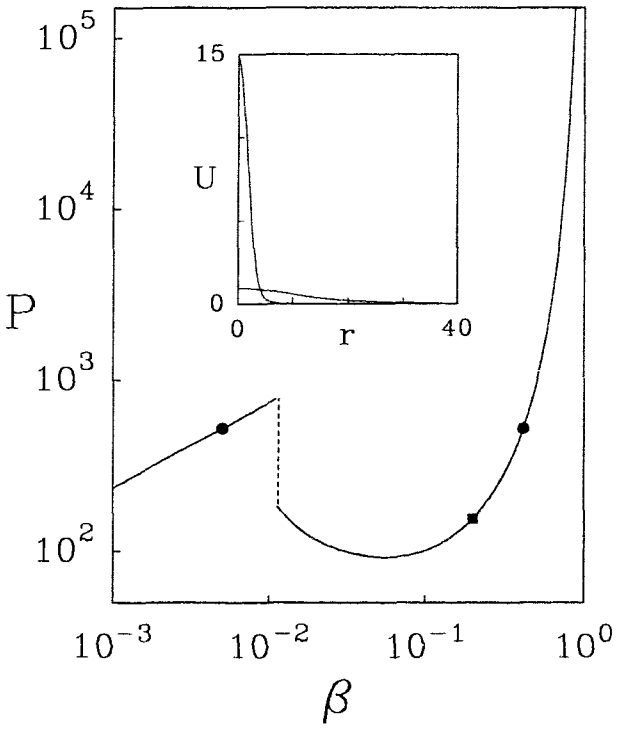

Figure 3.14: Energy curve for the SLSS model with $\mu = 0.05$ and $I_0 = 5$. Inset: Bistable radial profiles for the $\beta = 0.005$ and $\beta = 0.41$ values indicated by filled circles in the main figure.

Qualitatively, the lower leg with explicit $I^{1/2}$ behaviour gives rise to the low-state linear ramp, the steep section after the cusp produces the negative slope in the energy curve, and eventual saturation results in the high-state positive slope branch. The figure also confirms our intuition that weaker nonlinearity requires higher power pulses to produce a similar self-trapped solution.

Copious simulation results are not included here; suffice it to say that simulations of isolated bullets on both positive branches reveal these states to be unconditionally stable to small amounts of noise. In addition (and as expected), solitary waves on the intervening negative slope branch are absolutely unstable and disperse.

As with the saturable model, to show true solitonic behaviour, the bullets should be robustly stable to massive perturbations. Figure 3.16 depicts the successful $v = \pm 0.5$ collision of two high-state $\beta = 0.2$ (filled square on the SLSS energy curve) light bullets with results very similar to those shown for the saturable model.[13] As before, the β values of the final states can be determined by least squares fitting to the

[13]We note that historically this SLSS result preceded numerical work on the saturable model. In fact, this particular simulation is part of the first reported numerical evidence for the stable propagation of three-dimensional optical solitons [Ed92].

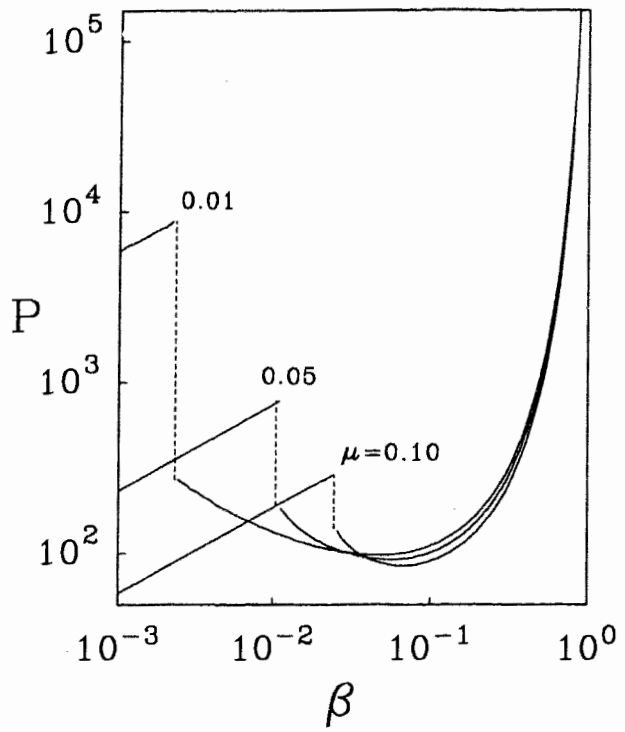

Figure 3.15: SLSS energy curves corresponding to the models shown in Figure 3.13.

available SLSS model profiles and are found to be $\beta = 0.16$ (not shown) corresponding to an energy loss of approximately 30%. This is an another example of collisional downswitching from one soliton state to another.

With drastically disparate sizes, one can envision a host of possible computational experiments and, accordingly, a selection of novel results is presented in Chapter 4. Here, to continue with bistable model building, we consider an $f(I)$ function that removes some of the unphysical defects of the SLSS model.

3.3.2 DSKC model

The double-saturable Kerr-cubic (DSKC) model,

$$f(I) = \begin{cases} 1 - \exp(-I), & I \leq I_0 \\ C + \frac{A}{B + (I_0/I)^3}, & I \geq I_0 \end{cases} \tag{3.17}$$

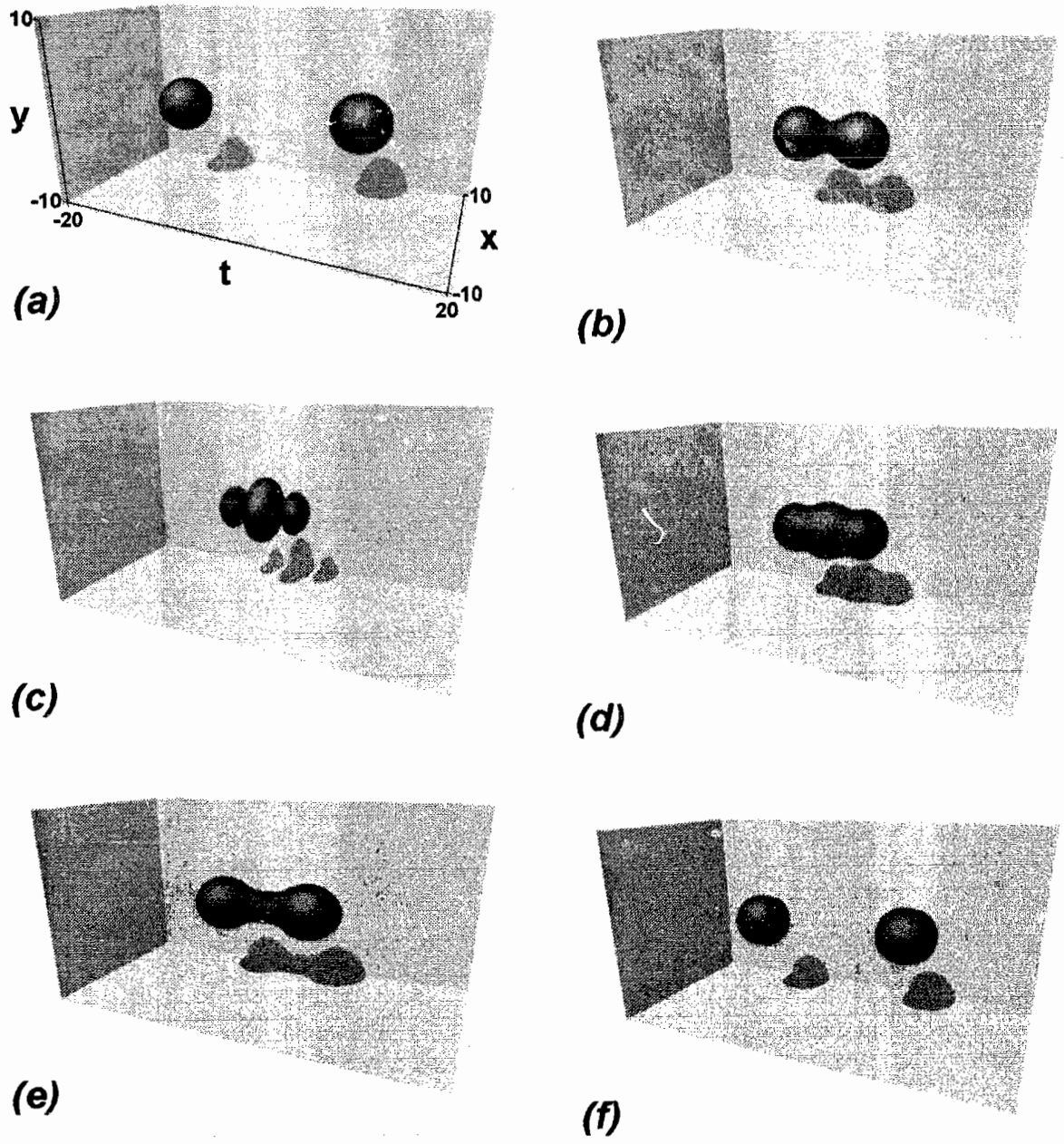

Figure 3.16: Sample collision of two high-state SLSS model light bullets demonstrating quasi-soliton behaviour. (a) $z = 0$, (b) $z = 13.2$, (c) $z = 19.2$, (d) $z = 22.2$, (e) $z = 30.6$ and (f) $z = 42.0$.

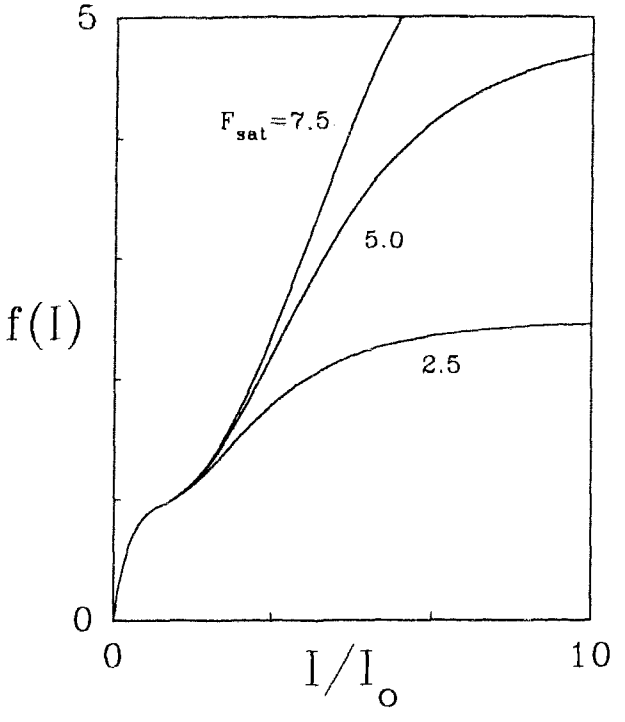

Figure 3.17: The double saturable Kerr-cubic (DSKC) nonlinearity. (Eventual saturation of the top-most curve is not apparent due to the figure scale.)

where the positive parameters A, B and C are defined by

$$\begin{aligned} B &\equiv \frac{I_0}{3[(F_{\text{sat}}-1)\exp(I_0)+1]-I_0} \\ A &\equiv B(1+B)[(F_{\text{sat}}-1)+\exp(-I_0)] \\ C &\equiv F_{\text{sat}}-\frac{A}{B} \end{aligned}$$

with F_{sat} and I_0 being adjustable model parameters. As shown in Figure 3.17 for various F_{sat} with $I_0 = 3$, one should not be disturbed by the apparent complexity of the model parameters A, B and C; these wieldy expressions simply ensure that the first derivative of $f(I)$ is continuous at $I = I_0$. A Taylor expansion of the $I < I_0$ branch about $I = 0$ yields linear behaviour at the origin which is a desirable result as existing nonlinear media exhibit Kerr-like behaviour; based on previous experience, we expect that this region of the model will yield negative slope for the energy curve. The lower leg then has a plateau which, if sufficiently flat, should result in a positive slope branch on the energy curve. For $I > I_0$, the model is steep slightly above the transition point but saturates at still higher intensities which can result in an

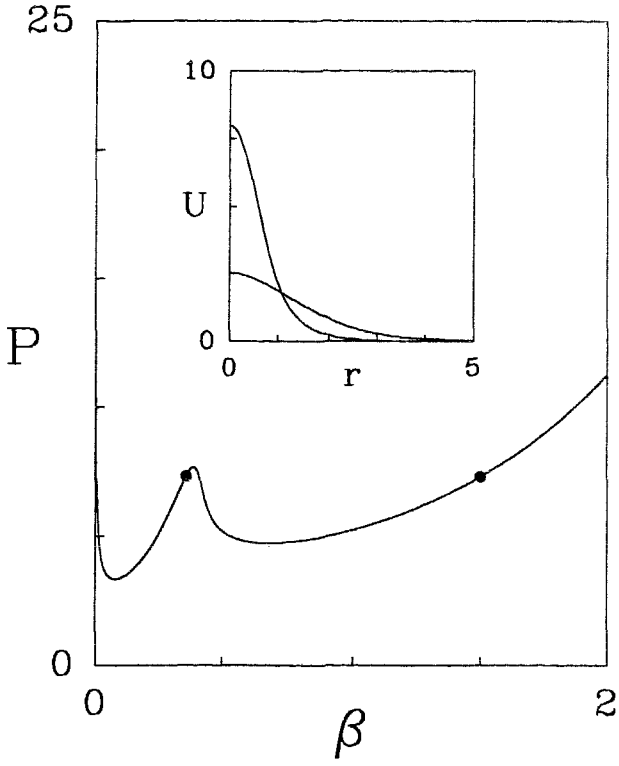

Figure 3.18: Energy curve for the DSKC model with $I_0 = 3$ and $F_{\text{sat}} = 3$. Inset: Bistable radial profiles for the $\beta = 0.36$ and $\beta = 1.5$ values indicated in the main figure.

additional U-shaped section of the energy curve. For appropriate choices of the two model parameters, such a double-saturating nonlinearity should result in a skewed W-shaped energy curve with two positive and two negative slope branches. Figure 3.18 shows the energy curve obtained for $I_0 = 3$ and $F_{\text{sat}} = 5$ with the inset depicting the radial field profiles for the sample bistable solitary wave pair $\beta = 0.36$ and $\beta = 1.5$.

The energy curves for the three parameter variations depicted in Figure 3.17 are shown in Figure 3.19 where it can be seen that if the saturation intensity is too low, the second leg of the model is insufficiently steep to yield the necessary negative slope branch, thus precluding bistability.

3.4 A brief word on fabrication considerations

While the three-dimensional solitary wave solutions of the GNLSE studied in this thesis are of intrinsic interest solely as an intriguing applied mathematics problem, if we wish to observe light bullets in the laboratory, then some discussion of the

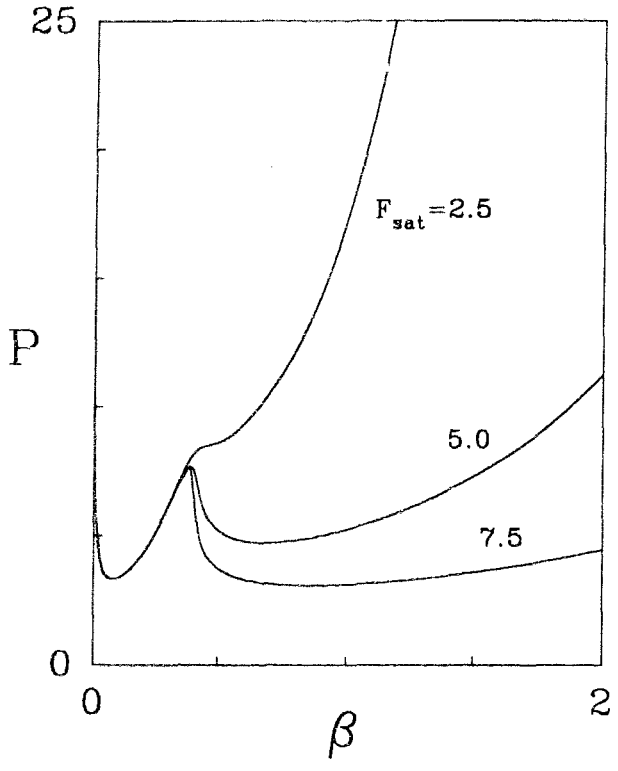

Figure 3.19: DSKC energy curves corresponding to the specific models shown in Figure 3.17.

materials problem must be advanced.

While the Kerr nonlinearity, $f(I) = I$, is characteristic of many existing nonlinear materials, in Section 3.1 we demonstrated that for this case, stable light bullets were not possible. Further, to rectify this instability, it was found that the model should display I^n behaviour with $n < 2/3$. However, based on (i) our knowledge that Kerr behaviour is apparent at "low" intensities, and (ii) a desire to avoid explicit sub-linear behaviour, we were naturally led to consider the saturable model

$$f(I) = \frac{I}{1 + aI} \tag{3.18}$$

for which robustly stable light bullets were then numerically propagated. While media exhibiting saturable behaviour are known to exist (see, e.g., Refs. [Ca91, Co91]), an important issue is the timescale with which such nonlinearities respond. Often, as with a typical two-level system, saturation involving real particle populations occurs on a nanosecond timescale (although Coutaz and Kull reported a 7 ps lifetime in a darkened semiconductor doped glass [Co91]); in such cases, the assumption of instantaneous

nonlinear response is patently untrue.

However, Taylor expanding and truncating the saturable model reveals that for reasonable intensities, its behaviour is qualitatively similar to a polynomial model

$$f(I) = I + \alpha I^2 \tag{3.19}$$

with $\alpha < 0$ which is *precisely* the form one would obtain by considering a negative $\chi^{(5)}$ contribution to the nonlinear polarization [Pi74]. In this case, the response is strictly a polarization effect and would therefore be sufficiently fast to satisfy the assumptions used in deriving the GNLSE. In addition, there is no physical restriction that α be positive. For example, as discussed by McLeod and co-workers [Mc95] in the context of light bullets, recent measurements of organic nonlinear materials such as p-toluene sulfanate (PTS) have found large positive n_2 and negative $n_4 \equiv \chi^{(5)}/2n_0$ at wavelengths of optical interest [La94].

Let us briefly address the usual criticisms about the apparent unphysical behaviour (e.g., cusps of step-models) or complexity (e.g., the algebraic form of the DSKC model) of the bistable nonlinear refractive index functions introduced earlier. Theoretically, certain step and polynomial models in one dimension are attractive because the initial solitary wave profiles can be analytically determined. The algebraic complexity is simply the result of desiring a smooth model displaying the qualitative dual saturation features seen for both the SLSS and DSKC models. It never ceases to amaze us that people fixate on the specifics of the model, ignoring the exciting fact that wildly disparate $f(I)$ possessing a few key features give qualitatively similar quasi-soliton results!

It is far beyond the scope of this thesis to consider the materials science problem of fabricating bistable soliton supporting media. However, Enns and Edmundson [En93] have attempted to diffuse some of the criticism by showing that rather than search for a single exotic material possessing the desired $f(I)$, it is possible to achieve the same result by combining three properly chosen single saturable media.

As we shall demonstrate in the chapters that follow, a recurrent theme of this thesis is that the light bullet phenomenon does not rely on a specific model and

particular choice of parameters, requiring only that the underlying model satisfy the $\mathrm{d}P/\mathrm{d}\beta$ stability criterion.

Chapter 4

Novel soliton interactions

In the previous chapter, three nonlinear refractive index models were introduced and shown to support the propagation of three-dimensional optical solitons. While the simplest physically realizable model, a saturable nonlinearity, admits a continuous spectrum of stable light bullets, the more complex SLSS and DSKC models possessing two saturable jumps admit bistable light bullets, solitary waves with the same energy content but radically different radial profiles.

In this chapter, we present a representative sample of novel results obtained with the three-dimensional beam-propagation code used to solve the generalized nonlinear Schrödinger equation for an arbitrary initial optical envelope configuration. The intent of these results is to demonstrate and reinforce:

- That the extra degrees of freedom intrinsic to the three-dimensional problem can result in novel effects that have no one-dimensional analogue.
- That saturable media have a natural tendency to form optical solitons. That is, in the space of all envelope functions, light bullets are attractors to nearby functions.

Unfortunately, with limited access[1] to the supercomputing power necessary to

[1]The HPCC scholarship program allots 100 hours of cpu time per year to scholarship holders on the 2.5 Gigaflop Fujitsu VPX 240/10.

carry out these simulations, one has to be extremely selective about systematic studies. Our approach has been to balance systematic studies (Chapters 5 and 6) with an exploration of the rich parameter space of the light bullet problem. It is worth emphasizing that while only a selection of results are presented below, all such simulations have been repeated both for different model parameters and, in the case of the bistable light bullets, for one or more different models. In four years of simulations, we have yet to encounter a simulation scenario where the qualitative results are highly model or parameter dependent. That this occurs for models that are quantitatively dissimilar leads us to infer that light bullet propagation is indeed a universal phenomenon, requiring only that the underlying nonlinear model fulfill the minimal $\mathrm{d}P/\mathrm{d}\beta$ stability condition.

4.1 Soliton fusion

Figure 1.2(a) in the introduction of this thesis depicts the periodic temporal collapse of solitons for the integrable one-dimensional NLSE. For the exactly analogous situation of one-dimensional spatial solitons, a simple Snell's law argument explains the interaction in terms of each soliton "bending" in the direction of the increasing refractive index produced by the existence of its soliton neighbour. Gordon [Go83] has analytically determined the interaction force between initially overlapping one-dimensional solitons, a point we will return to in Chapter 5. Such endless oscillatory behaviour will only occur in a nonlinear medium if the pulses are true soliton solutions. However, if radiative losses occur, one might expect the amplitude of the oscillation to slowly decay or, in the case of an overdamped system, to decrease rapidly and monotonically to zero. While both of these scenarios result in fusion of the two initially separated bullets, it is not at all obvious that the final result will be a stable fused state - this is a conjecture that must be confirmed by numerical experiment.

Returning to the collision of the two $\beta = 4$ saturable model light bullets discussed in Chapter 3 and depicted in Figure 3.9, the attractive force is apparent in frames (d) and (e) where the bullets have passed through one another and are struggling to escape the induced attractive potential. The intent of this simulation was to demonstrate

quasi-soliton collisional behaviour analogous to that seen for true one-dimensional situations (e.g., KdV or NLSE). However, in light of the above discussion, we can now admit that below the specific incident velocities for this simulation, a threshold velocity v_c exists beneath which the emerging solitons are unable to break free of the attractive binding potential.

As an example, consider Figure 4.2 which shows volume rendered images for a simulation identical to that of the previous chapter but with incident velocities $|v| = 1.6$ which are slightly below the critical value. The initial stages of the simulation have been omitted, the evolution preceding the first frame being equivalent to that of Figure 3.9 up until frame (d). The light bullets initially pass through one another displaying quasi-soliton behaviour; however, by frame (c) the attractive force due to the overlapping tails has brought the bullets to a complete standstill. The propagation parameter of these isolated solitons can be determined by least-squares fitting the profiles and is found to be $\beta = 3.1$ (not shown), the energy lost to background radiation at this stage of the simulation being a mere 18%. Beyond this point, the attractive force due to the overlapping tails (which are not apparent in this figure) causes the separated pulses to coalesce into a single stable fused soliton state.

Figure 4.2 is a topological contour plot of the simulation, indicating that the final fused state is pulsating. To aid in the visualization of this phenomenon, Figure 4.3 shows the field intensity at the centre of the computational mesh as a function of the propagation distance z. Initially $|E(0,0,0)|$ is zero when the two light bullet are at their starting locations of $t_0 = \pm 2$. The first large peak occurs when the light bullets meet and pass through one another. Soliton fusion is indicated by the rise preceding the point labelled 'a' which corresponds to the set of concentric rings on the contour plot at $z \simeq 5$. The fused soliton then undergoes a series of oscillations, least-squares fitting of the field profiles being able to determine the instantaneous propagation parameter at the points 'a', 'b', 'c' and 'd'. Based on the observance of only several periods of the slowly decaying envelope, can we assert that this pulse is relaxing to an asymptotic state? Unfortunately, the results of the simulation are questionable beyond $z = 8$ due to interference from the 50% of the original energy

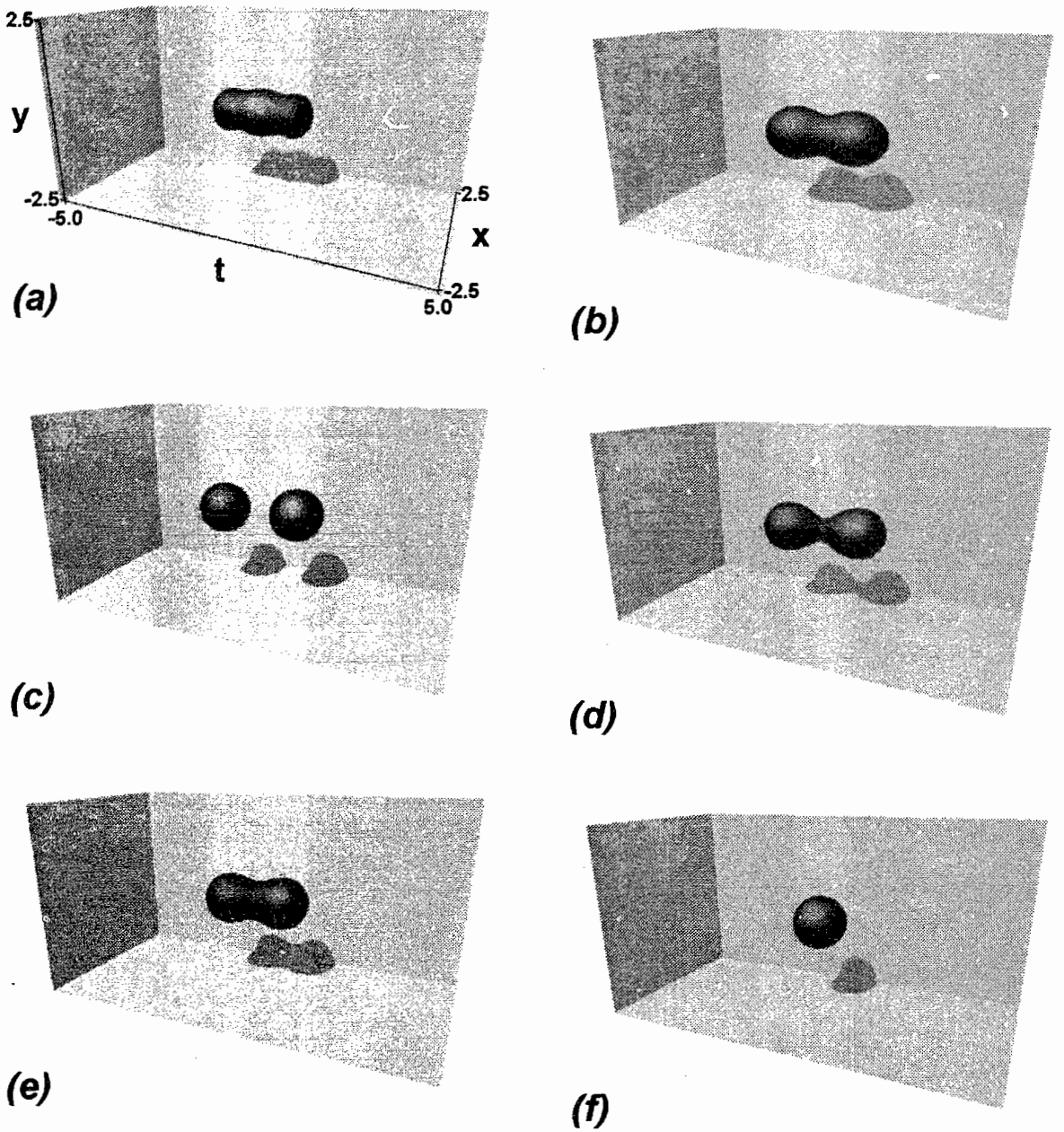

Figure 4.1: Fusion of two saturable model light bullets with velocities below v_c. Note that in frame (a), the simulation is already well underway, qualitatively corresponding to frame (d) in Figure 3.9. (a) $z = 1.30$, (b) $z = 1.85$, (c) $z = 3.00$, (d) $z = 3.64$, (e) $z = 4.19$ and (f) $z = 5.75$. Peak $|E| = 13.4$.

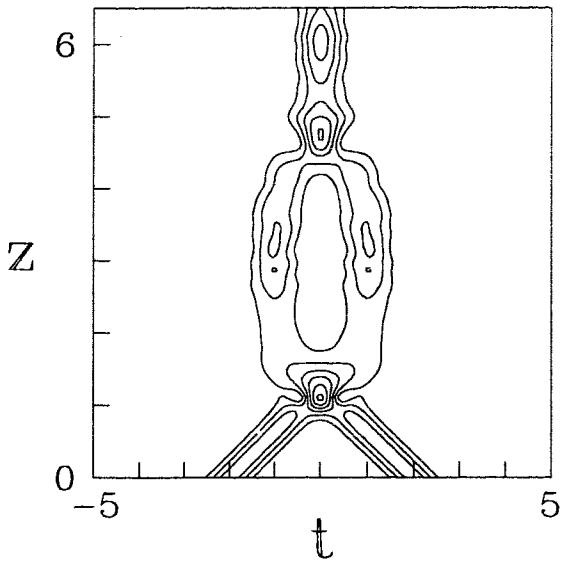

Figure 4.2: Topological soliton track plot for the collision shown in Figure 4.1. Contour levels begin at $|E| = 3$ and rise by odd integers.

that has been released as background radiation.[2] However, as we shall see later for the case of bistable soliton switching, such ringing patterns typically do decay and it is thus reasonable to take the propagation constant at either point 'b' or 'd' as an approximation to the asymptotic soliton state.

In the $v > v_c$ quasi-soliton collisions of two light bullets discussed so far, a significant amount of energy was dissipated into the surrounding medium, the energy being released as an outgoing continuum of radiation. Alternatively, the radiation may be cast off in a quantized form. Consider, for example, the collision of two high-state $\beta = 0.41$ SLSS light bullets with opposing velocities $v = \pm 1.6$ as depicted in Figure 4.4. Given the earlier results, frames (a) through (c) should be familiar; the bullets pass through one another and undergo a nonlinear interaction. By frame (d) the tails of the outgoing light bullets still overlap resulting in an attractive binding of the soliton pair that retards their attempt to separate. Beyond this point, the interaction is manifestly different. Whereas the bound pair often separate with a parting "snap" of the overlapping tails, here we see the tails pinching off to form a third isolated soliton. The truly remarkable aspect of this simulation is that, while

[2]The fusion process also contributes to the total energy loss.

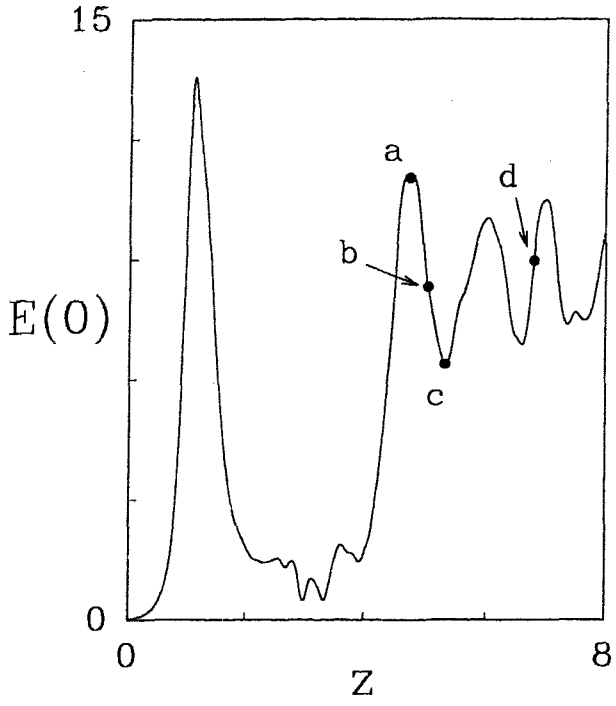

Figure 4.3: Central field value $|E(0,0,0)|$ versus z shows relaxation of the fused soliton state.

fitting of the final states (Figure 4.5) reveals that the outgoing solitons are down-shifted, as shown by the figure inset the energy difference is completely accounted for by the energy of the newly-formed stationary central light bullet! The pinching can be qualitatively understood based on the investigations of Akhmediev and co-workers [Ak92, Ak93a] into the temporal modulation instability of a continuous-wave (cw) beam in a saturable nonlinear medium. That is, if we loosely consider the optical envelope at frame (d) to be a section of a homogenous cw beam with sufficient energy to form three solitons, such a configuration is susceptible to an exponentially growing longitudinal modulation with a wavelength that will pinch the beam in the two locations shown in frame (e). This interpretation does not answer two key questions: (i) why is so much of the outgoing pulse energy trapped in the central region, and (ii) how does this process eliminate the typical emission of radiation from the front of the outgoing pulse? Even though the emerging original pulses are β-downshifted, the fact that the lost energy is almost entirely contained in the newly formed third soliton may make this a system worthy of analytical analysis by those researchers better prepared to do so. Finally, for completeness, Figure 4.6 depicts the soliton contour plot for this

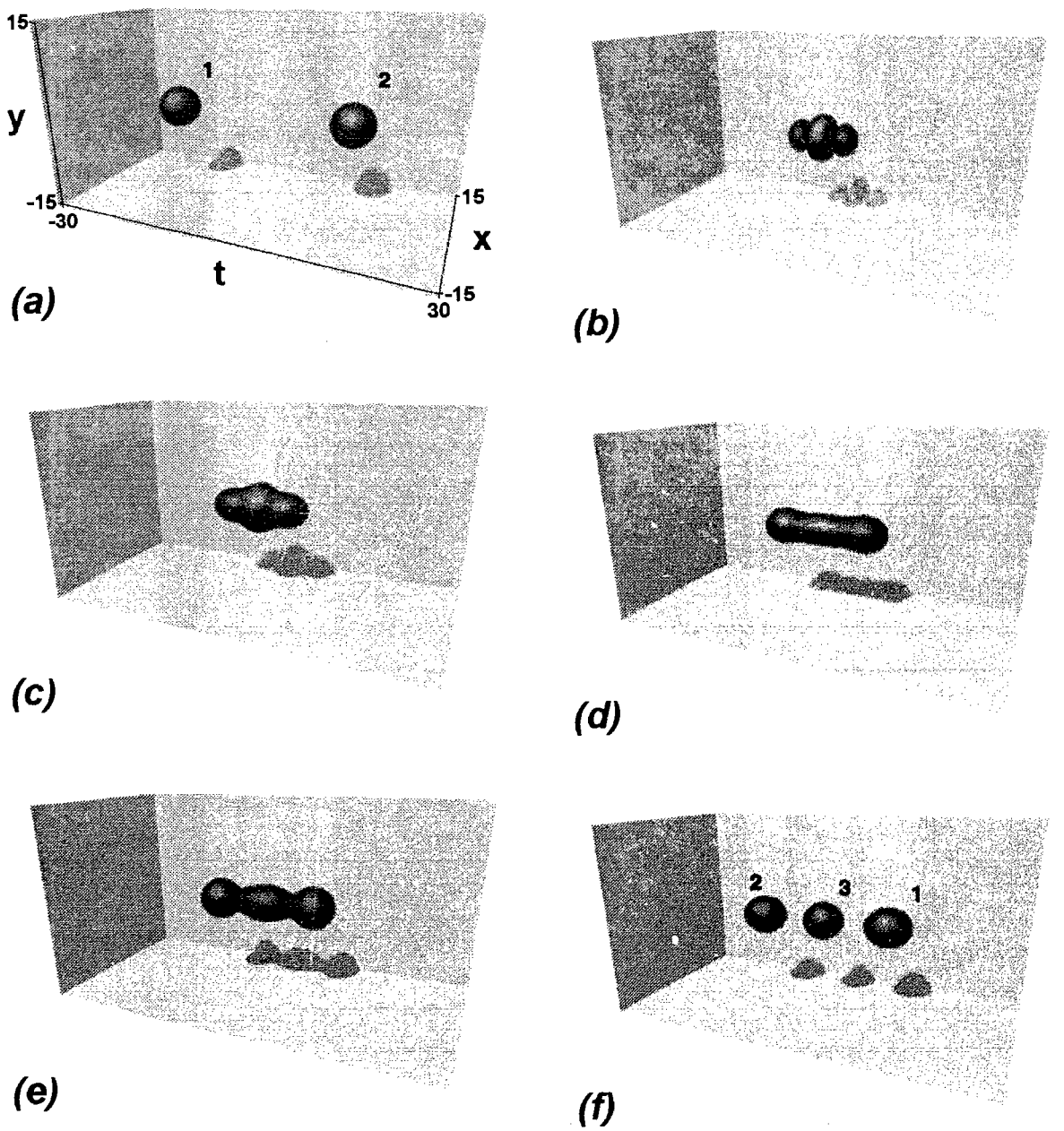

Figure 4.4: Radiationless quasi-soliton collision of two high-state SLSS light bullets yields production of a third stationary bullet. (a) $z = 0$, (b) $z = 29.6$, (c) $z = 32.8$, (d) $z = 39.2$, (e) $z = 44.8$ and (f) $z = 55.2$.

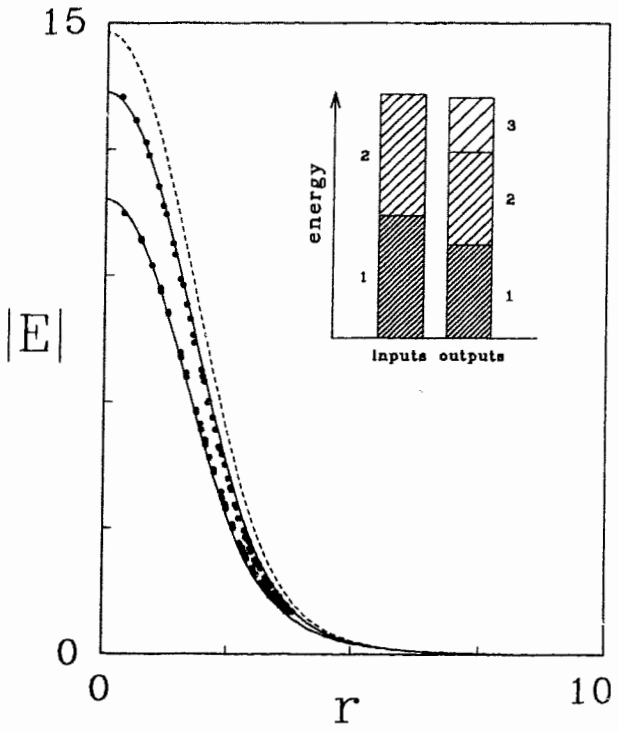

Figure 4.5: Least-squares fits of the final soliton profiles. Dashed curve: original $\beta = 0.41$ input states. Top solid curve: down-shifted $\beta = 0.37$ output profiles. Lower solid curve: stationary soliton. Inset: schematic energy transitions.

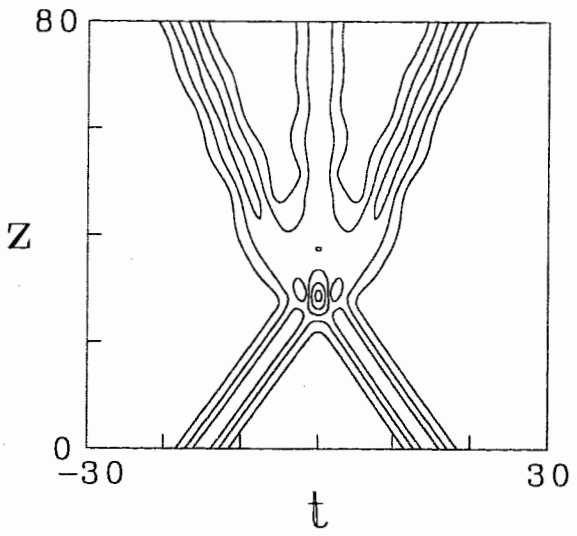

Figure 4.6: Contour plot corresponding to Figure 4.4 soliton production simulation. Contour levels begin at $|E| = 2$ and rise by 5 with each interior line.

interaction. The familiar slowing-down of the outgoing pulses is clearly evident.

4.2 Soliton tunnelling

Recall that a key feature of bistable models is that the two positive slope branches produce light bullets with radically different radial intensity profiles. For example, referring back to the SLSS model energy curve Figure 3.14, we see that the bistable light bullets $\beta = 0.005$ and $\beta = 0.41$ have equal energy content but grossly disparate $U(r)$ profiles.

As shown in Figure 4.7, one of the more spectacular three-dimensional simulations occurs when a pair of bistable light bullets is involved in a collision process. In frame (a) the low-state soliton is placed at the centre of the computational mesh with zero initial velocity (with respect to the group velocity) while the high-state light bullet begins its journey at $t_0 = -50$ with velocity $v = 0.5$. As can be seen from this sequence of images,[3] the compact, intense, high-state bullet succeeds in tunnelling through the relatively larger and less intense low-state bullet, both displaying soliton-like behaviour.

Due to the greyscale cutoff, what cannot be observed in this sequence is the series of hemispheric shock waves that precede the tunnelling bullet. The moving bullet displaces energy in its immediate path, resulting in the formation of the circular bulges apparent in frame (c). These "bow waves" travel to the right and are emitted into the surrounding volume as radiation. As we shall see, this lost energy is solely to the detriment of the large stationary bullet.

To allow visualization of the shock waves, Figure 4.8 shows the surface[4] $|E(t, x, 0)|$ at a propagation distance slightly after frame (c) such that the two shocks have now propagated to the front of the system and are about to be radiated away. We admit to having little understanding about the origin of these shocks and can only note that their characteristic wavelength is of the same order as the size of the travelling

[3]Which certainly do not do justice to the original colour animations!

[4]Note that a majority of the high-state bullet's peak height of $|E| = 14.7$ has been cropped, the reduced scale facilitating viewing of the low-level radiation.

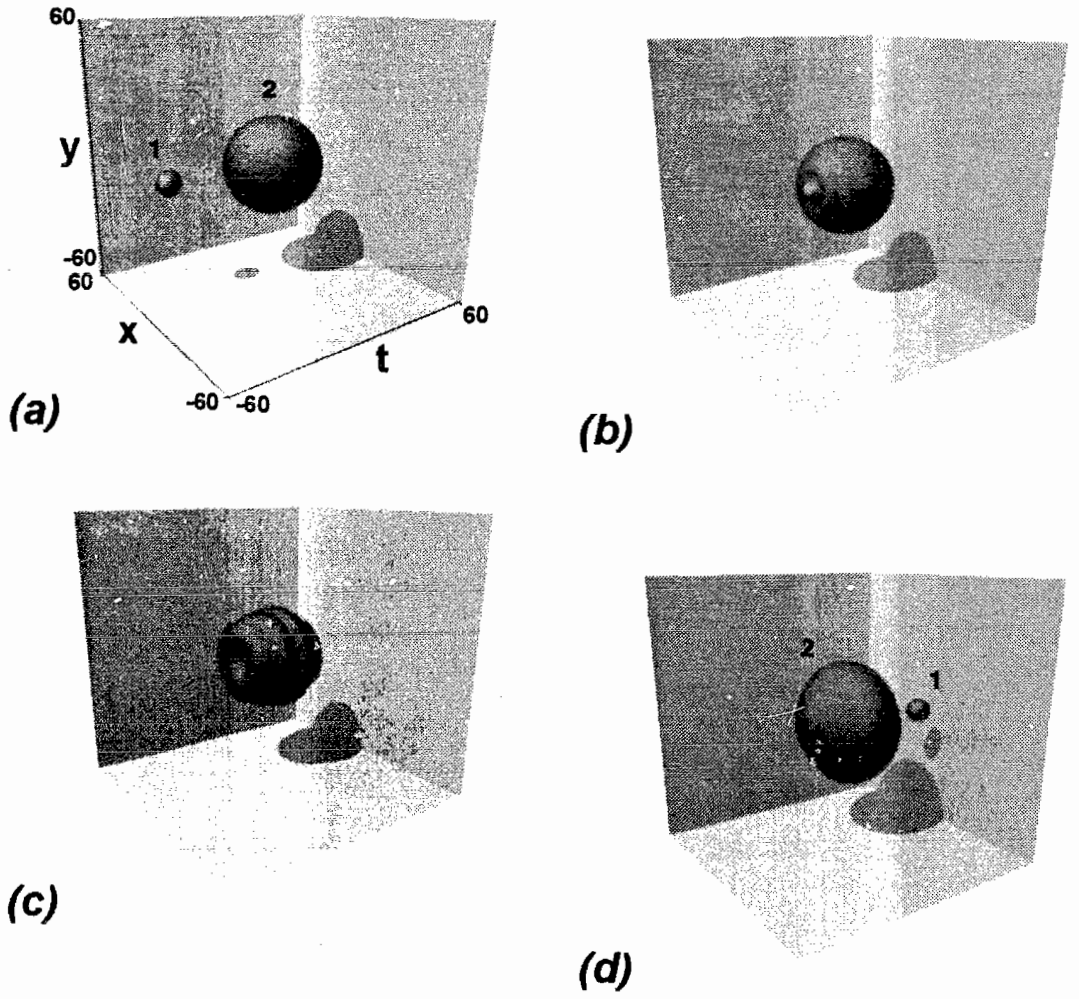

Figure 4.7: Bistable tunnelling: a high-state SLSS light bullet bores through a low-state state light bullet. (a) $z = 0$, (b) $z = 68$, (c) $z = 102$ and (d) $z = 200$. Peak $|E| = 16.1$. Due to the grossly disparate sizes of the two bullets, the data has been nonlinearly scaled to make the low $|E|$ features more prominent. The transparency cut-off occurs for $|E| = 0.17$, 18% of the low-state soliton's peak height.

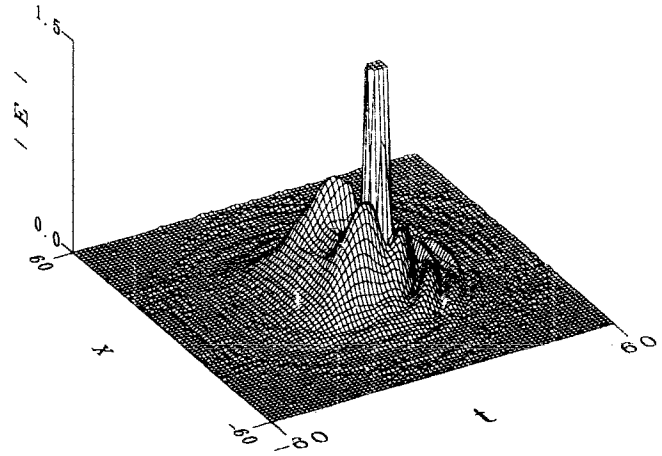

Figure 4.8: Surface plot of $|E(t,x,0)|$ after frame (c) ($z = 128$) in Figure 4.7 showing "bow wave" formation in front of burrowing high-state light bullet.

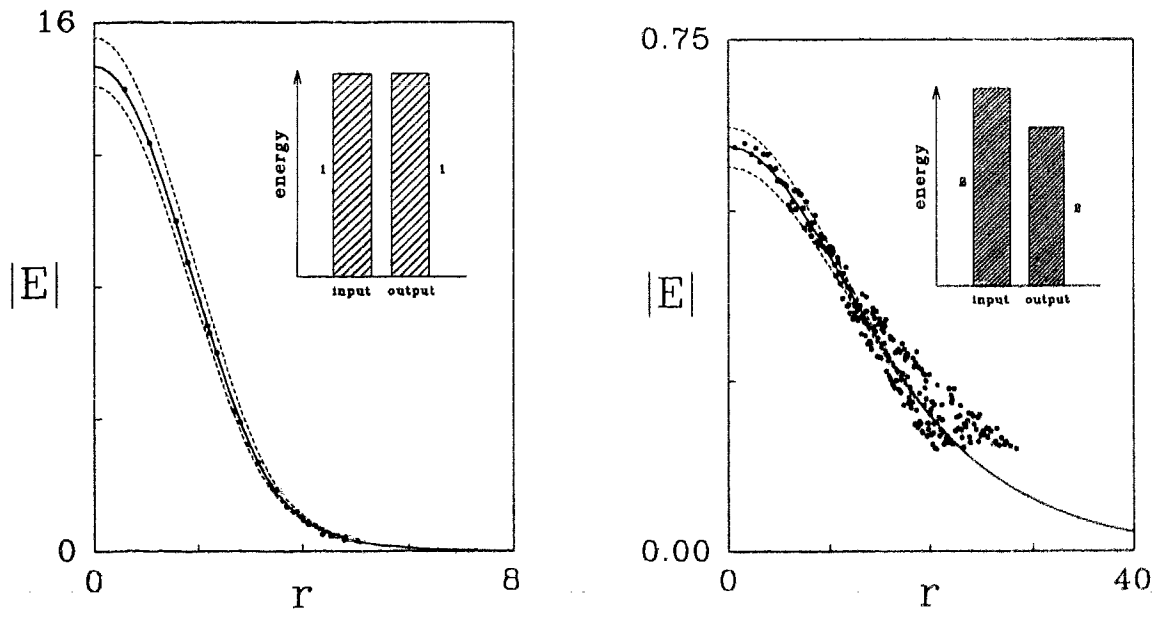

(a) $\beta = 0.41$ (b) $\beta = 0.0032$

Figure 4.9: Post-collision ($z = 220$) least-squared fits to the light bullet profile data. Upper and lower dashed lines are $\beta = \pm 5\%$ of the fit value. Inset: schematic energy transitions.

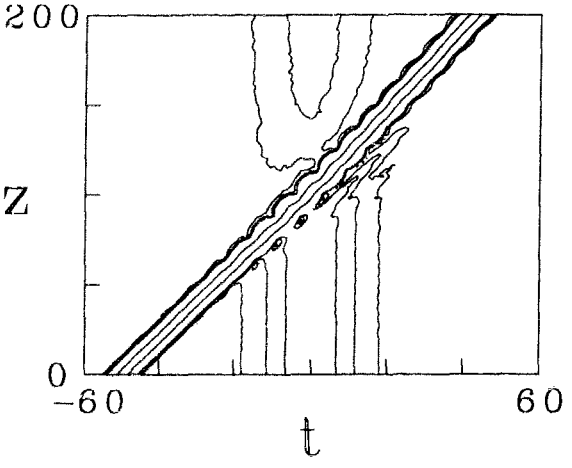

Figure 4.10: Contour plot of $|E(t,0,0)|$ reveals slight slowing down of the high-state light bullet. Contour levels at $|E| = 0.25$, 0.5, 0.75 and 1.00.

soliton. In this figure, the $|E|$ depression left in the wake of the travelling bullet, which is the energy source of the emitted waves, is clearly apparent and we therefore expect downswitching of the stationary soliton and little or no change to the travelling bullet. This is confirmed by performing a least-squares fit of the final radial profiles (Figure 4.9). The energy of the high-state soliton is conserved while the propagation parameter of the stationary low-state bullet is downshifted from $\beta = 0.005$ to $\beta = 0.0032$ corresponding to an energy loss of 20%. The low-state data points are widely strewn due to asymmetry of the final state, the stationary bullet becoming temporarily oblate due to the impact of the other bullet.

Finally, does the collision have any discernible effect on the travelling bullet? Indeed, while the bullet energy remains fixed, its velocity is slightly reduced as can be seen[5] by referring to the contour plot Figure 4.10.

4.3 Glancing incidence: spiralling light bullets

While, in our opinion, the simulations depicted so far are striking, they share the common trait of possessing a collisional symmetry axis and thus the inherent freedom

[5]The deviation is best seen by staring directly along the soliton track just above the plane of the paper. (Not an exercise for the astigmatically inclined.)

of three spatial dimensions has not been fully exploited. Therefore, consider Figure 4.11(a) in which two $\beta = 4$ saturable model light bullets with opposing velocities $v = \pm 1.6$ are initially offset in both the *t and x* directions. For future reference, in physics the transverse offset distance between the bullet centres is known as the *impact parameter* which we denote by the symbol b. For this particular choice of impact parameter, $b = 1.625$, the bullets pass at grazing incidence but, as seen in frame (b), the overlapping tails create an attractive force that deflects each bullet from its otherwise straight-line path. As seen in the subsequent images, the light bullets enter into orbit around a common centre. By frame (e), it is clear that due to radiative energy losses as they orbit, the distance between the soliton centres is decreasing until, by frame (f), the two light bullets have merged into a single rotating soliton state! The reader may well ask: how can a spherical envelope be said to rotate? While asymptotically the soliton assumes a spherical profile, during the relaxation process, deviations[6] from the eventual spherically symmetric state can be seen to precess on the soliton surface. (This relaxation process can be quantified by a spherical harmonic decomposition of the envelope versus z, the harmonic analysis determining deviations from perfect sphericity.) Finally, as shown in Figure 4.12, the propagation constant of the final state can be ascertained by a least-squares fit of the fused profile, and is found to be upswitched to $\beta = 5.45$ as schematically indicated in the figure inset.

For this particular choice of initial propagation constants and velocities, increasing the impact parameter slightly to $b = 1.65$ results in the solitons orbiting each other but not coalescing (Figure 4.13), leaving the interaction region with equal and opposite transverse components to their velocities. (In the laboratory frame of reference, these small transverse velocity components manifest themselves as a sideways drift superimposed on the fast longitudinal motion.)

This set of simulations leads one to consider the creation of a stable orbiting soliton pair. Alas, this does not seem to be possible as radiative losses cause the size of the orbit to decay with propagation distance resulting in eventual soliton fusion.

[6]To put it rather crudely, "bumps" on the surface.

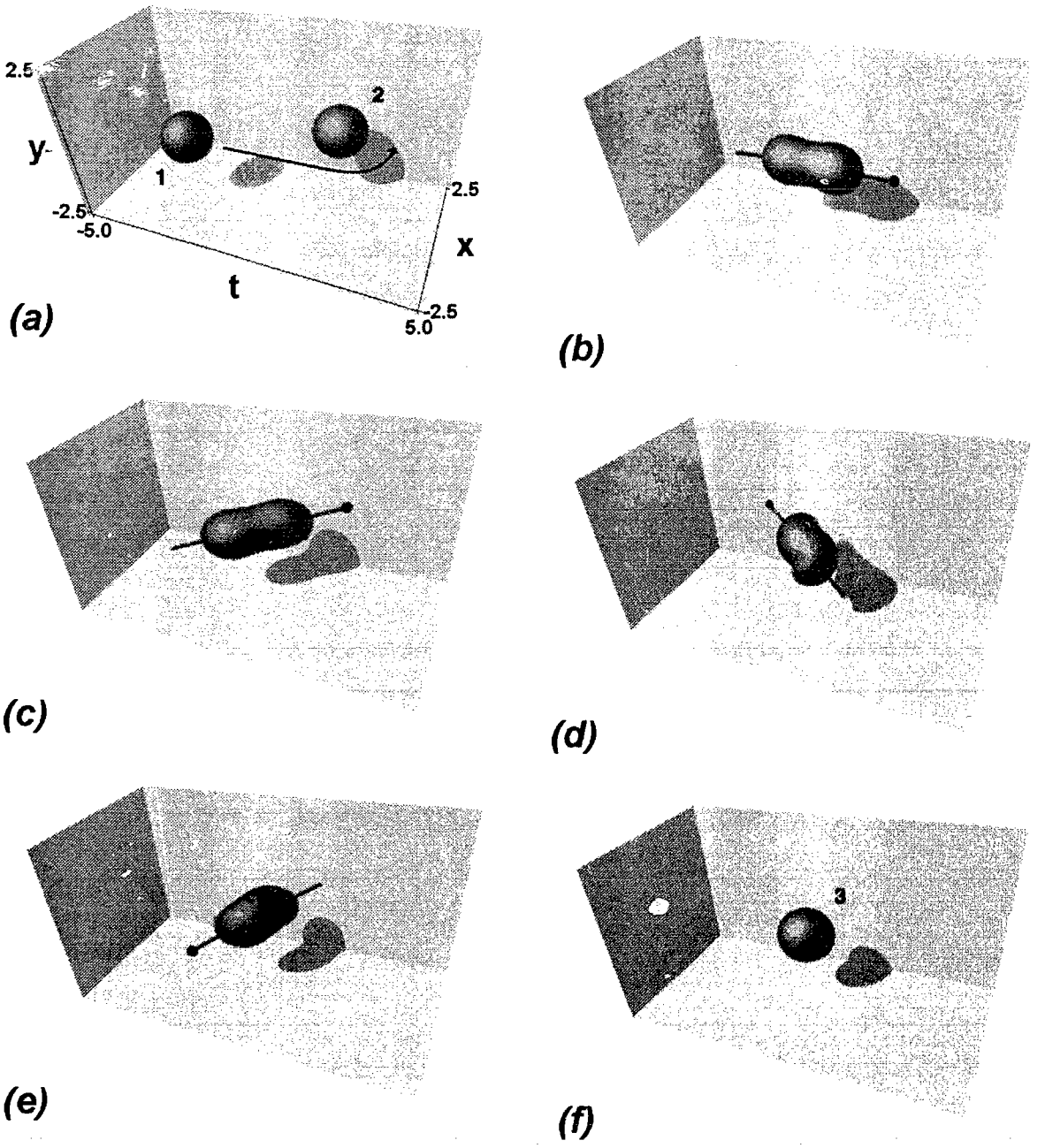

Figure 4.11: Spiralling light bullets and eventual soliton fusion. (a) $z = 0$, (b) $z = 2.75$, (c) $z = 3.10$, (d) $z = 3.70$, (e) $z = 4.15$ and (f) $z = 5.50$. (The "skewer" is added as a visual aid to indicate the degree of rotation.)

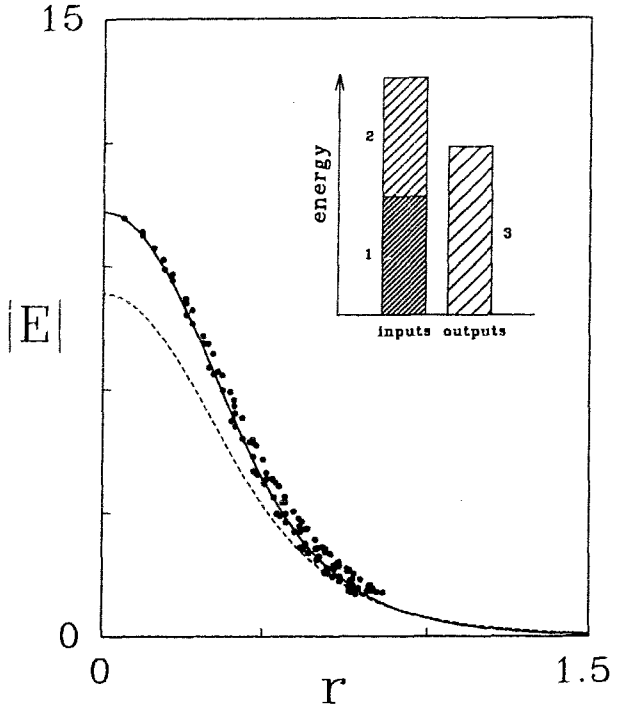

Figure 4.12: Least-squares fit of the final soliton profile. Dashed curve: original $\beta = 4.0$ input states. Solid curve: $\beta = 5.45$. Inset: schematic energy transitions.

4.4 Parasitic solitons: phase controlled interactions

Consider modified initial pulses of the form

$$U(r) \rightarrow U(r)\ \exp(i\phi)$$

where ϕ is a real phase factor. Such a transformation is still a solution to the nonlinear ODE which governs the shape of the initial profile, therefore, it is also a solitary wave solution to the GNLSE itself. An immediate question arises: what occurs for light bullets involved in a collision process when ϕ is different for each input pulse? That is, what is the effect of a global phase difference $\phi_{\text{diff}} = \phi_1 - \phi_2$ between the input states? Referring back to the introduction of this thesis, Figure 1.2(b) illustrates that in one dimension, repulsion occurs if overlapping solitons initially have a π phase difference. Spatially, this behaviour can be understood via the simple Snell's law argument presented earlier, in this case the repulsion being due to a reduction in the refractive index that one soliton "sees" based on the presence of the other soliton's π phase-shifted tail.

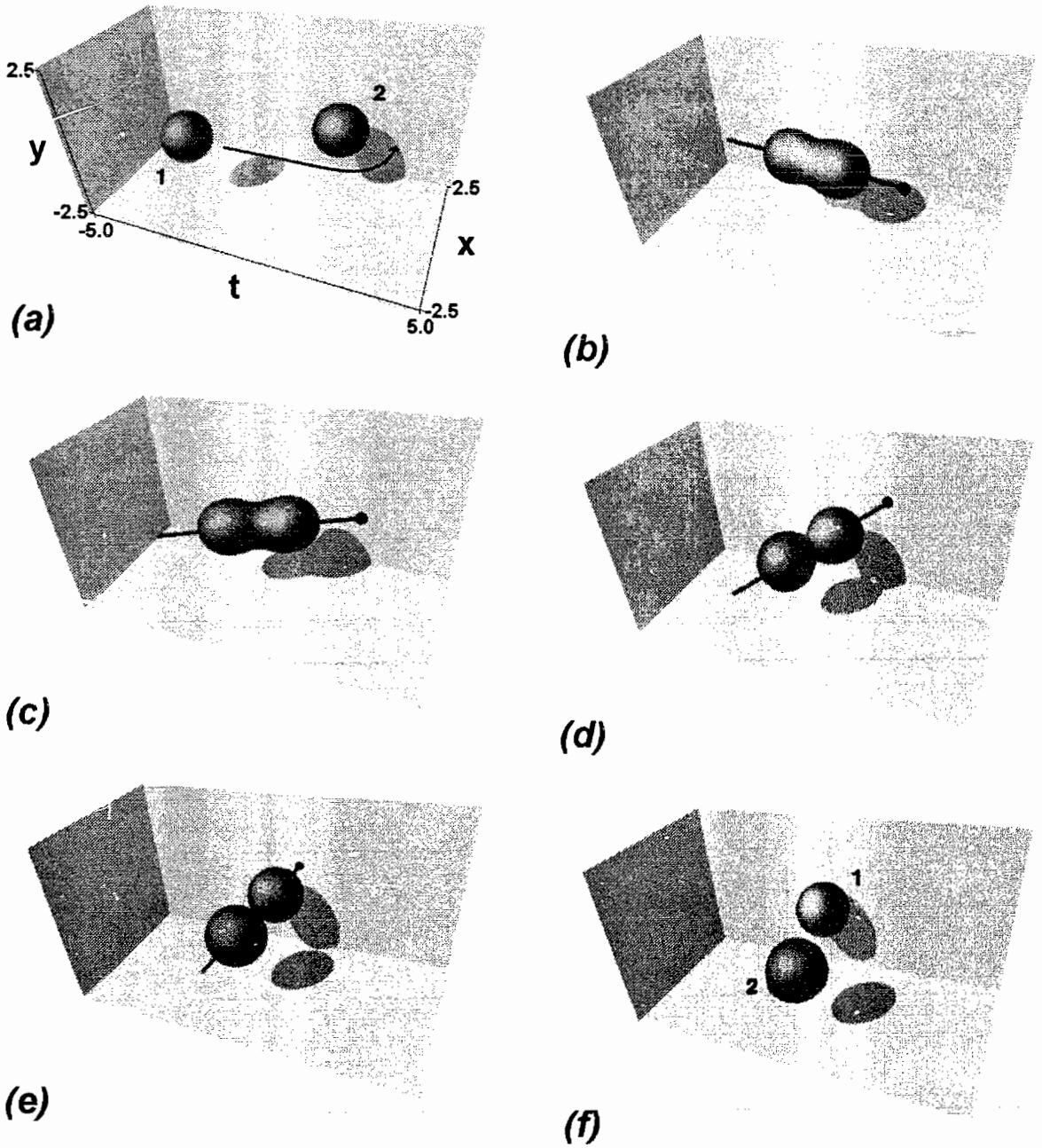

Figure 4.13: Spiralling light bullets without capture. For easy comparison, frames (a) – (e) correspond to the z values of Figure 4.11, while in frame (f), $z = 4.75$.

The analogous repulsion of three-dimensional optical solitons is depicted in Figure 4.14 for the case of two $\beta = 4$ saturable model light bullets initially incident with velocities $v = \pm 1.6$. The reason that we have introduced opposite velocities rather than stationary overlapping states is for comparison with the earlier non-phase-shifted simulations and to illustrate the bullet deformation that occurs at frame (c), the distance of closest approach.

Figure 4.15, the corresponding contour plot for this simulation, illustrates two interesting features. First, the magnitude of the pre- and post-collision velocities are identical. Second, compression at $z = 1.0$ results in a temporary increase in the central $|E|$ field intensity as evidenced by the ring contours in the middle of the figure. A least-squares fit of the final profiles reveals that the propagation constants are unchanged (not shown) - to within the numerical fitting accuracy, this is a completely elastic collision process.

Of course, cylindrical symmetry can be broken and similar π phase-shifted collisions can be performed at non-zero impact parameters. In the language of physics, such collisions are *scattering experiments* and can act as a probe of the force between the incident light bullets. Indeed, this is the approach taken in Chapter 5 where the quantitative nature of the interaction force is determined.

If one moves away from the symmetric situation of either $\phi_{\text{diff}} = 0$ or $\phi_{\text{diff}} = \pi$, quite bizarre results are observed. For example, consider Figure 4.16 which depicts the contour plot for a simulation similar to that above but with the right-most bullet initially leading in phase by $\pi/2$. From this figure, it is obvious that the left-most pulse loses energy, its peak height at $z = 2$ being below the second contour level. Conversely, the peak height of the right-most pulse has increased. This is more easily visualized in Figure 4.17 where we have performed a least-squares fit of the final profiles. Amazingly, the total energy loss to the surrounding background is a mere 1%, a loss that could be due simply to the small uncertainty in the fitting process. As shown by the energy diagram in the figure inset, here we have an example of significant energy transfer from one pulse to another, the light bullets naturally assuming radial profiles commensurate with their new energy content.

The downshifted light bullet has a propagation constant and energy in the vicinity

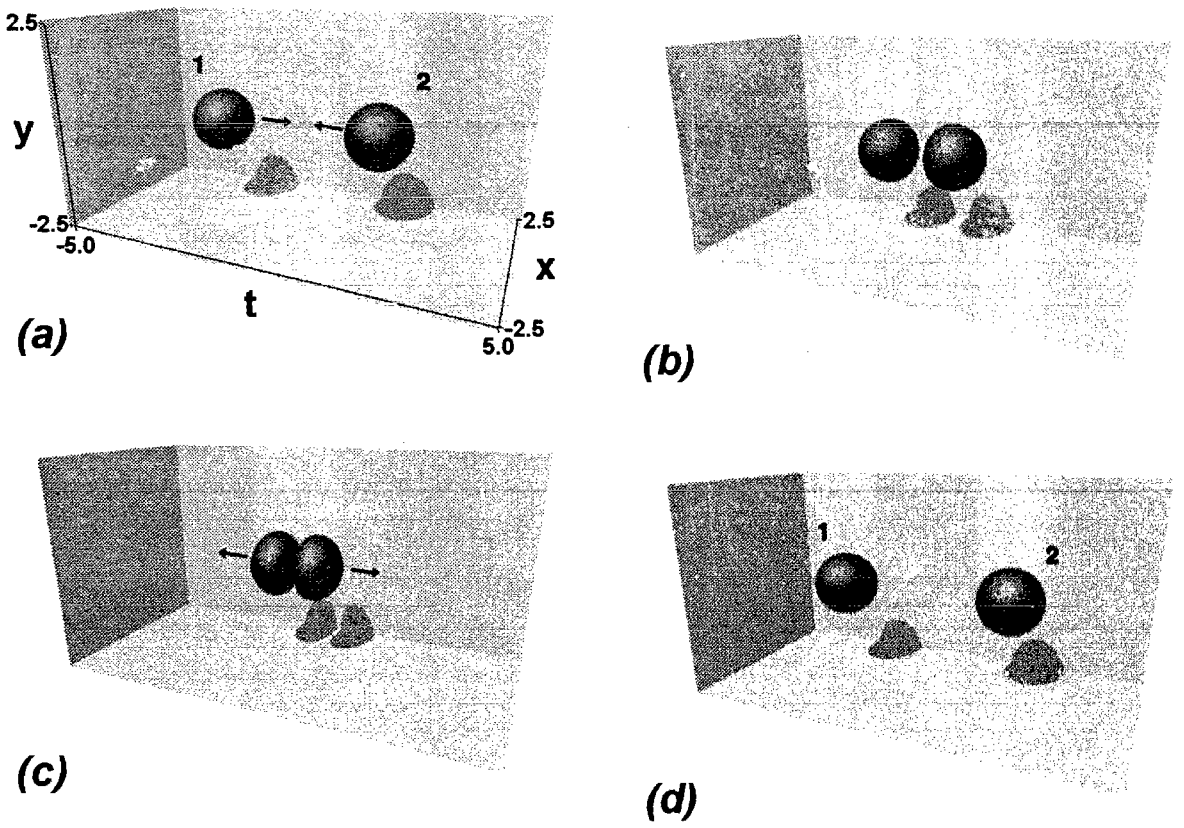

Figure 4.14: Repulsion of π phase-shifted saturable model light bullets. (a) $z = 0$, (b) $z = 0.72$, (c) $z = 1.12$ and (d) $z = 2.25$.

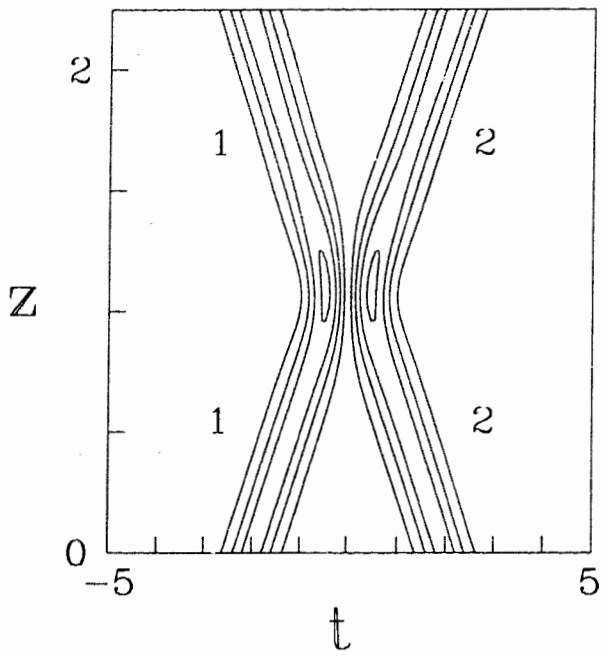

Figure 4.15: Topological soliton track plot for the collision shown in Figure 4.14. Contour levels are $|E| = 2$, 4.5, 7 and 9.5.

of the minima of the saturable model energy curve (Figure 3.4). From our previous experience, we would then expect that any more energy transfer would have left the downshifted pulse with insufficient energy to form an optical soliton and that the resultant pulse would subsequently disperse. An example of a phase-controlled interaction where this occurs is depicted in the contour plot of Figure 4.18 where two $\beta = 4$ light bullets collide with velocities $v = \pm 1.6$, the right-most bullet leading in phase by $\phi_{\text{diff}} = \pi/4$. The propagation constant of the surviving soliton is found to be upshifted to $\beta = 5.5$, the energy remaining in the downshifted state being insufficient to form a saturable model light bullet.

4.5 Switching between bistable soliton states

In the one-dimensional case, a significant amount of theoretical and numerical research has been expended on the problem of switching between bistable soliton states.[7] As discussed in the introduction to this thesis, switching - the conversion of a soliton on one branch of the energy curve to the opposite branch - has as its eventual goal the

[7]See, e.g., the review article by Enns and co-workers [En92b].

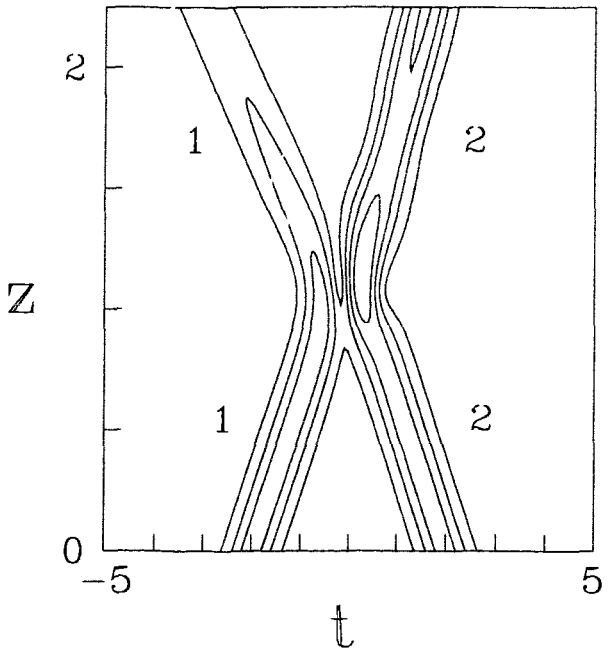

Figure 4.16: Repulsion and parasitic behaviour between light bullets with a $\pi/2$ phase difference. Contours begin at $|E| = 2$ and rise by 2.5 with each successive interior line.

fabrication of all-optical digital logic circuits. Using numerical simulations guided by an approximate variational analysis, Eix and Enns [Ei96] have recently demonstrated that cascadable AND and NOT logic circuits can be designed using evanescently coupled fibers.[8]

It is not the intent of this section to imply that a practical logic circuit can be fashioned using bistable light bullets. Rather, the aim is simply to illustrate an interesting physical phenomenon, namely, that motivated by one-dimensional simulations, the conversion of a low-state bistable optical soliton to a high-state light bullet can readily be achieved for both the SLSS and DSKC models.

Consider first the SLSS model light bullet with propagation parameter $\beta = 0.008$. For convenience, Figure 4.19 reprints the SLSS energy curve[9] with the above light bullet profile indicated by the solid curve in the figure inset. (The arrowed transition will be explained in due course.) In one dimension, addition of a source term to the

[8]A minor clarification is that Eix and Enns utilize the second definition of bistability, pulses with equal duration but different peak intensities.

[9]Although we again choose $\mu = 0.05$ and $I_0 = 5$, it worth restating that the qualitative results that follow are *not* dependent either on this specific choice of parameter or the bistable model. The qualitatively similar results that will be shown for the DSKC model should hopefully lend credence to this assertion.

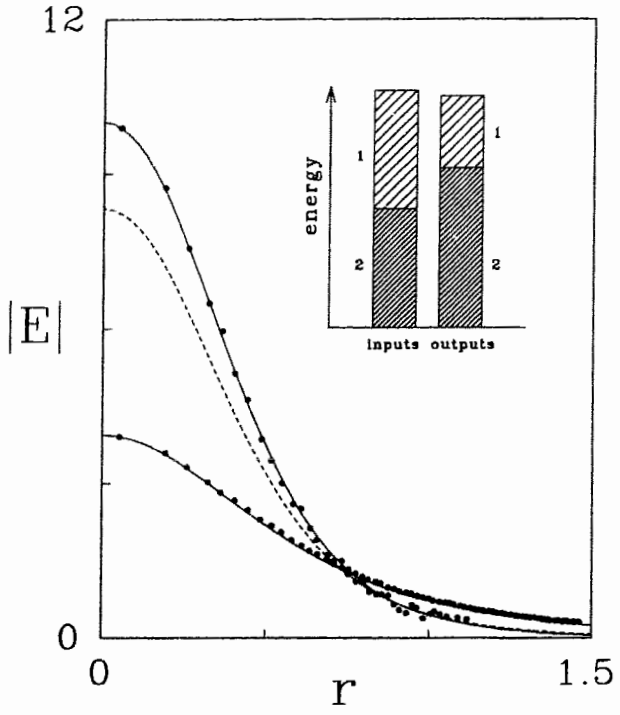

Figure 4.17: Least-squares fits of the final states in Figure 4.16. Upper solid curve: upshifted right-most light bullet with $\beta = 5.3$. Lower solid curve: downshifted left-most light bullet with $\beta = 0.96$. Dashed curve: original $\beta = 4.0$ profile. Inset: schematic energy transitions.

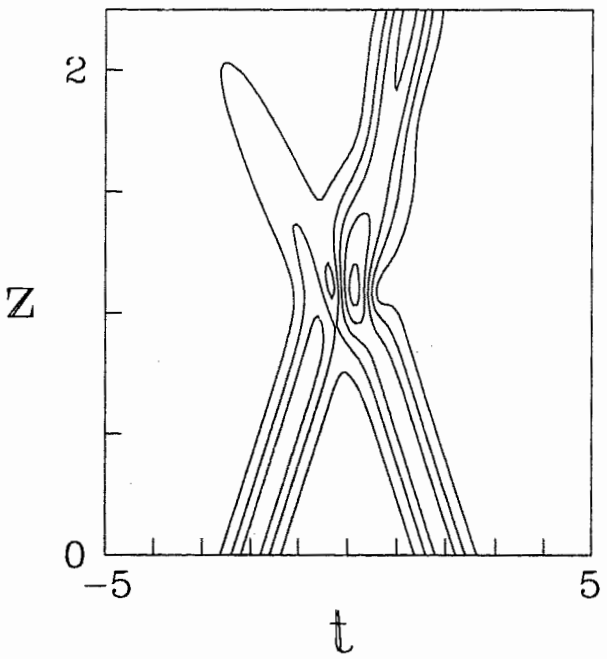

Figure 4.18: Parasitic soliton growth leading to death of the downshifted state. Contours begin at $|E| = 2$ and rise by 2.5 with each successive interior line.

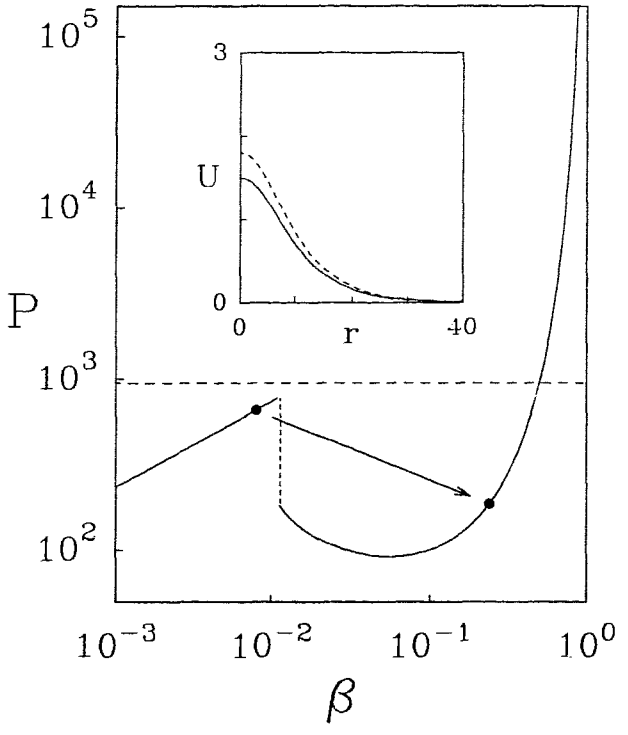

Figure 4.19: SLSS energy curve reprinted. (See accompanying text for an explanation of the arrowed transition and dashed curves.)

GNLSE acting over only a small range of z is a crude but effective means of modelling a fiber amplifier and allows low-state solitons to gain enough excess energy to bridge the crest of the low-state branch. Here, we achieve the same effect by taking profiles of the form

$$U(r) \rightarrow A\,U(r)$$

where A is a real amplification factor. As an illustrative example, consider $A = 1.2$ corresponding to the dashed profile shown in the figure inset and having energy content corresponding to the horizontal dashed line indicated in the main figure. (As this profile is not a solitary wave solution to the GNLSE, it cannot simply be represented as a point on the soliton energy curve.)

To visualize the dynamics of this soliton located in the centre of the computational mesh, Figure 4.20 plots the modulus of the central field value $E_{\text{peak}} \equiv |E(0,0,0)|$ versus propagation distance z. Initially the peak height rises relatively slowly until, at $z = 100$, a sudden upswitching transition to the high-state branch commences. This is followed by a sequence of oscillations relaxing towards an asymptotic soliton state. Dynamically, the relaxation is achieved by a radiative burst of energy released as an

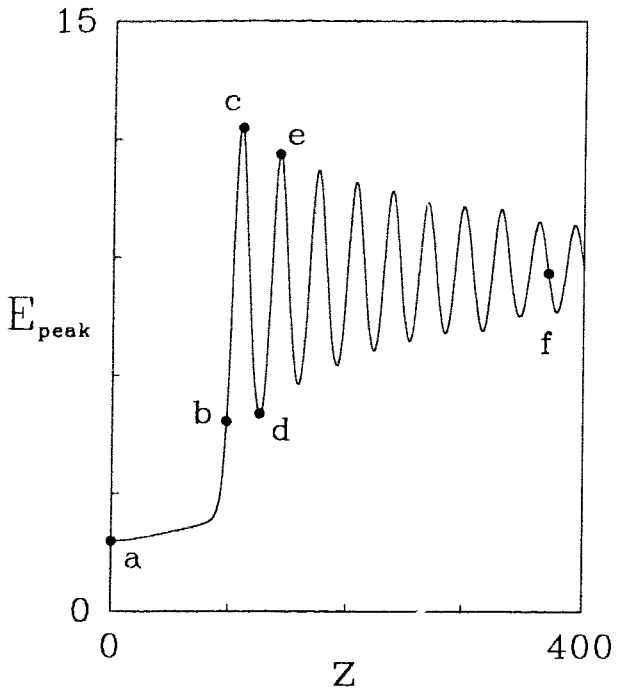

Figure 4.20: Central field value versus z for the $A = 1.2$ amplified soliton of Figure 4.19 (dashed profile in figure inset).

outgoing spherical wave during each oscillation. This can be seen in Figure 4.21 which is comprised of surface plots of $|E(t, x, 0)|$ at six interesting stages of the evolution corresponding to the labels in Figure 4.20.

In order to identify the asymptotic state, rather than fritter away our limited computer cycles waiting for the oscillations to die away, we observe that the oscillation envelope appears to be converging to a peak height in the vicinity of label 'f'. Consequently, we take the pulse profile at this point to be representative of the evolving soliton, a least-squares fit (not shown) revealing that the final state has a propagation constant $\beta = 0.24$.

As indicated by the arrowed transition in Figure 4.19, we have succeeded via a simple amplification scheme in inducing an otherwise stable low-state light bullet to upswitch to the high-state branch. Given the widely disparate radial profiles of these two soliton solutions, this is certainly *not* an intuitive result but again serves to reinforce both the parallels with one-dimensional bistable soliton physics and the role of these objects as attractors in the space of all possible functions.

To emphasize that this behaviour is not due to the specific form of the SLSS model, Figure 4.22 depicts the switching of an amplified $(A = 1.1)$ low-state $\beta = 0.36$ DSKC

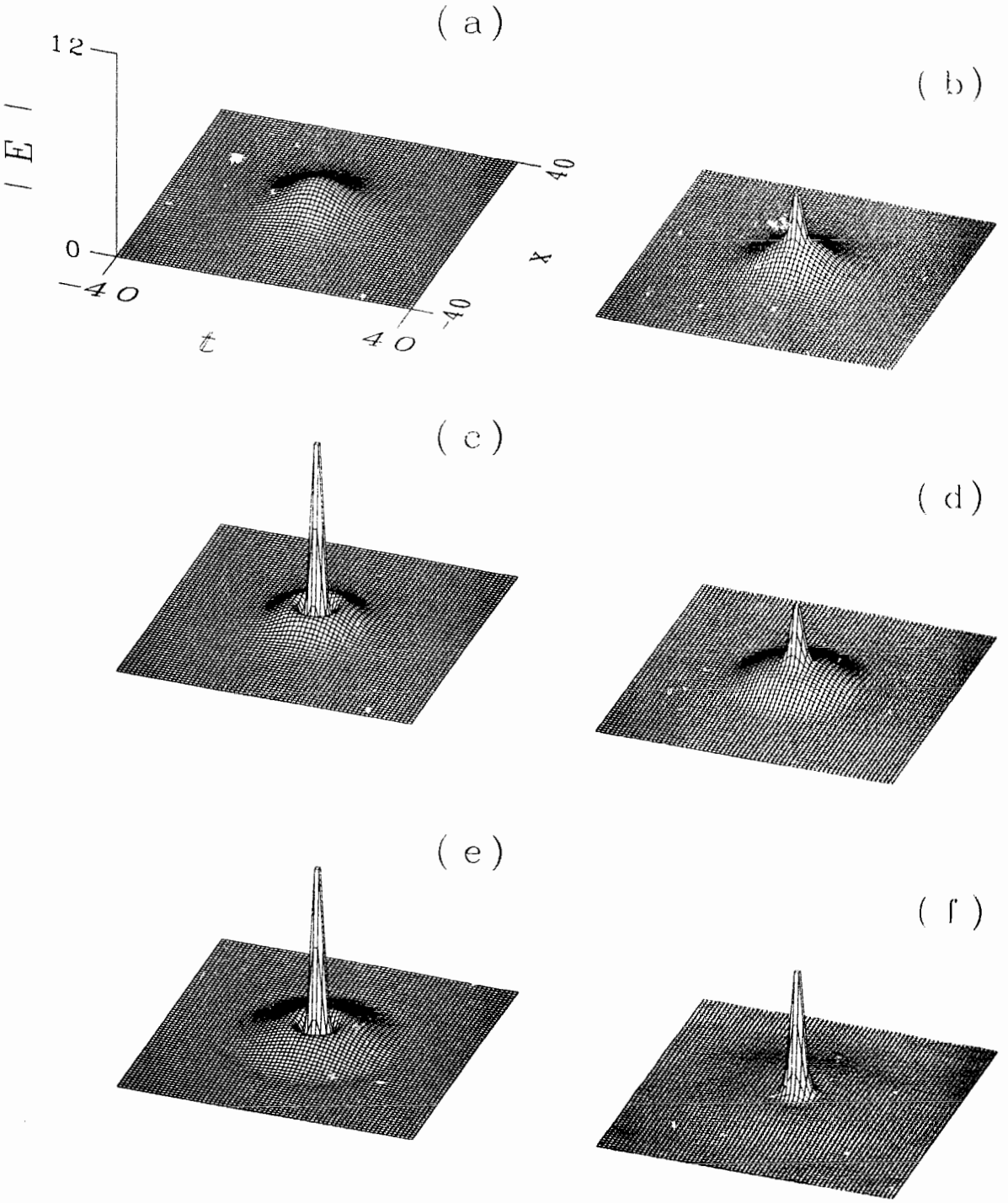

Figure 4.21: Switching of low-state SLSS light bullet via amplification. (a) $z = 0$, (b) $z = 98$, (c) $z = 110$, (d) $z = 126$, (e) $z = 142$ and (f) $z = 370$.

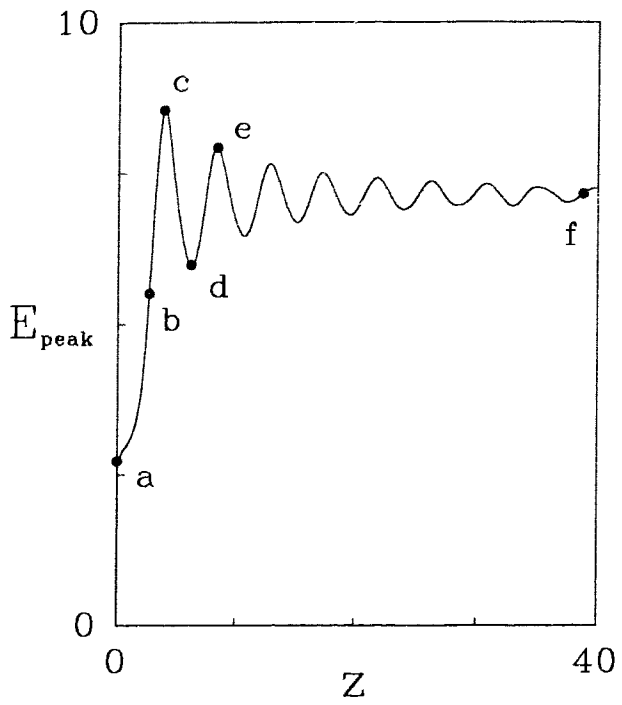

Figure 4.22: Central field value versus z for the $\beta = 0.36$ $A = 1.1$ DSKC amplified soliton.

soliton near the tip of its associated energy curve (Figure 3.18). While the switching transition takes place on a much shorter distance scale and the oscillations are damped more quickly than for the SLSS model, the qualitative features are remarkably similar. The enhanced switching time and damping are likely due to the less drastic contrast between the low and high bistable soliton states; compare, for example, the surface plots of the DSKC model Figure 4.23 with those of the SLSS transition discussed previously (Figure 4.21). The upswitched state as determined by least-squares fitting the profile at frame (f) is found to be $\beta = 1.4$ (not shown). Based on the degree of convergence depicted in Figure 4.22, the profile at distance 'f' must certainly be quite close to the asymptotic soliton state.

Finally, based on this demonstration of induced switching by amplification, we can now rectify an apparent deficiency with the final sections of Chapter 3 pertaining to bistable models. Recall that while an example of a high-state quasi-soliton collision was shown for the SLSS model (DSKC high-state collisions being qualitatively similar), no mention was made of low-state collisions. This was not an oversight, rather, we have delayed discussion of such collisions until the present relevant section. Often, one finds that colliding low-state light bullets inadvertently switch to the high-state

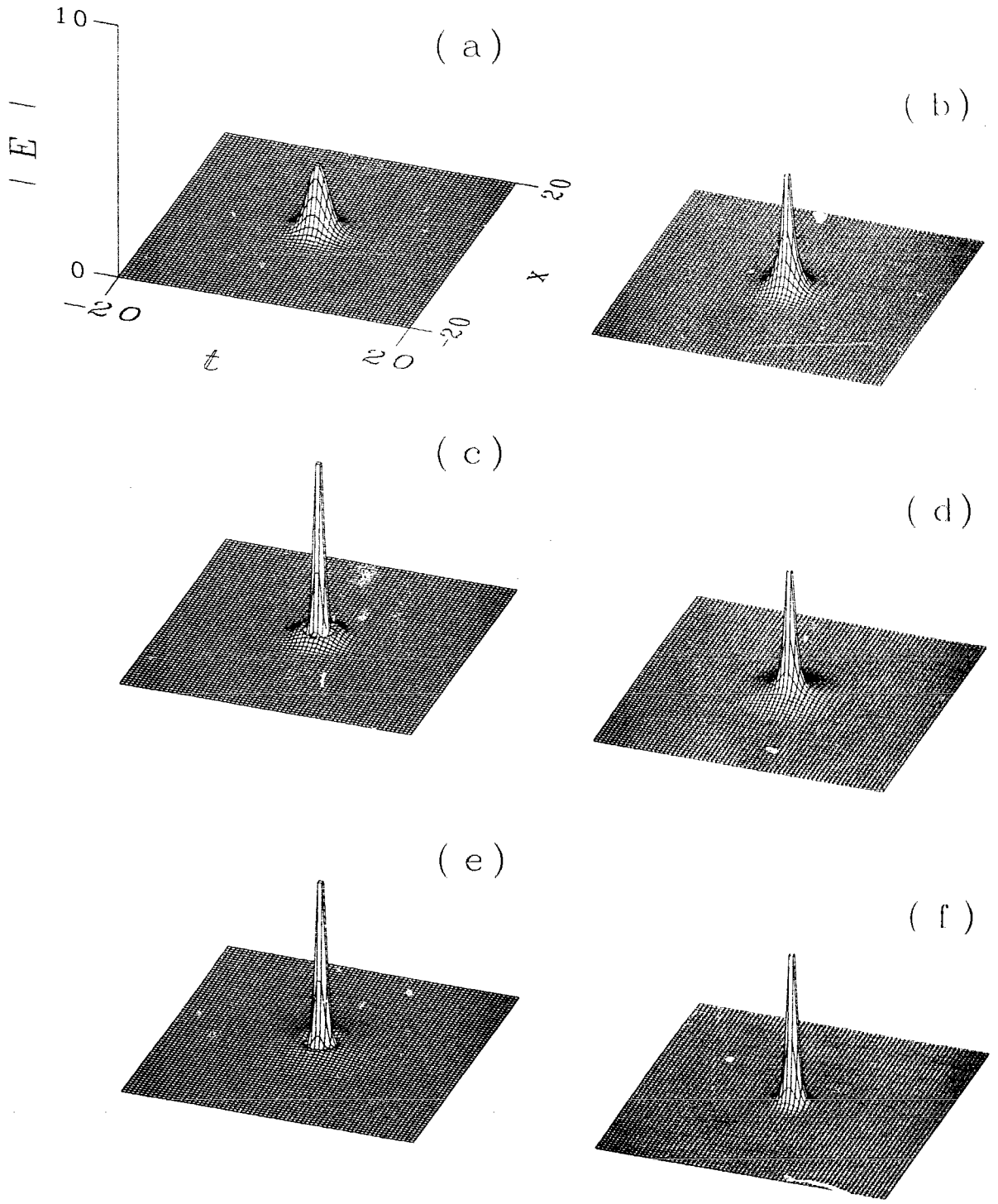

Figure 4.23: Switching of low-state DSKC light bullet via amplification. (a) $z = 0$, (b) $z = 2.6$, (c) $z = 3.8$, (d) $z = 6.2$, (e) $z = 8.4$ and (f) $z = 38.8$.

branch when the pulses overlap. In light of our induced switching simulations, this result is not particularly surprising. One would now expect switching to possibly occur if the peak intensity of the overlapping pulses rises above a certain threshold value.

4.6 Closing comments

It is hoped that this chapter has succeeded in conveying to the reader the inherent richness of the light bullet problem. As this previously unexplored area is a mere five years old, one certainly cannot expect to explore all regions of the vast parameter space. Instead, as stated at the beginning of this chapter, our approach has been to balance the search for novel results with more systematic studies. Consequently, we turn now to a more quantitative analysis - that of ascertaining the precise structure of the interaction force between colliding light bullets.

Chapter 5

The quantitative nature of the interaction

The previous chapter dealing with novel soliton interactions suggests a number of systematic studies. A suitable starting point is to elucidate the general nature of bullet-bullet interactions. We have already seen several examples of light guiding light, that is, the presence of one optical soliton changing the local refractive index such that another soliton changes its trajectory. Of course, this scenario is reciprocated and both solitons undergo a change of course. In the case of zero initial phase difference and non-zero impact parameter, the result is bullet-bullet attraction that can result in orbiting behaviour, eventual soliton fusion, and the formation of a single rotating soliton state. Alternatively, introduction of a π initial phase difference between bullets results in soliton repulsion.

This latter case is extremely exciting because it opens up the possibility of performing scattering experiments whereby a set of collisions at various degrees of glancing incidence can reveal the precise form of the interaction force [Ed95]. Once ascertained, this general force law could then be used to make specific predictions about the outcome of other soliton-soliton collision scenarios.

We will restrict the scattering experiments to light bullets of the saturable model which, as has been noted previously, is characteristic of existing media. In section 5.1,

the scattering experiments are described in detail and the simulation results are presented. In section 5.2, we show that the simulation results can be interpreted within the framework of elastic scattering theory and we proceed to derive a well-known equation for scattering from a central potential. Using this equation, in section 5.3 we determine the analytical form of the interaction potential where it is shown that the scattering data is accurately fitted by a Yukawa potential, a model consistent with assuming that each bullet "sees" only the tail of the other. Further, we demonstrate that the scattering data scales correctly with velocity and the light bullet energy plays the role of an effective mass.

5.1 Scattering experiments

Consider the simplest physically realizable nonlinear refractive index model that supports stable light bullets, namely, the simple saturable model

$$f(|E|^2) = \frac{|E|^2}{1 + a|E|^2} \tag{5.1}$$

Figure 5.1 depicts the saturable model energy curve (originally shown in Figure 3.4) for $a = 0.05$ along with the β values used for the scattering studies. The corresponding radial field profiles are displayed in the figure inset.

A typical scattering simulation is depicted schematically in Figure 5.2 where it is evident that there are a multitude of parameters to choose. For a given collision, the initial symmetric positions of the bullets with respect to the center of the computational mesh are given by the offset parameters $\pm t_0$ and $\pm x_0$. One can also introduce initial constant phase factors ϕ_1 and ϕ_2 by multiplying the individual input profiles by $\exp(i\phi_1)$ and $\exp(i\phi_2)$ for bullets 1 and 2 respectively. Finally, velocities $\pm v$ relative to the group velocity are introduced by taking input profiles of the form $U(r)\exp(\pm ivt)$. With ϕ the same for both pulses (i.e., $\phi_1 - \phi_2 = 0$), the bullets are attractive, bending towards each other as each bullet "sees" an increased refractive index due to the presence of the other bullet's tail.[1] For the scattering experiments

[1] i.e., $U(r)$ at large r.

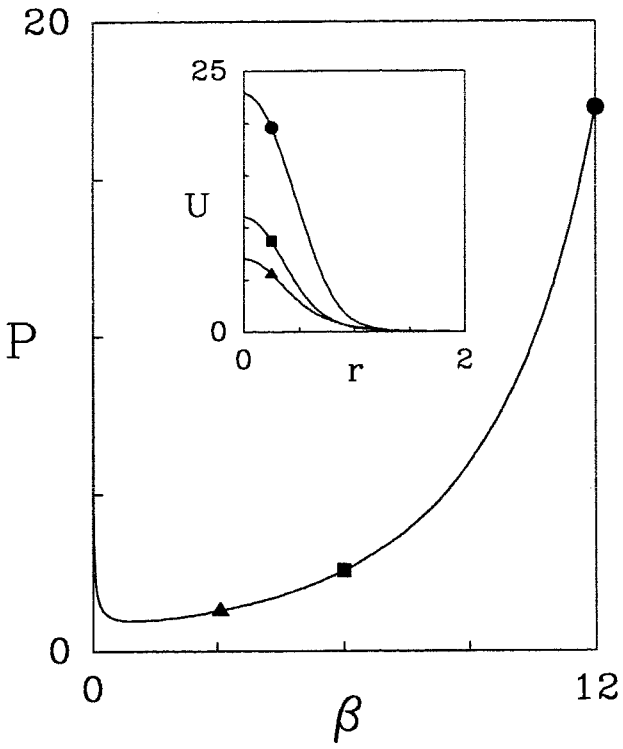

Figure 5.1: Saturable model energy curve reprinted. Inset: radial solitary wave profiles corresponding to the three β values indicated below.

of this chapter, we set $\phi_1 - \phi_2 = \pi$ so that the bullets are repulsive and scatter symmetrically from one another. As one moves away from $\phi_1 - \phi_2 = \pi$, the scattering becomes asymmetric with an energy exchange between solitons, the bullet leading in phase growing at the expense of the other (Chapter 4 and Ref. [Ed93]).

Because the simulations are carried out in a box of finite size, the size being limited by the computer power used, several practical issues had to be dealt with in order to obtain accurate scattering data. Although the solitons tend to look like small billiard balls because of the rapid intensity drop-off with increasing r, nevertheless the tail of each bullet reacts to the tail of the other and one must check that the scattering results are independent of the initial separation t_0. In other words, one must ensure that the light bullets are initially infinitely separated. For example, Figure 5.3 demonstrates how the asymptotic scattering angle θ reaches a plateau as t_0 is increased for two $\beta = 6$ light bullets initially incident with $v = 0.5$ and impact parameter $b = 0.8$.

An additional concern is that if the impact parameter b becomes too large, the interaction across the periodic boundary will become problematic and the scattering results will again be adversely affected. One must also be quite sure that the measured

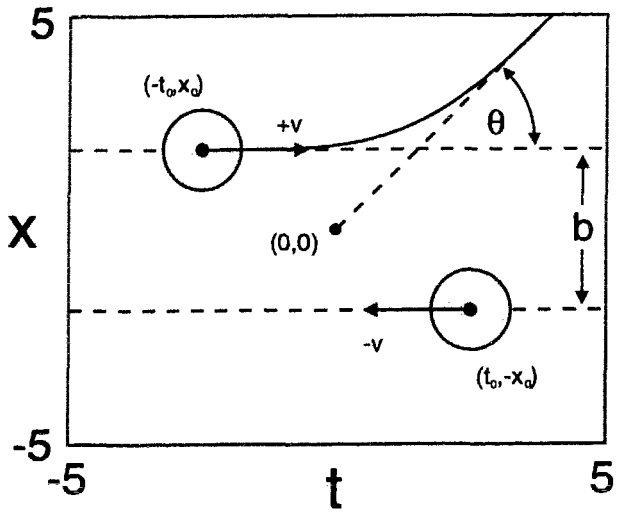

Figure 5.2: Schematic representation of scattering experiments in the $x - t$ plane. The rightmost bullet scatters symmetrically to the leftmost bullet.

angle is in fact the asymptotic scattering angle θ. These and other issues connected to the finite size of the computational mesh have been carefully considered in presenting the final scattering data.

A typical numerical scattering experiment is rendered in Figure 5.4. Two $\beta = 6$ light bullets are initially positioned at $t_0 = \pm 2$ and $x_0 = \pm 0.4$ (corresponding to an impact parameter $b = 0.8$) with $|v| = 0.5$. As the simulation proceeds, the bullets approach and meet at $z = 3.0$, compressing slightly before scattering at an angle slightly greater than $\theta = \pi/2$. The particle or billiard ball-like nature of the light bullets is quite evident, although the light bullets are clearly not hard spheres since they compress slightly along their contact edge at $z = 3.0$. However, the force appears to be short-ranged since, following the collision, the bullets rapidly regain their spherical shape and settle onto their final outgoing trajectories.

We have performed a complete set of scattering studies for various impact parameters and speeds $v = 0.1$, 0.25, and 0.5, culminating in curves plotting asymptotic scattering angle θ versus b for $\beta = 3$, 6 and 12 (Figures 5.5 – 5.7). These curves have the expected behaviour that:

- $\theta \to \pi$ as $b \to 0$ with the bullets colliding head-on and reversing direction.
- $\theta \to 0$ for increasing b, the solitons passing by each other with decreasing interaction.

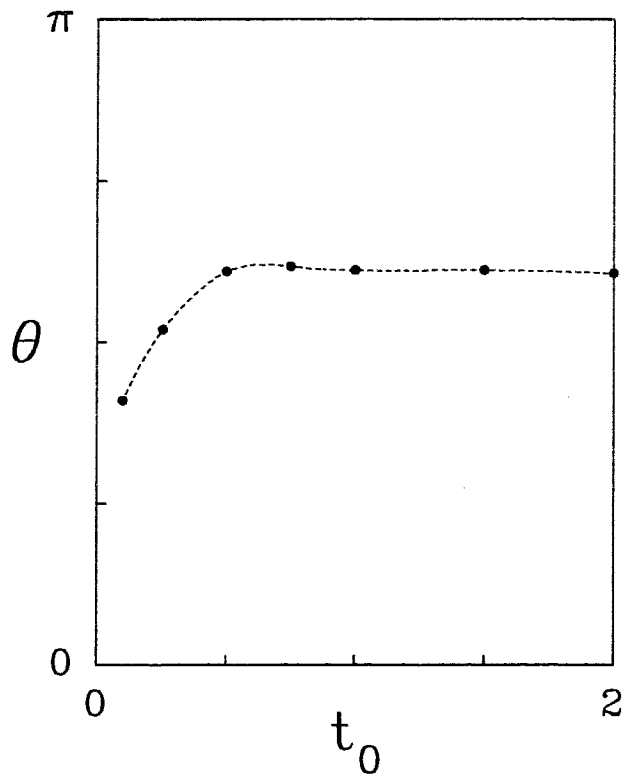

Figure 5.3: Typical dependence of the asymptotic scattering angle θ on initial bullet separation.

- For a given impact parameter b, the scattering angle is less for collisions at higher velocity as the bullets spend less time interacting with each other.

Before proceeding, we should briefly estimate the error in the $\theta(b)$ measurements. The θ values are extracted from 2-dimensional 140·140 pixel animations corresponding to a slice through the three-dimensional mesh in the x-t plane. One calculates θ by forming a triangle whose hypotenuse is tangent to the asymptotic trajectory. Assuming a single pixel error in locating the end-point of the hypotenuse, one can determine $\Delta\theta/\theta \sim 3\%$ as representative of the error associated with this procedure. The errors in θ due to the step size (Δz), initial t_0 separation, and across-boundary effects are believed to be negligible. The numerical (i.e., algorithmic) error due to the coarseness of the grid could be ascertained by performing simulations on much finer meshes. Unfortunately, this is beyond our current computational power. However, in light of the results that follow, this error is either small or benevolently biased.

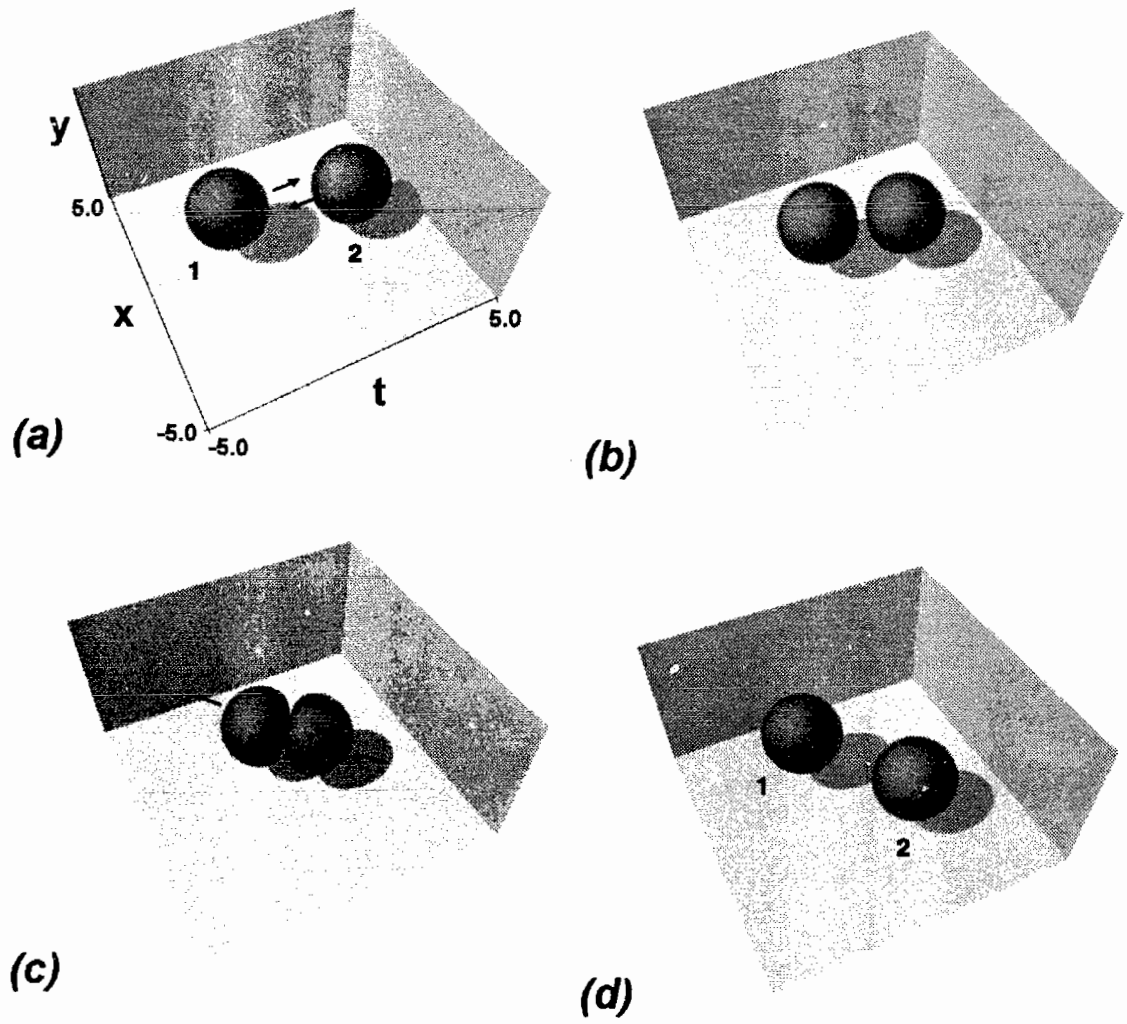

Figure 5.4: Typical scattering simulation for two repulsive light bullets. (a) $z = 0$, (b) $z = 1.47$, (c) $z = 3.22$ and (d) $z = 5.81$. Vertical scale: $-2.5 \leq y \leq 2.5$.

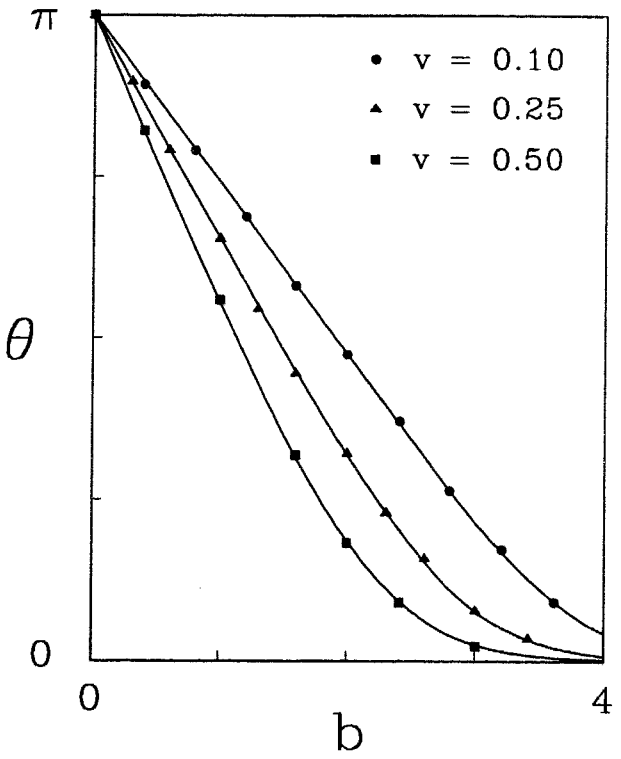

Figure 5.5: Asymptotic scattering angle versus impact parameter curves for scattering of two $\beta = 3$ light bullets at three collision velocities. (The solid lines are theoretical fits that will be discussed in section 5.3).

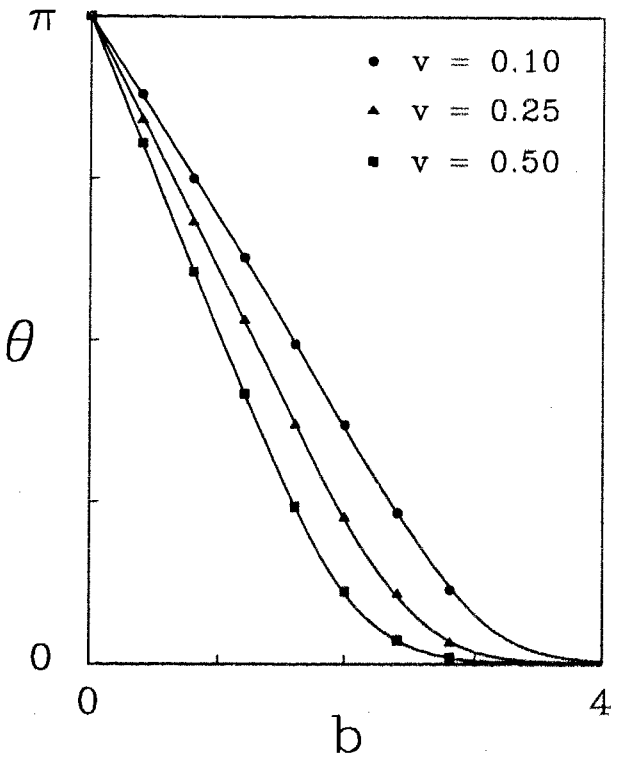

Figure 5.6: θ versus b curves for scattering of two $\beta = 6$ light bullets at three collision velocities.

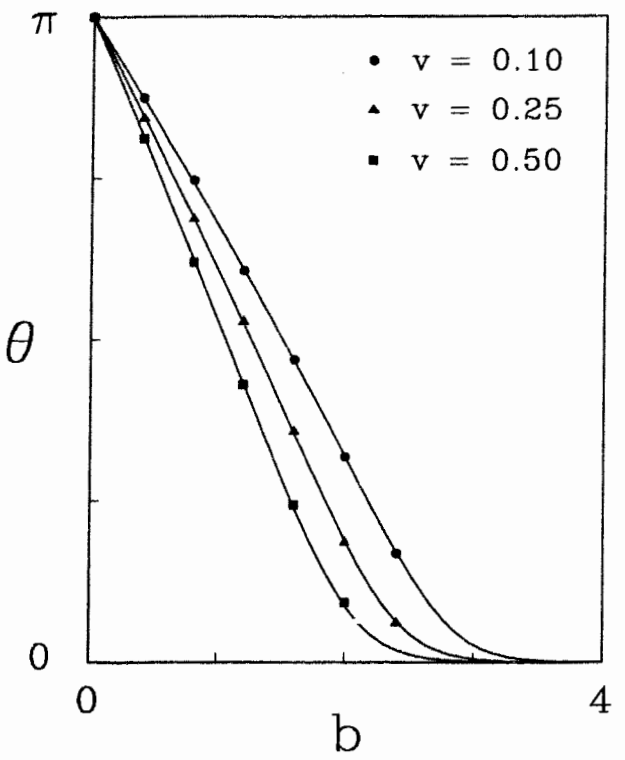

Figure 5.7: θ versus b curves for scattering of two $\beta = 12$ light bullets at three collision velocities.

5.2 Elementary scattering theory

5.2.1 Hard sphere scattering

How then does one proceed to determine the nature of the interaction from the raw scattering data of Figures 5.5–5.7? The simplest scenario is that of a hard sphere collision where two billiard ball-like light bullets with radii A and effective mass m collide with speeds $\pm v$ at impact parameter b. In this case, it is easy to show that the asymptotic scattering angle is given by

$$\theta = \pi - 2\sin^{-1}\left(\frac{b}{2A}\right) \tag{5.2}$$

For $b/2A \ll 1$, expansion of the sine function yields

$$\theta = -\left(\frac{1}{A}\right)b + \pi \tag{5.3}$$

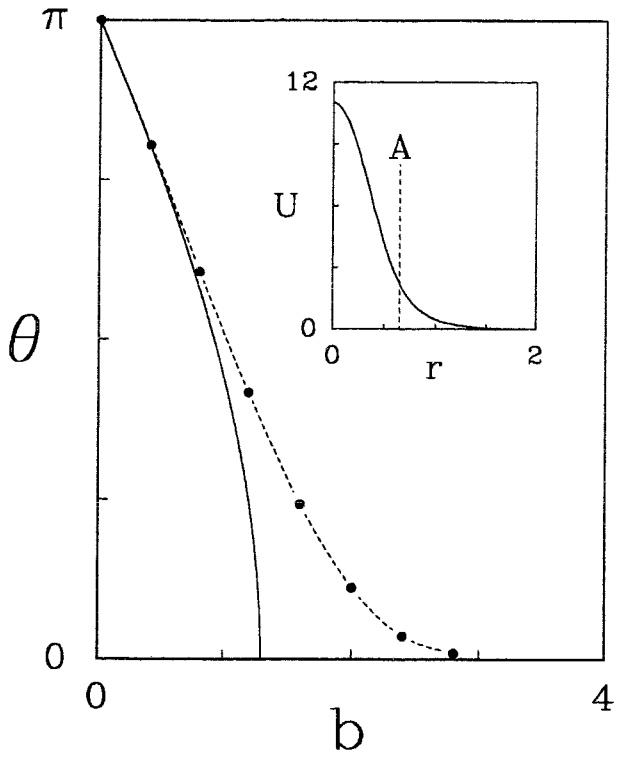

Figure 5.8: Least-squares fit of the hard sphere model to the $\beta = 6$, $v = 0.1$ scattering data of Figure 5.6. Inset: initial $\beta = 6$ profile with effective core-size 'A' indicated by vertical dashed line.

so that, for a hard sphere interaction, the scattering curve for small impact parameters will be linear with a slope inversely proportional to the effective bullet radius. However, at $b = 2A$, Eq. (5.2) (and common sense) dictates that the bullets will pass at grazing incidence and fail to scatter. Figure 5.8 shows a least-squares fit of the hard sphere model to the $\beta = 6$, $v = 0.1$ scattering data of Figure 5.6 revealing an effective core size of $A = 0.65$ as indicated in the figure inset. Obviously such a simplistic model with finite range cannot account for the asymptotically decreasing tails of our scattering data. Consequently, we are led to consider the elastic scattering of two particles interacting via a separation dependent potential.

5.2.2 Elastic scattering

During an elastic scattering event, the particles' kinetic energies are conserved. In other words, the collision process should be immune to:

- "Frictional losses" in which the bullets radiate energy.

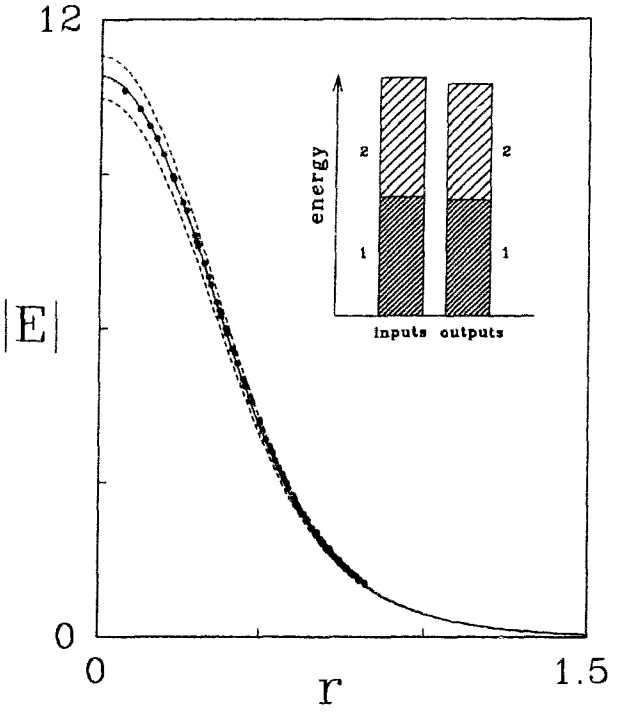

Figure 5.9: Least-squares $\beta = 5.9$ fit of the initially left-most $\beta = 6$ light bullet in frame (d) of Figure 5.4. Upper and lower dashed curves are $\pm 5\%$ of the fit value. Inset: schematic energy transitions.

- Changes in the internal energy of the light bullets including transfer of energy to vibrational (pulsating) modes.

If these conditions hold, then, as shall be demonstrated, the asymptotic scattering angle θ is determined by a separation-dependent interaction potential, the initial light bullet kinetic energies and the impact parameter. The methodology is then to compare the results of various reasonable interaction potentials against the scattering data obtained by numerical experiment.

That the collision process is almost completely elastic is confirmed by comparing the initial and final bullet profiles and energies. As an example, Figure 5.9 depicts a least squares fit to the left-most light bullet in Figure 5.4(d). The filled circles are a selection of numerical points taken from the computational mesh while the solid line is the best fit profile with $\beta = 5.9$. The input profile of $\beta = 6.0$ (not shown) is so close to the experimental points that it is virtually indistinguishable from the solid curve. A very small amount of radiation (approximately 2%) has been shed which, because of its low intensity and the greyscale cutoff, is not apparent in Figure 5.4. In terms of the $P(\beta)$ curve of Figure 5.1, the final state is still inside the square data

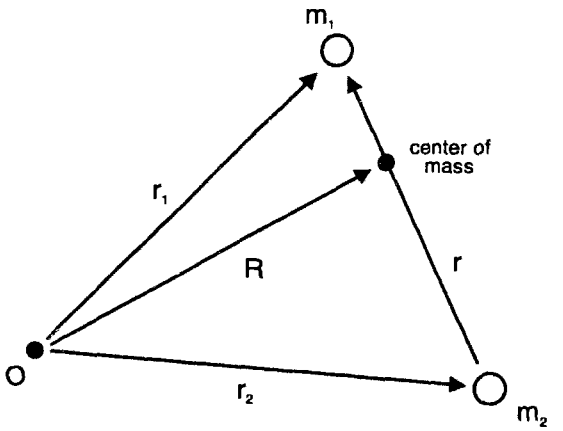

Figure 5.10: Schematic diagram of two point particles moving with respect to each other and a fixed origin.

point shown. That little or no vibrational (pulsating) modes have been excited is readily determined by observing a three-dimensional animation of the collision. Thus we conclude that the repulsive light bullets are extremely stable and undergo nearly elastic collisions with one another.

The scattering of two point particles under the influence of a central force is a familiar classical mechanics problem. We provide here a condensed derivation taken from J. B. Marion's "Classical Dynamics of Particles and Systems" [Ma70].

Figure 5.10 is a schematic representation of two particles moving with respect to each other and an arbitrary fixed origin. Restricting ourselves to systems where the potential energy V is only a function of the separation between particles $r = |\vec{r_1} - \vec{r_2}|$, the Lagrangian is

$$L = \frac{1}{2}m_1|\dot{\vec{r_1}}|^2 + \frac{1}{2}m_2|\dot{\vec{r_2}}|^2 - V(r) \tag{5.4}$$

We choose to work in the centre of mass frame where $\vec{R} \equiv 0$ such that

$$m_1\vec{r_1} + m_2\vec{r_2} = 0 \tag{5.5}$$

Expressing $\vec{r_1}$ and $\vec{r_2}$ in terms of $\vec{r}$ by virtue of Eq. (5.5), the Lagrangian can be written as

$$L = \frac{1}{2}\mu|\dot{\vec{r}}|^2 - V(r) \tag{5.6}$$

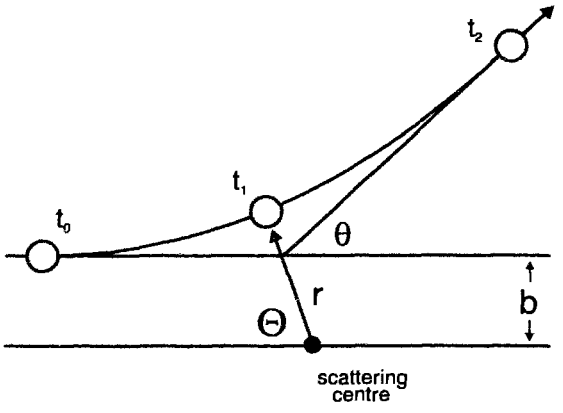

Figure 5.11: Scattering from a central potential.

where the reduced mass μ is defined to be

$$\mu \equiv \frac{m_1 m_2}{m_1 + m_2} \tag{5.7}$$

or, as in our case when the two bullets have equal "mass" m, $\mu = m/2$. Thus, as shown in Figure 5.11, the motion of two particles interacting via a separation-dependent potential can be thought of as the scattering of a single reduced mass from a fixed central potential $V(r)$.

As the potential $V(r)$ possesses spherical (rotational) symmetry, angular momentum of the system is conserved implying that the radius vector $\vec{r}$ is confined to a 2-dimensional plane. It is thus convenient to work in plane polar coordinates where the Lagrangian becomes

$$L = \frac{1}{2}\mu(\dot{r}^2 + r^2\dot{\theta}^2) - V(r) \tag{5.8}$$

Since L possesses no explicit θ dependence, the generalized momenta conjugate to θ is conserved, viz.

$$\dot{p_\theta} = \frac{\partial L}{\partial \theta} = 0 = \frac{\mathrm{d}}{\mathrm{d}t}\frac{\partial L}{\partial \dot{\theta}} \tag{5.9}$$

We can thus immediately integrate Eq. (5.9) to obtain

$$p_\theta = \frac{\partial L}{\partial \dot{\theta}} = \mu r^2 \dot{\theta} \equiv \ell \tag{5.10}$$

where ℓ is a constant of the motion. With no dissipation, the total energy is also conserved and

$$\begin{aligned} E &= \frac{1}{2}\mu(\dot{r}^2 + r^2\dot{\theta}^2) + V(r) \\ &= \frac{1}{2}\mu\dot{r}^2 + \frac{1}{2}\frac{\ell}{\mu r^2} + V(r) \end{aligned} \tag{5.11}$$

which can be solved for $\dot{r}$ to yield

$$\dot{r} = \sqrt{\frac{2}{\mu}\left(E - V(r) - \frac{\ell^2}{2\mu r^2}\right)} \tag{5.12}$$

For a repulsive potential, the vanishing of $\dot{r}$ implies a turning point in the motion, the distance of closest approach (label 't_1' in Figure 5.11), $r_{\min}$, being given by the real root of the function under the square root sign in Eq. (5.12). The differential change in angle

$$\mathrm{d}\theta = \frac{\mathrm{d}\theta}{\mathrm{d}t}\frac{\mathrm{d}t}{\mathrm{d}r}\mathrm{d}r = \frac{\dot{\theta}}{\dot{r}}\mathrm{d}r \tag{5.13}$$

Substitution of $\dot{\theta} = \ell/\mu r^2$ and Eq. (5.12) into Eq. (5.13), and integrating over a range of radii yields

$$(\Delta\theta) = \int_{r_{\min}}^{r_{\max}} \frac{\ell}{r^2\sqrt{2\mu\left(E - V(r) - \frac{\ell^2}{2\mu r^2}\right)}}\,\mathrm{d}r \tag{5.14}$$

for the change in angle for a particle travelling between the two radii indicated. For the case of a repulsive potential, $r_{\max} = \infty$. At $r = \infty$, the potential energy stored in the system is zero and all of the energy is kinetic, viz.

$$E = T_0 \equiv \frac{1}{2}\mu {v_0}^2 \tag{5.15}$$

where v_0 is the reduced particle's initial velocity. Finally, the angular momentum can be specified in terms of the initial kinetic energy and impact parameter b as

$$\ell = \mu v b = b\sqrt{2\mu T_0} \tag{5.16}$$

so that Eq. (5.14) becomes

$$\Theta = \int_{r_{\min}}^{\infty} \frac{(b/r^2)}{\sqrt{1-(b/r)^2 - V(r)/T_0}}\, \mathrm{d}r \tag{5.17}$$

From Figure 5.11

$$\theta = \pi - 2\Theta \tag{5.18}$$

so that the asymptotic scattering angle

$$\theta = \pi - 2\int_{r_{\min}}^{\infty} \frac{(b/r^2)}{\sqrt{1-(b/r)^2 - V(r)/T_0}}\, \mathrm{d}r \tag{5.19}$$

We now have an equation that determines the asymptotic scattering angle based solely on the initial impact parameter, a general central potential, and the initial kinetic energy of the system. While Eq. (5.19) can be solved analytically for several low-order polynomial models in terms of elliptic functions, e.g., the Coulomb potential with $n = 1$, it must generally be solved numerically.[2]

5.3 The nature of the interaction

As a first naive attempt, let us consider polynomial models of the form

$$\frac{V(r)}{T_0} = Cr^{-n} \tag{5.20}$$

where C is a real constant and consider the $\beta = 6$ scattering data of Figure 5.6. Figure 5.12 depicts least-squares fits of the linear portion of the $\beta = 6$, $v = 0.5$ scattering data to various polynomial models for integer n. From this figure it is clear that the potential is relatively short range with the best fit occurring for $n \simeq 7$.

[2]The value of $r_{\min}$ is easily determined by standard root-finding techniques, e.g., Newton's method. However, care must be taken to obtain an accurate numerical determination of θ as the integrand diverges at the lower bound. The standard method [Pr86] is to break the integral into two pieces at a point where r is large enough that the integrand is already beginning to asymptotically approach zero. Both integrals are then handled by a change of variable, the lower change eliminating the integrable singularity while the upper change maps the infinite interval into a finite range.

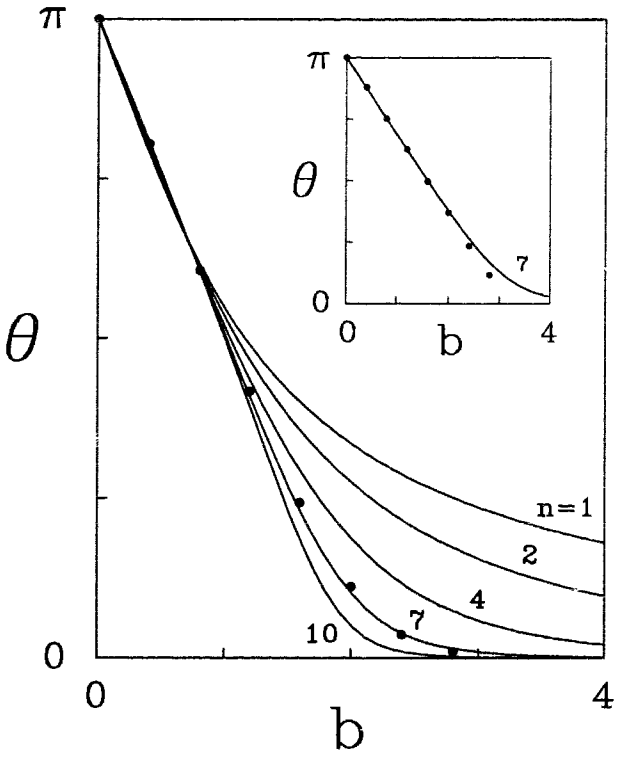

Figure 5.12: Least squares fit to $\beta = 6$, $v = 0.5$ scattering data for various polynomial models $V(r) \propto r^{-n}$. Inset: Optimum least-squares fit to $\beta = 6$, $v = 0.1$ scattering data for the $n = 7$ polynomial model.

However, as the inset shows, one cannot then accurately fit the $v = 0.1$ scattering data with the $n = 7$ polynomial model, the best fit occuring for $n = 10$ (not shown). This scenario holds for all of the scattering data; one finds that any two sets of curves at a given β value cannot be fitted by the same (even non-integer) n value. As it is intellectually unappealing to have the force law depend on the velocities of the input pulses, we reject the class of polynomial models.

Having ruled out polynomial models, what should we take as an approximation to the correct interaction potential? Let us assume that the interaction is dominated by each bullet reacting to the rapidly decreasing tail of the other. For the Kerr case in one dimension, an asymptotic expansion of the solitary wave for large r reveals that

$$U(r) \propto \exp(-\gamma r) \tag{5.21}$$

with decay constant $\gamma = \sqrt{2\beta}$. Gordon theoretically found that coalescence between overlapping in-phase one-dimensional solitons is exponential with this same decay constant [Go83]. Recall the ordinary differential equation that determines light bullet

radial profiles

$$\frac{\mathrm{d}^2U}{\mathrm{d}r^2} + \frac{2}{r}\frac{\mathrm{d}U}{\mathrm{d}r} + 2\left[f(U^2) - \beta\right]U = 0 \tag{5.22}$$

and assume that in the tail region $f(U^2) \ll \beta$. That is, for the saturable model, the intensity

$$I = U^2 \ll \frac{\beta}{1 - a\beta} \tag{5.23}$$

For $a = 0.05$, we require that $U \ll 1.9$, 2.9 and 5.5 for $\beta = 3$, 6, and 12, respectively. Neglecting the $f(U^2)$ term in Eq. (5.22) results in a modified Bessel equation,

$$\frac{\mathrm{d}^2U}{\mathrm{d}r^2} + \frac{2}{r}\frac{\mathrm{d}U}{\mathrm{d}r} - 2\beta U = 0 \tag{5.24}$$

the relevant physical solution[3] of which is

$$U(r) \propto \frac{\exp(-\gamma r)}{r} \tag{5.25}$$

For $\beta = 3$, 6, and 12, $\gamma = 2.45$, 3.46 and 4.90 respectively.

Let us assume that the interaction is governed by the shape of the bullet tail and as a trial potential function in Eq. (5.19) we choose

$$\frac{V(r)}{T_0} = C\frac{\exp(-\alpha r)}{r} \tag{5.26}$$

(with C and α real positive parameters) which is of the form of a Yukawa potential. The validity of this assumption can only be answered by a comparison between the theoretical predictions of the interaction model and the numerical scattering data. Thus, we will determine α and C by a least-squares fit of the model to the scattering data. If the tails of the bullets do indeed dominate the interaction, we expect to find that

$$\alpha \simeq \gamma \equiv \sqrt{2\beta}$$

In addition, if this hypothesis is correct, as the kinetic energy $T_0 \sim v^2$, one would expect that $\sqrt{C}$ scales as $1/v$.

[3] i.e., nonsingular at the origin.

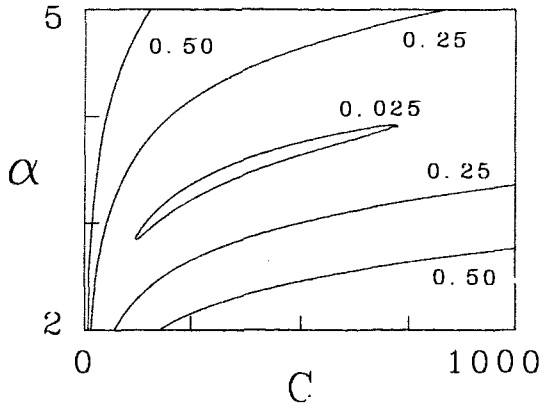

Figure 5.13: Contours of constant merit function L in the $\alpha - C$ plane for $\beta = 6$, $v = 0.5$ scattering data and the Yukawa interaction potential $V(r)/T_0 = C\exp(-\alpha r)/r$.

In order to quantitatively compare the experimental results with the theoretical predictions, we define a least squares merit function

$$L(\alpha, C) \equiv \sqrt{\frac{1}{n}\sum_{i=1}^{n}\left[\theta_{\text{theory}}(\alpha, C; b_i) - \theta_{\text{num}}(b_i)\right]^2} \tag{5.27}$$

which is positive definite and disappears for an exact fit between theory and numerical experiment. (It may be helpful to remember that L corresponds to the mean vertical deviation between points on the numerical and theoretical scattering curves.) We then search for α and C that minimize L for a given set of $\theta(b)$ scattering data.

Figure 5.13 shows contours of constant L in the α-C plane for the $\beta = 6$, $v = 0.5$ scattering data. One observes a long narrow valley for $L = 0.025$ and, as the minimum lies within this region,[4] α is restricted to be between 3 and 4. Traversing this valley from one end to the other, we obtain the $v = 0.5$ curve shown in Figure 5.14, the minimum of which occurs for $\alpha = 3.32$. Repeating this process for the $v = 0.1$ and $v = 0.25$ scattering data results in the other curves shown in Figure 5.14, each of which has a two-dimensional merit function qualitatively similar to Figure 5.13. The minima are at $\alpha = 3.30$ and 3.55 for $v = 0.1$ and 0.25 respectively. As for the polynomial model, we expect the decay constant α to be velocity independent and therefore take the optimal α to be the mean value $\overline{\alpha} = 3.40$ which differs by only

[4]Note that $L = 0.025$ indicates an extremely small mean deviation between theory and numerical experiment.

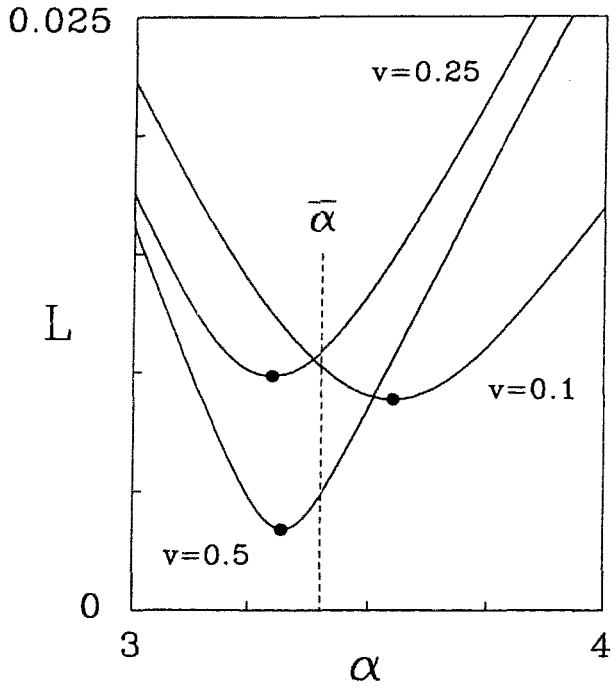

Figure 5.14: $v = 0.5$ curve is a plot of L versus α along the valley floor of Figure 5.13. $v = 0.25$ and $v = 0.5$ curves are similarly obtained from their respective scattering data. $\overline{\alpha}$ (vertical dashed line) calculated as the mean value of the three minima shown.

2% from the "theoretical" value $\sqrt{2\beta} = 3.46$. That these L minima do not occur for exactly the same α value is likely due to a combination of numerical error, the error in extracting $\theta(b)$ from the two-dimensional animations, and slightly inelastic behaviour.

This procedure is then repeated for the $\beta = 3$ and $\beta = 12$ sets of scattering curves, yielding qualitatively similar results for which the C and α values are summarized in Table 5.1. Although there is a hint of a systematic trend in $\overline{\alpha}$ deviating from $\sqrt{2\beta}$ as β is increased, given the numerical uncertainty already discussed (on the order of several percent), it would be pushing our analysis too far to attempt to calculate next order corrections to the Yukawa potential.

With the average least squares $\overline{\alpha}$ values determined, we can then identify the corresponding C values for each velocity curve by reference to their respective L contour map (e.g., Figure 5.13 for $\beta = 6$, $v = 0.5$). Both these C values and the calculated velocity scaling ratios are presented in Table 5.2. It is these $\overline{\alpha}$ and C values that were used to produce the theoretical fits shown in Figures 5.5 – 5.7. The theoretical curves fit the experimental data extremely well (as one expects with mean deviations on the order of 0.025). The scaling ratios shown in Table 5.2 are all within a few percent of the ideal values of 2.5, 5 and 2, further proof of the validity of the

Table 5.1: Calculation of $\overline{\alpha}$ and comparison with "ideal" value $\sqrt{2\beta}$.

β	v	$\alpha_{\min}$	$\overline{\alpha}$	$\sqrt{2\beta}$
3	0.1	2.41	2.46	2.45
	0.25	2.36		
	0.5	2.60		
6	0.1	3.55	3.40	3.46
	0.25	3.30		
	0.5	3.32		
12	0.1	4.79	4.62	4.90
	0.25	4.74		
	0.5	4.32		

Table 5.2: C values and velocity scaling ratios.

β	v	$C_v(\overline{\alpha})$	$\sqrt{\frac{C_{0.1}}{C_{0.25}}}$	$\sqrt{\frac{C_{0.1}}{C_{0.5}}}$	$\sqrt{\frac{C_{0.25}}{C_{0.5}}}$
3	0.1	3158	2.57	5.13	1.99
	0.25	476.6			
	0.5	120.2			
6	0.1	7245	2.39	4.91	2.05
	0.25	1265			
	0.5	300.2			
12	0.1	64560	2.49	5.23	2.11
	0.25	10450			
	0.5	2356			
"Ideal" scaling[a]			2.50	5.00	2.00

[a]Ideal velocity scaling is $\sqrt{\frac{C_{v_1}}{C_{v_2}}} = \frac{v_2}{v_1}$.

Table 5.3: Calculation of average Cv^2 values at a given β value.

β	v	Cv^2	$\overline{Cv^2}$
3	0.1	31.58	30.47
	0.25	29.79	
	0.5	30.05	
6	0.1	72.45	75.52
	0.25	79.06	
	0.5	75.05	
12	0.1	645.6	629.2
	0.25	653.1	
	0.5	589.0	

elastic scattering model and the choice of the Yukawa interaction potential.

We can look at our numerical data in still another way by appealing to a familiar example. For the (attractive) gravitational force problem involving two identical masses m, and using the same initial conditions as in Figure 5.2, one would have

$$\frac{V(r)}{T_0} = \frac{C}{r} \tag{5.28}$$

with $C = Nm/v^2$, N being a numerical factor. Note that the product Cv^2, (i) is invariant for a given mass and (ii) increases linearly with mass.

For the light bullet problem, independent of any interpretation, we can also form the product Cv^2 for different v values as a function of β. This data is presented in Table 5.3. The Cv^2 values are approximately constant for each β value, deviating with a small error consistent with our estimated numerical uncertainty from the average value $\overline{Cv^2}$. Analogous to the gravitational problem, $\overline{Cv^2}$ increases with increasing β or, from Figure 5.1, with increasing bullet energy P. In Figure 5.15, we have plotted $\overline{Cv^2}$ versus P, the experimental points being described by the linear equation $\overline{Cv^2} = 37.5P - 19.2$. The vertical cutoff (dashed line) corresponds to $P = P_{\text{min}}$, the

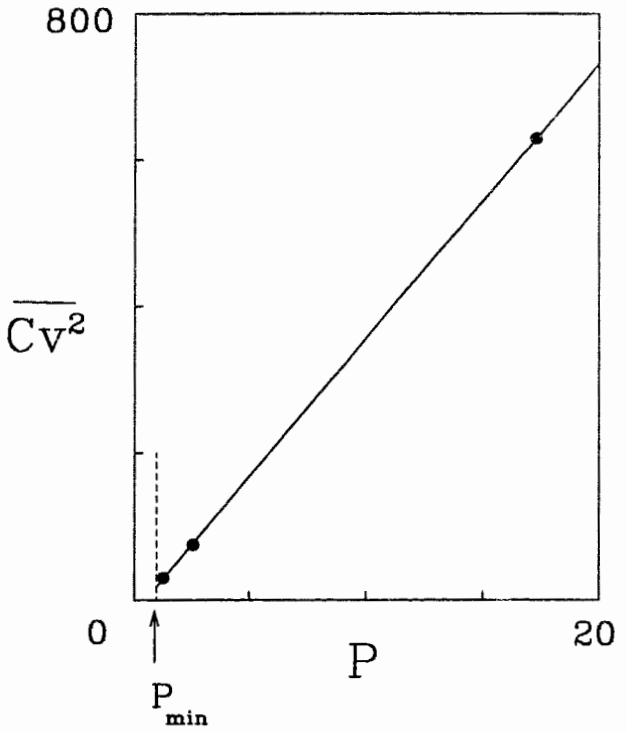

Figure 5.15: $\overline{Cv^2}$ versus bullet energy content P.

minimum energy required for light bullet formation.

Comparing with conditions (i) and (ii) on $\overline{Cv^2}$ for the gravitational problem, one finds that P appears to play the role of an effective mass with the caveat that there exists a minimum "mass" threshold for light bullet formation.

In this chapter, we have successfully determined the interaction force between π-phase shifted repulsive solitons. We turn now to a completely different analysis, a study of the so-called "spherical halo" states of the GNLSE.

Chapter 6

Stability of the higher bound states

Until this point we have considered only solitary wave solutions to the GNLSE of a particular qualitative form; namely, localized spherically symmetric pulses that are bright at the center and whose intensity decreases monotonically to zero with increasing radius. Our preoccupation with this form is justified for the following reasons. First, for all models considered, such solutions are found to be numerically stable against small perturbations for a range of propagation parameters. Second, their simple Gaussian-like profiles should make them relatively easy to produce with existing laser systems. However, there do exist other bullets with more complicated radial profiles but which still possess spherical symmetry. In fact, for a given propagation parameter β, there exist a family of localized solutions, the intensity profile of each member of the family being characterized by a different number of symmetric halos surrounding a bright central core.

An analogous scenario was recently discussed in a beautiful paper by Soto-Crespo *et al.* [So91] for the case of two-dimensional spatial solitons. In fact, it was this paper that provided the impetus for the current three-dimensional study [Ed96]. Soto-Crespo *et al.* considered the case of the transverse patterns formed in a continuous-wave beam under the influence of self-focusing in a saturable medium. Mathematically, the transverse beam profile is governed by an equation very much like the GNLSE but without the temporal dispersion term and using the appropriate two-dimensional Laplacian. These researchers considered the stability of solitary wave

solutions characterized by a number of symmetric rings surrounding a bright central spot. Numerical propagation of these higher bound states revealed them to be unstable to angular perturbations, the initially symmetric rings breaking up into a number of filaments which later underwent complicated dynamical interactions. A linear stability analysis was carried out by studying the evolution of angular perturbation eigenmodes of the form $\cos(m\theta)$, m an integer. It was found that the most unstable mode occurred for finite 'm', the value of m then determining the number of filaments formed during the initial beam breakup. Here, we follow a similar approach with perturbation eigenmodes suitable to the three-dimensional problem.

We will ignore the practical aspects of experimentally producing such complicated three-dimensional profiles except to note that the analogous two-dimensional spatial solitary wave solutions studied by Soto-Crespo *et al.* could be produced by virtue of an optical mask. The extension to a time dependent mask is certainly non-trivial but still within the realm of possibility. Regardless, the stability of the halo states is worthy of study as an interesting applied mathematics problem and we take comfort in the knowledge that this will not be the first time that theorists have studied the dynamics of a system that may well be impossible to prepare in a laboratory environment.

Not surprisingly, propagation of the three-dimensional halo states reveals them to be transversely unstable, the spherical symmetry of the outer shells being spontaneously broken as a result of the nonlinearity. After propagating a short distance, the halos begin to "clump" forming a number of angularly separated light bullets that travel off in various directions. As we shall see, while the dynamics of this process are quite complicated, the initial decay is understandable in terms of a (somewhat complicated) linear stability analysis.

The treatment will proceed as follows. Restricting the analysis to the physically realizable saturable model, we will choose a separable perturbation composed of an unspecified radial function $g(r,z)$ multiplied by a spherical harmonic $Y_\ell^m(\theta,\phi)$ and linearize the GNLSE about an initial halo state. This will result in a linear PDE for $g(r,z)$ that depends only upon the propagation parameter β, the number of halos n, and the 'ℓ' index of the spherical harmonic modes under study. For a given halo state and 'ℓ' value, we will then seek an exponentially growing radial perturbation function

$g(r,z) = g(r)\exp(\delta z)$. This formulation constitutes a difficult eigenvalue problem that, when solved, will allow the identification of which spherical harmonic modes are exponentially unstable. These predictions will then be compared with data obtained from direct simulation of the GNLSE.

6.1 Initial halo states

Recall that in a saturable anomalously-dispersive medium, the propagation of a three-dimensional plane-polarized envelope is governed by the generalized nonlinear Schrödinger equation (GNLSE),

$$i\frac{\partial E}{\partial z} + \frac{1}{2}\nabla^2 E + f(I=|E|^2)E = 0 \tag{6.1}$$

where ∇^2 is the Laplace operator in the coordinate system of choice and

$$f(I) = \frac{I}{1+aI} \tag{6.2}$$

where a is a reciprocal measure of the saturation intensity. Spherically symmetric solitary wave solutions to Eq. (6.1) are found by substituting the assumed form

$$E\left(r=\sqrt{t^2+x^2+y^2}, z\right) = U(r)\ \exp(i\beta z) \tag{6.3}$$

where β is a real propagation parameter that determines the bullet's radial profile. The real amplitude U is assumed to have its maximum value at $r = 0$, while $\mathrm{d}U/\mathrm{d}r$ and $\mathrm{d}^2U/\mathrm{d}r^2 \to 0$ as $r \to \infty$. With this assumed form, Eq. (6.1) reduces to the ordinary nonlinear differential equation

$$\frac{\mathrm{d}^2U}{\mathrm{d}r^2} + \frac{2}{r}\frac{\mathrm{d}U}{\mathrm{d}r} + 2U\left[f(U^2) - \beta\right] = 0 \tag{6.4}$$

In Chapter 3, it was shown that Eq. (6.4) admits a localized bright solitary wave solution with a Gaussian-like profile. In addition, one finds empirically that for a given propagation constant β, there exist a number of higher bound states characterized by

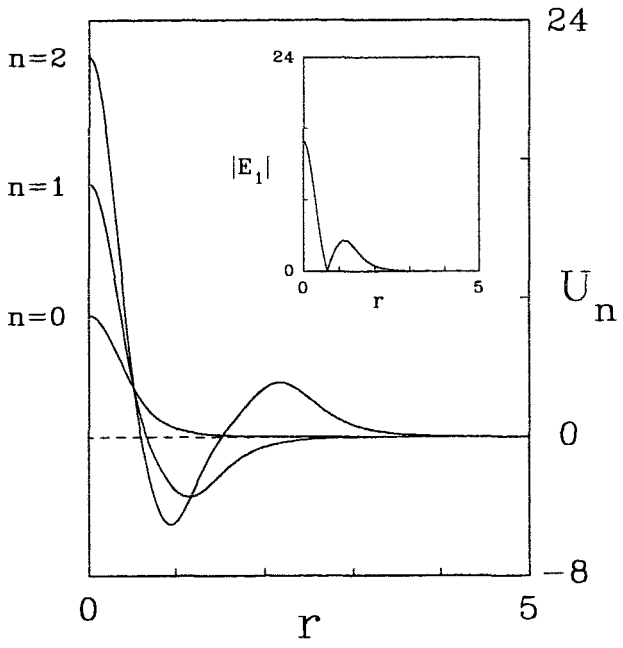

Figure 6.1: Radial field profiles for the $\beta = 3$ family of solutions. Inset: Square-root of the intensity of the one-halo state.

an increasing number of $U = 0$ crossings of the field. As a concrete example, Figure 6.1 shows the first few members of the $\beta = 3$ family of solutions. We label the members of a given family by U_i, the subscript i denoting the number of zero crossings. Using this nomenclature, U_0 corresponds to the familiar monotonically decreasing solutions of the previous chapters which only asymptotically approach $U = 0$. The solution U_1 corresponds to a solution whose profile has a single zero crossing, dipping below the positive axis to a minimum before asymptotically tending to $U = 0$ from below. The profile U_2 has two such zero crossings, and so on. Experimentally, however, one measures not the electric field of the envelope function but the intensity $I = |E|^2$. Consequently, each extraneous maximum or minimum becomes an intensity halo and thus the subscript of the field profile U_i can equivalently refer to the number of halos surrounding the central core.[1] For the sake of scale, rather than plot the square of the field, the inset of Figure 6.1 shows the radial profile of the modulus of the field, $|E_1| = \sqrt{U_1{}^2}$, the first bound state possessing a single halo.

For U_0 bullets, increasing the propagation parameter β resulted in taller wider solitary wave profiles. Figure 6.2 shows the result of varying β for single-halo solitary

[1]Note that the halo solutions do not simply correspond to the regular U_0 solutions with the addition of extraneous shells.

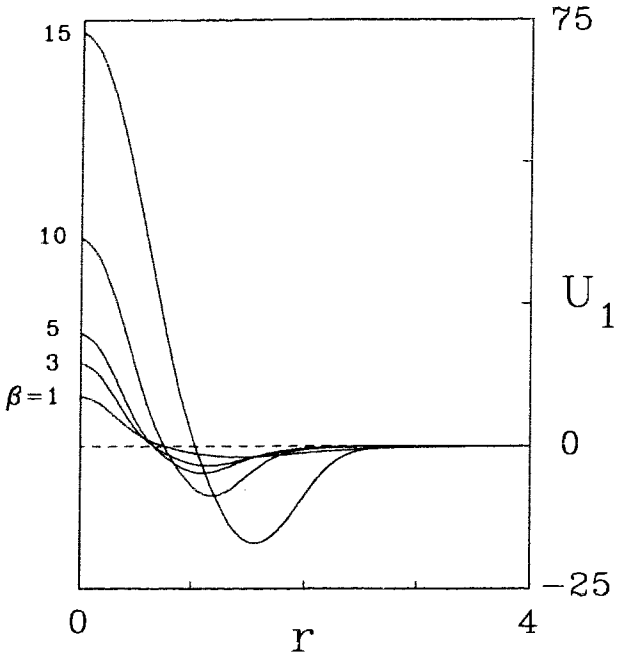

Figure 6.2: Effect of varying β on U_1 bullet profiles.

waves, the general trend being an increase in the central field value while the minima simultaneously deepen and move outwards towards larger radii; the situation for the higher bound states is qualitatively similar.

In Chapter 3, it was empirically demonstrated that a necessary condition for the stability of light bullets to small perturbations was that the propagation parameter β reside on a positive slope branch of the associated energy curve.[2] Let us then determine the energy curves for these higher bound states. For a given profile $U(r;\beta)$, we define the power

$$P(\beta) = \int_0^\infty U(r;\beta)^2\, r^2\, \mathrm{d}r \tag{6.5}$$

Numerically computing this integral for a spectrum of the allowable β values and the first three bound states results in the energy curves depicted in Figure 6.3. The P_0 curve is that shown previously in Figure 3.4. The energy curves for the higher bound states are qualitatively similar but displaced vertically on the log plot. As is the case for U_0 bullets, we might initially expect that the positive slope branches of the P_1 and P_2 curves are also stable against small perturbations. However, this "rule of thumb" is only a necessary condition for stability and pertains only to radial stability. We

[2]Successive positive slope branches can correspond to optical multistability.

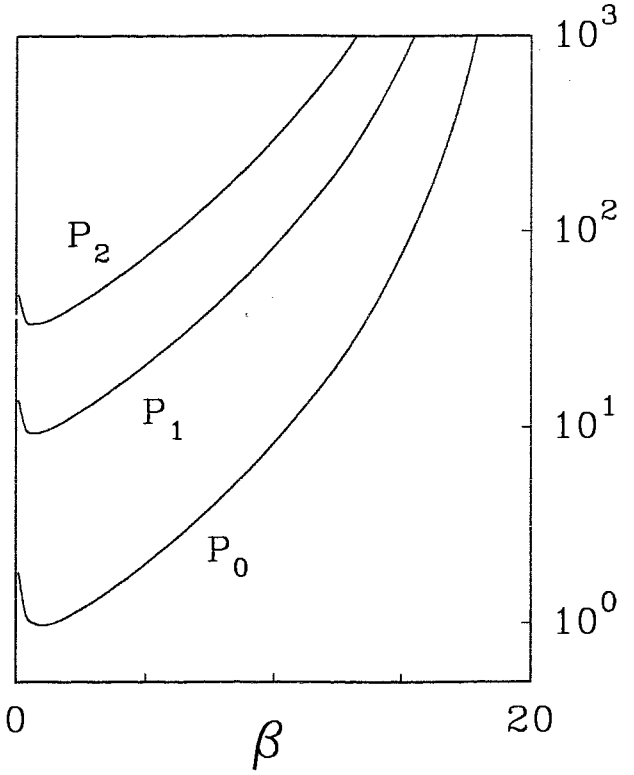

Figure 6.3: Energy curves for the first three bound states.

will see shortly that the higher states are transversely unstable, these complex solitary waves decaying into a number of stable light bullets on the positive-slope P_0 curve.

6.2 Sample halo state simulation

Rather than delve immediately into the stability analysis, this brief section is intended to impart a feeling for the typical dynamics of a halo state simulation. Hopefully this introduction will provide adequate motivation for the linear stability analysis presented in section 6.3. Quantitative simulation results for comparison with the predictions of the stability analysis will be presented later in section 6.4.

As an example, consider the $\beta = 3$, $n = 1$ radial profile depicted in Figure 6.1 as an initial condition to the GNLSE. As a slight modification, let the actual initial condition be

$$E(r,0) = [1 + \Gamma(t,x,y)]\ U(r) \tag{6.6}$$

where Γ is a small random noise term obeying the statistics

$$\begin{aligned} \langle \Gamma(t,x,y) \rangle &= 0\,, \\ \langle \Gamma(t,x,y)^2 \rangle &= \frac{1}{100} \end{aligned}$$

which is added in order to seed the instability. Although the halo states are unstable without this modification,[3] in such cases the evolving solution possesses the symmetry of the underlying computational mesh. With the addition of random noise, this finite-size effect disappears and one is left with a symmetry-breaking determined by the physics of the problem rather than the numerical method. This assertion was verified by varying the computational domain size and repeating the simulations with different realizations of the noise term.

The initial condition, Eq. (6.6), is centred on a 140^3 cartesian grid and propagated forward in z using the split-step Fourier method described earlier in Section 2.3. Figure 6.4 shows the volume rendered results of the simulation at six interesting z values. From $z = 0$ to approximately $z = 2.0$ (not shown), the initial state remains relatively stable. However, by frame (b) the outer shell has become aspherical and has begun to clump in two regions. By frame (c) this process is well developed and the halo has coalesced into a tube-like structure and single ball whereas the central core has remained relatively unaffected at the centre of the computational mesh. (This structure possesses a well-defined axis of cylindrical symmetry, a point we will return to later in a more quantitative fashion.) The lower bullet then begins to move towards the bottom-front corner of the mesh and, due to conservation of linear momentum, the tube structure begins to drift in the opposite direction, slowly expanding in diameter. By frame (d), the instability of the tube is manifestly evident as it begins to pinch off at four locations. By frame (e), this pinching effect has completely destroyed the tube and we are left with separated "clumps" of light. In frame (f) these clumps have stabilized and drifted to various parts of the mesh (the two linked bullets in frame (e) having fused together). In the final image, the bottom-front soliton begins to poke

[3] Intrinsic numerical noise due to truncation and round-off errors is sufficient to provoke the system to leave its initially symmetric state.

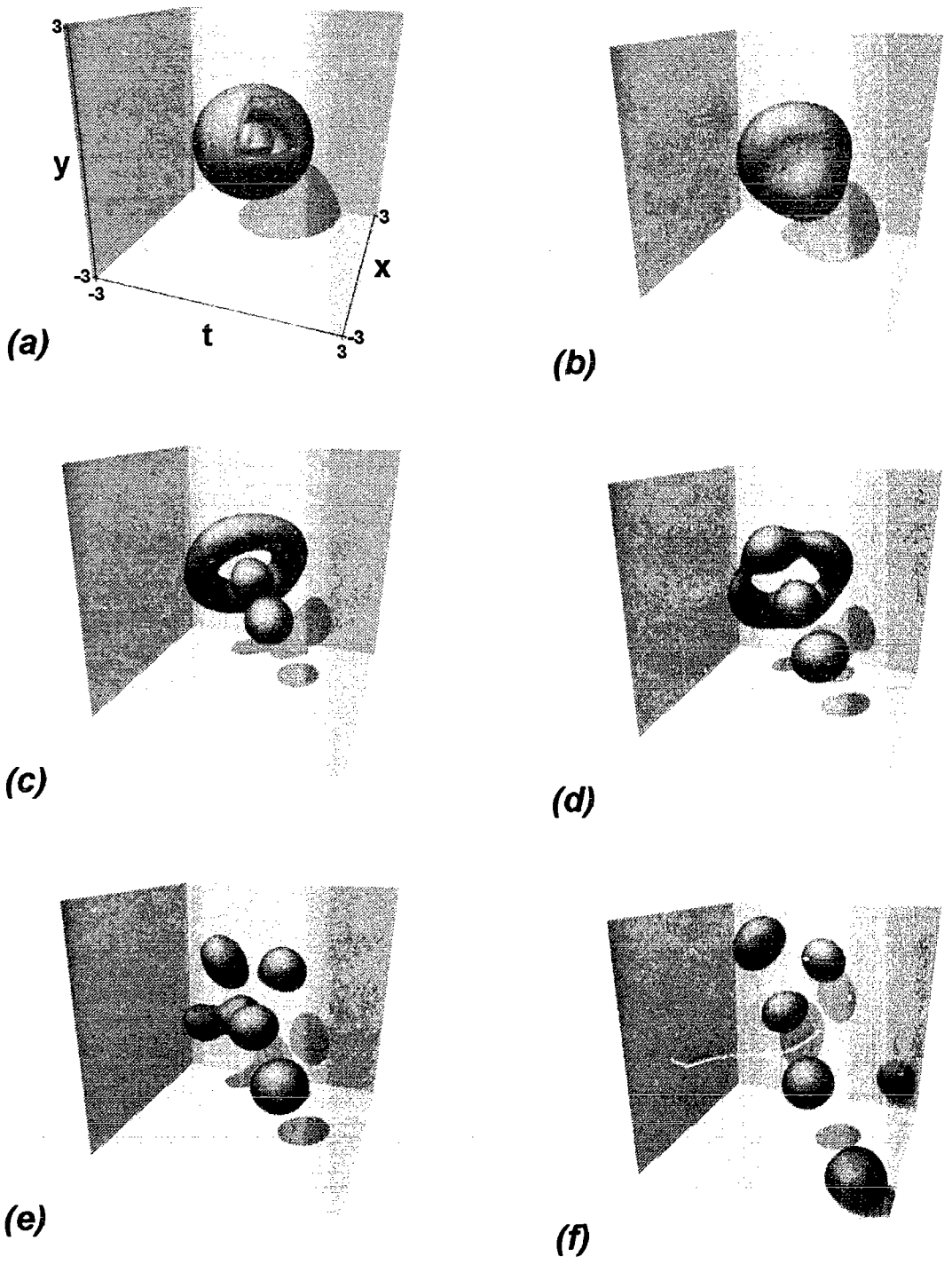

Figure 6.4: Simulation of the $\beta = 3$, $n = 1$ halo state reveals instability of the solution to a small amount of random noise. (a) $z = 0$, (b) $z = 2.4$, (c) $z = 2.8$, (d) $z = 3.2$, (e) $z = 3.4$ and (f) $z = 4.6$. Peak $|E| = 14.7$. In frame (a), an octant has been removed in order to visualize the central core.

through the back wall as it transits the periodic boundary.

The goal of the remainder of this chapter will be to explain this and other equally remarkable simulations in terms of a somewhat complicated numerical linear stability analysis.

6.3 Linear stability analysis

In this section we begin by deriving a linear PDE governing the initial evolution of a small perturbation to the halo state. This PDE is then solved using a Crank-Nicholson scheme whereupon the shapes and exponential growth rates of different perturbation eigenmodes are determined.

6.3.1 Derivation of the linear equation

Following Soto-Crespo [So91], we choose a separable perturbation to the stationary solution

$$E_n(r,z) = U_n(r)\exp(i\beta z) \tag{6.7}$$

of the form

$$E(r,\theta,\phi,z) = E_n(r,z) + \mu\, g(r,z)\,\Omega(\theta,\phi) \tag{6.8}$$

where n denotes the number of halos for the particular profile under study and μ is a small expansion parameter. Substitution of (6.8) into (6.1) yields

$$i\frac{\partial E_n}{\partial z} + i\mu\frac{\partial g}{\partial z}\Omega + \frac{1}{2}\nabla^2 E_n + \underbrace{\frac{\mu}{2}\nabla^2(g\Omega)}_{T_1} + \underbrace{f\left(|E_n+\mu g\Omega|^2\right)(E_n+g\Omega)}_{T_2} = 0 \tag{6.9}$$

Let us first consider the term T_1. In spherical polar coordinates,

$$\begin{aligned}\nabla^2(g\Omega) &= \frac{1}{r^2}\frac{\partial}{\partial r}\left(r^2\frac{\partial(g\Omega)}{\partial r}\right) + \frac{1}{r^2\sin\theta}\frac{\partial}{\partial\theta}\left(\sin\theta\frac{\partial(g\Omega)}{\partial\theta}\right) + \frac{1}{r^2\sin^2\theta}\frac{\partial^2(g\Omega)}{\partial\phi^2} \\ &= \frac{\Omega}{r^2}\frac{\partial}{\partial r}\left(r^2\frac{\partial g}{\partial r}\right) + \frac{g}{r^2}\underbrace{\left[\frac{1}{\sin\theta}\frac{\partial}{\partial\theta}\left(\sin\theta\frac{\partial\Omega}{\partial\theta}\right) + \frac{1}{\sin^2\theta}\frac{\partial^2\Omega}{\partial\phi^2}\right]}_{T_3}\end{aligned} \tag{6.10}$$

(6.11)

Letting $\Omega(\theta,\phi) = \Theta(\theta)\,\Phi(\phi)$,

$$T_3 = \frac{\Phi}{\sin\theta}\frac{\mathrm{d}}{\mathrm{d}\theta}\left(\sin\theta\frac{\mathrm{d}\Theta}{\mathrm{d}\theta}\right) + \frac{\Theta}{\sin^2\theta}\frac{\mathrm{d}^2\Phi}{\mathrm{d}\phi^2} \tag{6.12}$$

For reasons that will become apparent, let use choose $\Phi(\phi)$ to satisfy the differential equation

$$\frac{\mathrm{d}^2\Phi}{\mathrm{d}\phi^2} = -m^2\Phi \tag{6.13}$$

That is,

$$\Phi(\phi) \propto \mathrm{e}^{\pm im\phi} \tag{6.14}$$

Then, Eq. (6.12) can be rewritten as

$$T_3 = \left[\frac{1}{\sin\theta}\frac{\mathrm{d}}{\mathrm{d}\theta}\left(\sin\theta\frac{\mathrm{d}\Theta}{\mathrm{d}\theta}\right) - \frac{m^2}{\sin^2\theta}\Theta\right]\Phi \tag{6.15}$$

Let us further assume that $\Theta(\theta)$ satisfies the associated Legendre equation

$$\frac{1}{\sin\theta}\frac{\mathrm{d}}{\mathrm{d}\theta}\left(\sin\theta\frac{\mathrm{d}\Theta}{\mathrm{d}\theta}\right) + \ell(\ell+1)\Theta - \frac{m^2}{\sin^2\theta}\Theta = 0 \tag{6.16}$$

That is, we choose $\Theta(\theta)$ to be $P_\ell^m(\cos\theta)$, an associated Legendre function. This being the case, Eq. (6.15) becomes simply

$$T_3 = -\ell(\ell+1)\,\Theta\,\Phi \tag{6.17}$$

Note that

$$\Omega(\theta,\phi) = \Theta(\theta)\,\Phi(\phi) = P_\ell^m(\cos\theta)\,\mathrm{e}^{\pm im\phi} \equiv Y_\ell^m(\theta,\phi) \tag{6.18}$$

where $Y_\ell^m(\theta,\phi)$ are the familiar normalized spherical harmonic functions. The Laplacian acting on $g\Omega$ can thus be written as

$$\nabla^2(g\Omega) = \frac{\Omega}{r^2}\frac{\partial}{\partial r}\left(r^2\frac{\partial g}{\partial r}\right) - \frac{\ell(\ell+1)}{r^2}g\Omega \tag{6.19}$$

This is an important point: by choosing $\Omega(\theta,\phi)$ to be an unspecified spherical harmonic, we find that Eq. (6.19) contains no explicit angular dependence. Instead, as Y_ℓ^m is an eigenfunction of the transverse Laplacian, the angular dependence appears solely by virtue of the parameter 'ℓ'. In addition, the azimuthal index 'm' does not appear in the perturbation equation. This is interpreted as the stability analysis being able to distinguish which family of spherical harmonics are unstable but not which particular member or mixture dominates the evolution.

Next, let us consider the term T_2 in Eq. (6.9) with

$$f(I) = \frac{I}{1+aI} \tag{6.20}$$

and

$$k(r,\theta,\phi,z) \equiv g(r,z)\,\Omega(\theta,\phi) \tag{6.21}$$

To first order in the small parameter μ,

$$\begin{aligned} T_2 &= \frac{|E_n+\mu k|^2}{1+a|E_n+\mu k|^2}(E_n+k) \\ &= \frac{|E_n|^2}{1+a|E_n|^2}E_n + \mu\frac{2|E_n|^2k + a|E_n|^4k + {E_n}^2k^*}{(1+a|E_n|^2)^2} \end{aligned} \tag{6.22}$$

A minor complication is the k^* term. Our goal is to choose functions $\Omega(\theta,\phi)$ such that the linear equation contains no explicit angular dependence. In other words, Ω is to be an eigenfunction of the linearized equation. This being the case, we require

$$(g\Omega)^* = g^*\Omega \tag{6.23}$$

As $\Theta(\theta)^* = P_\ell^m(\cos\theta)^* = P_\ell^m(\cos\theta) = \Theta(\theta)$, we must therefore insist upon a minor

restriction on the generality of the solution of Eq. (6.13), namely,

$$\Phi(\phi)^* = \Phi(\phi) \tag{6.24}$$

such that the azimuthal function is real rather than the complex exponential initially proposed in Eq. (6.14).

The term T_2 can thus be written as

$$T_2 = f(|E_n|^2)E_n + \mu \frac{2|E_n|^2 g + a|E_n|^4 g + {E_n}^2 g^*}{(1+a|E_n|^2)^2}\,\Omega \tag{6.25}$$

With these simplifications of T_1 and T_2, Eq. (6.9) then becomes

$$i\frac{\partial E_n}{\partial z} + i\mu\frac{\partial g}{\partial z}\Omega + \frac{1}{2}\nabla^2 E_n + \frac{\mu\Omega}{2r^2}\frac{\partial}{\partial r}\left(r^2\frac{\partial g}{\partial r}\right) - \frac{\mu\ell(\ell+1)}{2r^2}g\Omega + f(|E_n|^2)E_n + \mu\frac{2|E_n|^2 g + a|E_n|^4 g + {E_n}^2 g^*}{(1+a|E_n|^2)^2}\,\Omega = 0 \tag{6.26}$$

Terms 1, 3, and 6 form an identity leaving a linear PDE for the evolution of the radial perturbation function

$$i\frac{\partial g}{\partial z} + \frac{1}{2r^2}\frac{\partial}{\partial r}\left(r^2\frac{\partial g}{\partial r}\right) - \frac{\ell(\ell+1)}{2r^2}g + \frac{2|E_n|^2 g + a|E_n|^4 g + {E_n}^2 g^*}{(1+a|E_n|^2)^2} = 0 \tag{6.27}$$

Note that this equation for $g(r,z)$ only depends upon the initial halo profile (determined by β) and the ℓ index of the spherical harmonic family under study.

To study the stability of a particular family of modes, we then seek exponentially growing solutions to the radial perturbation function of the form

$$g(r,z) = g(r)\,\mathrm{e}^{\delta z} \tag{6.28}$$

Substitution of Eq. (6.28) into Eq. (6.27) constitutes a challenging eigenvalue problem, even computationally. To solve this problem, there are two possible approaches. One could perform a truncated Fourier-Bessel decomposition of both E_n and $g(r)$ and then solve a coupled set of linear ODEs for the z evolution of the expansion

coefficients. This is the approach taken by Kolokolov and Sykov [Ko75] for a similar two-dimensional problem but Soto-Crespo and co-workers found that some of their conclusions were erroneous. An alternative approach [So91], and the one we follow here, is to choose a small random initial condition for $g(r, z=0)$ which is then numerically evolved according to Eq. (6.27). If this family of modes is unstable, an exponentially growing profile should make itself evident. The rationale is that although such a random initial condition will contain a mixture of all possible eigenmodes, the long term growth will be dominated by that particular eigenmode possessing the largest growth constant. The modal growth constant δ_ℓ can then be calculated numerically according to

$$\delta_\ell = \frac{1}{\Delta z}\left[\ln|g(r, z+\Delta z)| - \ln|g(r, z)|\right] \tag{6.29}$$

While Eq. (6.29) is true by definition in the limit as $\Delta z \to 0$ for the case when $g(r, z)$ contains only a single eigenmode, if the above hypothesis is correct, $\delta_\ell(z)$ should converge with increasing z.

6.3.2 Numerical method

Numerically then, how does one solve Eq. (6.27)? As we are studying stability, it seems reasonable to choose a numerical scheme that is unconditionally stable ensuring that any exponential growth witnessed is mathematically real and not an artifact of the numerical method. Consequently, Eq. (6.27) is solved using a Crank-Nicholson [Pr86, Se88] algorithm on a 500-point equispaced radial mesh.

Letting $g = u + iv$, and noting that

$$E_n{}^2 = U^2[\cos(2\beta z) + i\sin(2\beta z)] \tag{6.30}$$

where we have dropped the halo index subscript on U for clarity in what follows. Equation 6.27 can be written as two real coupled PDEs, viz.

$$-\frac{\partial v}{\partial z} + \frac{1}{2}\nabla_r^2 u - \frac{\ell(\ell+1)}{2r^2}u + \frac{(2+aU^2)U^2}{(1+aU^2)^2}u + \frac{U^2\cos(2\beta z)}{(1+aU^2)^2}u + \frac{U^2\sin(2\beta z)}{(1+aU^2)^2}v = 0 \tag{6.31}$$

and

$$\frac{\partial u}{\partial z}+\frac{1}{2}\nabla_r^2 v-\frac{\ell(\ell+1)}{2r^2}v+\frac{(2+aU^2)U^2}{(1+aU^2)^2}v+\frac{U^2\sin(2\beta z)}{(1+aU^2)^2}u-\frac{U^2\cos(2\beta z)}{(1+aU^2)^2}v=0 \quad (6.32)$$

where the radial Laplacian

$$\nabla_r^2 \equiv \frac{1}{r^2}\frac{\partial^2}{\partial r^2}+\frac{2}{r}\frac{\partial}{\partial r} \quad (6.33)$$

To solve these equations numerically, define an equally spaced mesh at radii $r=r_j$ with $j=1\ldots n$ where $r_j=(j-1)\Delta r$ and Δr is the intramesh spacing. The values of the fields u and v at the boundaries are allowed to float freely but the first derivatives are pinned to zero. With superscripts denoting the z direction, implicit discretizations for the field u are

$$\left.\frac{\partial u}{\partial z}\right|_{r=r_j}=\frac{u_j^{n+1}-u_j^n}{\Delta z} \quad (6.34)$$

and

$$\begin{aligned}\left[\frac{\partial^2 u}{\partial r^2}+\frac{2}{r}\frac{\partial u}{\partial r}\right]\Bigg|_{r=r_j} &= \frac{1}{\Delta r^2}\left[u_{j-1}^{n+1}-2u_j^{n+1}+u_{j+1}^{n+1}\right]+\frac{2}{r_j}\left[\frac{u_{j+1}^{n+1}-u_{j-1}^{n+1}}{2\Delta r}\right] \\ &= \frac{1}{\Delta r^2}\left[\left(1-\frac{\Delta r}{r_j}\right)u_{j-1}^{n+1}-2u_j^{n+1}+\left(1+\frac{\Delta r}{r_j}\right)u_{j+1}^{n+1}\right] \quad (6.35)\end{aligned}$$

Note that the first discretization is centred mid-mesh at $(n+1/2)$. We can also center the spatial discretization at $(n+1/2)$ by averaging with a similar version at timestep n, viz.

$$\begin{aligned}\left[\frac{\partial^2 u}{\partial r^2}+\frac{2}{r}\frac{\partial u}{\partial r}\right]\Bigg|_{r=r_j} &= \frac{1}{2\Delta r^2}\left[\left(1-\frac{\Delta r}{r_j}\right)u_{j-1}^{n+1}-2u_j^{n+1}+\left(1+\frac{\Delta r}{r_j}\right)u_{j+1}^{n+1}\right]+ \\ &\quad \frac{1}{2\Delta r^2}\left[\left(1-\frac{\Delta r}{r_j}\right)u_{j-1}^{n}-2u_j^{n}+\left(1+\frac{\Delta r}{r_j}\right)u_{j+1}^{n}\right] \quad (6.36)\end{aligned}$$

Substitution of these and their analogous discretizations for the field v into Eqs.(6.31)

and (6.32) followed by a healthy dose of subscript and superscript laden algebra yields,

$$\frac{1}{4\Delta r^2}\left(1-\frac{\Delta r}{r_j}\right)u_{j-1}^{n+1}+\left[-\frac{1}{2\Delta r^2}-\frac{\ell(\ell+1)}{4r_j^2}+\frac{(2+aU^2)}{2(1+aU^2)^2}U^2+\frac{U^2\cos(2\beta z)}{2(1+aU^2)^2}\right]u_j^{n+1}+$$
$$\left[-\frac{1}{\Delta z}+\frac{U^2\sin(2\beta z)}{(1+aU^2)^2}\right]v_j^{n+1}+\frac{1}{4\Delta r^2}\left(1+\frac{\Delta r}{r_j}\right)u_{j+1}^{n+1}=-\frac{1}{4\Delta r^2}\left(1-\frac{\Delta r}{r_j}\right)u_{j-1}^{n}+$$
$$\left[\frac{1}{2\Delta r^2}+\frac{\ell(\ell+1)}{4r_j^2}-\frac{(2+aU^2)}{2(1+aU^2)^2}U^2-\frac{U^2\cos(2\beta z)}{2(1+aU^2)^2}\right]u_j^{n}+\left[-\frac{1}{\Delta z}-\frac{U^2\sin(2\beta z)}{(1+aU^2)^2}\right]v_j^{n}-$$
$$\frac{1}{4\Delta r^2}\left(1+\frac{\Delta r}{r_j}\right)u_{j+1}^{n} \tag{6.37}$$

and

$$\frac{1}{4\Delta r^2}\left(1-\frac{\Delta r}{r_j}\right)v_{j-1}^{n+1}+\left[-\frac{1}{2\Delta r^2}-\frac{\ell(\ell+1)}{4r_j^2}+\frac{(2+aU^2)}{2(1+aU^2)^2}U^2-\frac{U^2\cos(2\beta z)}{2(1+aU^2)^2}\right]v_j^{n+1}+$$
$$\left[\frac{1}{\Delta z}+\frac{U^2\sin(2\beta z)}{(1+aU^2)^2}\right]u_j^{n+1}+\frac{1}{4\Delta r^2}\left(1+\frac{\Delta r}{r_j}\right)v_{j+1}^{n+1}=-\frac{1}{4\Delta r^2}\left(1-\frac{\Delta r}{r_j}\right)v_{j-1}^{n}+$$
$$\left[-\frac{1}{2\Delta r^2}+\frac{\ell(\ell+1)}{4r_j^2}-\frac{(2+aU^2)}{2(1+aU^2)^2}U^2+\frac{U^2\cos(2\beta z)}{2(1+aU^2)^2}\right]v_j^{n}+\left[\frac{1}{\Delta z}-\frac{U^2\sin(2\beta z)}{(1+aU^2)^2}\right]u_j^{n}-$$
$$\frac{1}{4\Delta r^2}\left(1+\frac{\Delta r}{r_j}\right)v_{j+1}^{n} \tag{6.38}$$

Forming the column vector

$$\vec{x}=\begin{pmatrix}u_1\\v_1\\u_2\\v_2\\\vdots\\u_n\\v_n\end{pmatrix} \tag{6.39}$$

Equations (6.37) and (6.38) form a matrix system

$$\tilde{A}\,\vec{x}=\vec{b} \tag{6.40}$$

where the matrix $\tilde{A}$ has the following banded structure

$$\tilde{A} = \begin{pmatrix} \bullet & \bullet & \bullet & \circ & \circ & \circ & \circ & \circ \\ \bullet & \bullet & \circ & \bullet & \circ & \circ & \circ & \circ \\ \bullet & \circ & \bullet & \bullet & \bullet & \circ & \circ & \circ \\ \circ & \bullet & \bullet & \bullet & \circ & \bullet & \circ & \circ \\ \circ & \circ & \bullet & \circ & \bullet & \bullet & \bullet & \circ \\ \circ & \circ & \circ & \bullet & \bullet & \bullet & \circ & \bullet \\ \circ & \circ & \circ & \circ & \bullet & \circ & \bullet & \bullet \\ \circ & \circ & \circ & \circ & \circ & \bullet & \bullet & \bullet \end{pmatrix} \tag{6.41}$$

the empty and filled circles representing zero and nonzero matrix elements, respectively.

The algorithm is implemented as follows. We begin by choosing a propagation constant β and halo index n which then uniquely determines the initial radial profile $U_n(r)$. One then selects the family of spherical harmonic modes under study by choosing the integer parameter ℓ. Finally, we set $z = 0$ and load the computational mesh with small random initial values for the real fields u and v. Then:

1. Load the column vector $\vec{b}$ based on the current values of u and v.
2. Load the matrix $\tilde{A}(r, z)$.
3. Solve the banded matrix system of Eq. (6.40) for the solution vector $\vec{x}$.
4. Extract the new values of the fields u and v from the alternating structure of $\vec{x}$.
5. Increment z by Δz and return to step 1.

As the simulation proceeds, the modal growth rate is calculated from Eq. (6.28). Based on this prescription,

$$\delta_\ell = \delta_\ell(r)$$

and thus the growth rate is calculated at each radial mesh point. Then, as $|g|$ evolves, one continues the simulation until the growth rate δ_ℓ converges and each part of the emerging eigenmode is seen to be growing at the same rate.

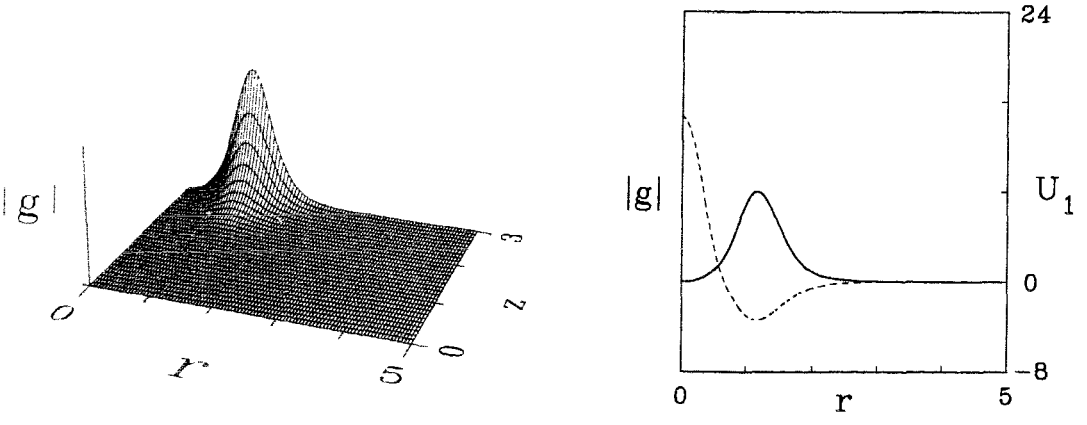

(a) Growth of $g(r)$ from a small random initial condition.

(b) Solid curve: $g(r)$. Dashed curve: initial $\beta = 3$ one-halo state.

Figure 6.5: Calculation of the radial perturbation eigenfunction for $\beta = 3$, $n = 1$ and $\ell = 3$.

6.3.3 Predictions: one-halo modal analysis

As a concrete example, using the above numerical method to solve Eq. (6.27), let us examine the stability of the $\beta = 3$, $n = 1$ halo state simulated in Section 6.2. The method requires that we choose a family of spherical harmonic modes for analysis, so, with some clairvoyancy, we select $\ell = 3$ as being a particularly important family of modes. This being the case, one finds that from a very small random initial condition for

$$g(r, 0) = u(r, 0) + v(r, 0) \tag{6.42}$$

an exponentially growing radial profile $|g|$ emerges as shown in Figure 6.5(a). The vertical scale is omitted as the absolute height of the pulse is not important. Rather, the salient feature is that by the end of the simulation, the growth of the entire pulse has converged[4] to an exponential rate of $\delta_3 = 3.75$. In Figure 6.5(b), we plot the radial profile $|g(r)|$ versus r and for comparison, the initial condition $U_1(r)$. Note

[4]This is true for all points across the pulse, i.e., the radial profile grows in a scale-invariant way.

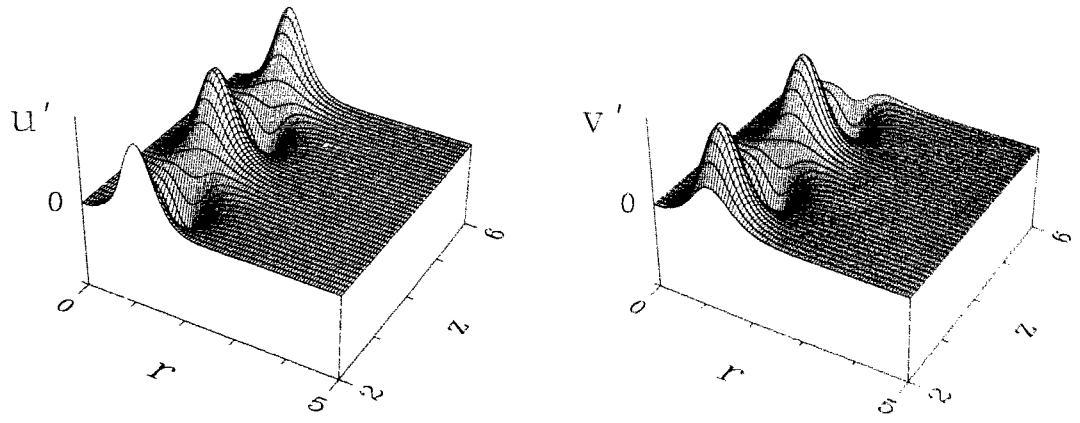

(a) (b)

Figure 6.6: Real and imaginary components of g scaled to eliminate the exponential growth and ease visualization of the periodicity.

that the perturbation eigenmode is concentrated at the radius of the halo and acts negligibly upon the core of the halo state. This turns out to be a result independent of the mode under study and explains two features of our sample simulation: (i) why the dynamics initially appear confined to the outer shell and (ii) why the central core is relatively unaffected by the instability.

The astute reader may be wondering about the real and imaginary parts of $g(r, z)$. The underlying fields u and v display periodic behaviour but as they are also growing exponentially at the rate $\delta_3 = 3.75$, this periodicity is difficult to visualize. Therefore, we introduce the scaled fields

$$u'(r, z) = u(r, z) \exp(-\delta_\ell z) \tag{6.43}$$

and

$$v'(r, z) = v(r, z) \exp(-\delta_\ell z) \tag{6.44}$$

such that

$$|g'(r, z)| \equiv \sqrt{u'(r, z)^2 + v'(r, z)^2} \tag{6.45}$$

remains constant in z. Figure 6.6 shows the evolution of these two scaled fields from

$z = 2$–6. Recall that the initial state $E_1(r, z)$ also possessed a phase evolution

$$E_1(r, z) = U_1(r) \exp(i\beta z) \tag{6.46}$$

An obvious question then arises, namely, although $|g|$ acts at the halo radius, are the periodicities of the real and imaginary parts of g commensurate with the phase evolution of E_1? If, in fact, they are not commensurate, the exponentially growing modes will not drive the initial state in a "fixed" direction, instead taking energy into and out of (θ, ϕ) locations that are Y_3^m mode extrema. From Eq. (6.46), the characteristic repeat length is determined by

$$2\pi i = i\beta z_{\mathrm{p}} \tag{6.47}$$

so that

$$z_{\mathrm{p}} = \frac{2\pi}{\beta} \tag{6.48}$$

Thus, for $\beta = 3$, $z_{\mathrm{p}} = 2.1$. Careful measurement of the periodicities of u' and v' show that they are equal to $2.1 \pm 1\%$. Thus, for all intents and purposes, one can think of the evolution of $|E|$ in terms of the shapes of $|g|$ and the unstable Y_ℓ^m.

Repeating the above analysis for other modes $\ell = 0, 1, 2, 4, 5, 6, \ldots$, one finds that only for modes $\ell = 1, 2, 3, 4$ do exponentially growing pulses arise; the other modes presumably possess either negative or purely imaginary eigenvalues and can thus be classified as stable. The growth rates of the four modes determined to be unstable are displayed in Figure 6.7. Thus, the $\ell = 3$ mode is found to be most unstable and, as the growth is exponential, we hypothesize that this mode will dominate the long term evolution and that the simulation results should be consistent with a Y_3^m-type instability.

At this point we have a perplexing problem. In terms of the simulation results, how does a Y_3^m instability manifest itself? As the family consists of the four functions Y_3^0, Y_3^1, Y_3^2 and Y_3^3, does one observe:

- One particular dominant mode?

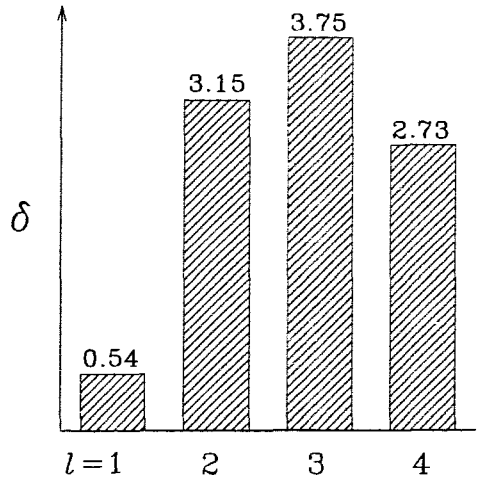

Figure 6.7: Exponential growth rates of the four unstable $\beta = 3$, Y_ℓ^m modes.

- An equal mixture of modes?
- An arbitrary linear combination of modes?

To answer this question, the only recourse is a series of numerical experiments with differing realizations of the noise term followed by spherical harmonic analysis of the resultant simulation data. Before presenting and analyzing the simulation data, we conclude this section by summarizing the growth rates for all one-halo states.

The analysis carried out above pertains only to the $\beta = 3$ single-halo state U_1. This same procedure can be carried out for all bullets in the allowable range $0 < \beta < 20$ resulting in the growth rate curves shown in Figure 6.8. An important result is that the $\ell = 3$ mode dominates for all single halo states. This is in marked contrast to the situation in two-dimensions where a crossover occurred at a critical β value. Such a crossover divides the spectrum of bullets into two classes which have different stability properties and resultant long-term evolution.

6.4 One-halo results and analysis

Soto-Crespo *et al.*'s comparison between the predictions of linear stability analysis and simulation in two dimensions was relatively simple. The analysis predicted a specific 'm' mode of the perturbation $\cos(m\theta)$ to be unstable. A visual inspection of the numerical data then clearly showed the initially symmetric circular halo break

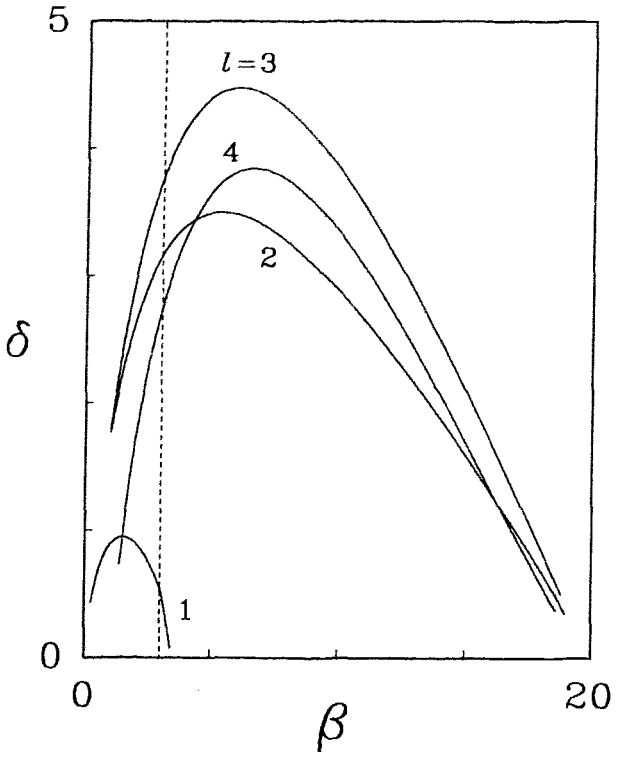

Figure 6.8: Summary of unstable growth rates for all single-halo bullets.

up into m spots - the m-fold symmetry being unmistakable. The situation in three dimensions is much more complicated for two reasons:

1. The linear stability analysis only predicts the ℓ value of the unstable mode. This is interpreted as all members of the Y_ℓ^m family possibly being present.

2. The functions Y_ℓ^m, defined over the surface of a sphere, are much more complicated than simple cosine functions. Thus, one cannot depend on the human mind to identify a pattern as, for example, being obviously Y_3^2.

The approach then is to quantitatively analyze the simulation data by the method of spherical harmonic analysis. That is, choosing a characteristic radius r^*, the field $E(r^*, \theta, \phi)$ is decomposed into its spherical harmonic components. Initially, the field is spherically symmetric and all of the harmonic content will exist in the DC mode Y_0^0. However, as the simulation proceeds, the system decays and energy will flow from Y_0^0 into the unstable exponentially growing modes.

For performing the spherical harmonic analysis of the real function $|E|$, we utilize the excellent package SPHEREPACK[5] written by Paul Swarztrauber of the U.S. National Center for Atmospheric Research. Defining $n_{\rm lat}$ as the number of colatitudes on the grid and $n_{\rm lon}$ as the number of distinct longitudinal points, the discretized equispaced angles θ_i and ϕ_j are given by

$$\begin{aligned} \theta_i &= (i-1)\tfrac{\pi}{n_{\rm lat}-1}, \quad i = 1 \ldots n_{\rm lat} \\ \phi_j &= (j-1)\tfrac{2\pi}{n_{\rm lon}-1}, \quad j = 1 \ldots n_{\rm lon} \end{aligned} \tag{6.49}$$

Choosing the radius of the halo minimum r^* as the radius of interest, we require the value of the field $|E|$ at these locations. As the simulation data is defined on a cartesian mesh, this necessitates interpolation [Pr86] of $|E|$ from the regular grid (t, x, y) to the locations (r^*, θ_i, ϕ_j).[6] In addition, with reference to the volume renderings of Figure 6.4, we take the "north-pole" to be vertical, i.e., normal to the t-x plane through centre of the mesh.

SPHEREPACK is able to determine the coefficients A_ℓ^m and B_ℓ^m such that

$$\begin{aligned} |E(r^*, \theta_i, \phi_j)| &= \frac{1}{2} \sum_{\ell=0}^{n_{\rm lat}-1} A_\ell^0 P_\ell^0(\theta_i) + \\ &\quad \sum_{m=1}^{m_{\rm max}} \sum_{\ell=m}^{n_{\rm lat}-1} \left[A_\ell^m \cos(m\phi_j) - B_\ell^m \sin(m\phi_j) \right] P_\ell^m \end{aligned} \tag{6.50}$$

where $P_\ell^m(\theta)$ are the normalized associated Legendre functions and $m_{\rm max} = (n_{\rm lon} + 2)/2$. Rather than considering both A and B, note that

$$C \equiv \sqrt{A^2 + B^2} \tag{6.51}$$

is invariant to rotations about the pole; as we are not interested in the absolute orientation of the system, consideration of the C_ℓ^m will suffice.

[5]SPHEREPACK and other scientific computing packages are available over the Internet from the software repository Netlib, accessible via the World Wide Web at <URL:http://www.netlib.org/>.

[6]For the $\beta = 3$ simulation presented earlier, the radius for which the peak of the halo occurs is $r^* = 1.15$. How many θ_i and ϕ_j values should one optimally choose? With a cubic domain of 140^3 spanning $-3 \le (t, x, y) \le 3$, roughly one requires $4\pi(1.15/3.0 \cdot 70)^2 \simeq 9127$ points.

Figure 6.9 shows the results of the spherical harmonic analysis corresponding to the simulation depicted earlier in Figure 6.4. The data is restricted to the modes up to and including $\ell = 5$, the modes above this value containing negligible energy. In addition, due to its large initial content, the DC mode Y_0^0 is omitted and displayed separately in Figure 6.10. A sharp transition in the DC component occurs in the neighbourhood of $z = 3$ corresponding to the tube and lower forming bullet moving away from SPHEREPACK's radius of interest. As predicted, we see that Y_3^m modes dominate the evolution[7] although the Y_3^1 mode is curiously absent. This analysis, however, assumes that the north-pole is as chosen, normal to the $t - x$ plane. But we have absolutely no justification for this arbitrary choice! In fact, choosing the pole normal to the $t - y$ plane would have led to a different mixing of the Y_3^m components. Note, however, that as the initially spherical halo decomposes, it spontaneously chooses a symmetry axis aligned through the centre of the tube and both of the forming bullets. Taking the lower soliton to be at the north-pole,[8] Figure 6.11 shows the harmonic analysis with respect to this new coordinate system. With such a choice, all of the interesting harmonic content is contained in the Y_3^0 mode. As $m = 0$, $Y_3^0(\theta, \phi) = P_3^0(\theta)$ and the dominant unstable growth mode thus possesses azimuthal symmetry. The associated Legendre function

$$P_3^0(\theta) = \frac{7}{4\pi} \cos\theta \left(\cos^2\theta - \frac{3}{2} \sin^2\theta \right) \tag{6.52}$$

is plotted in Figure 6.12(a) and allows us to explain how both the torus and the north-pole light bullet of Figure 6.4(c) coalesce out of the initially symmetric halo. (The origin of the central light bullet was already explained in terms of halo localization of the radial perturbation function, i.e., we observed that $g(r)$ acts only at the radius of the outer shell and negligibly at the origin.) To facilitate the comparison between this curve and the simulation data, Figure 6.12(b) depicts the interpolated field $|E(r^*, \theta, \phi)|$ at frame (c) of the simulation. Note that the rotation axis of this

[7] At least up until the formation of the tube structure which is already far beyond the realm of the linear analysis.

[8] This choice is arbitrary but facilitates later analysis. C is unaffected by such a π rotation of the data.

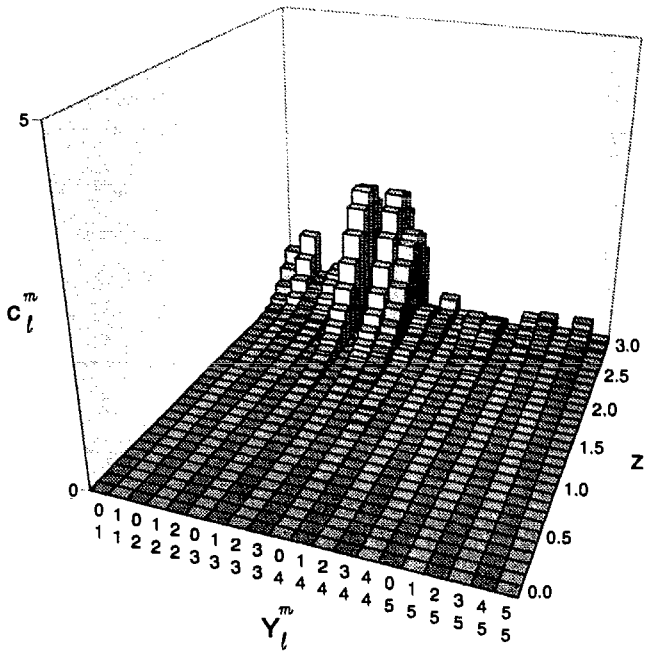

Figure 6.9: z evolution of the spherical harmonic components.

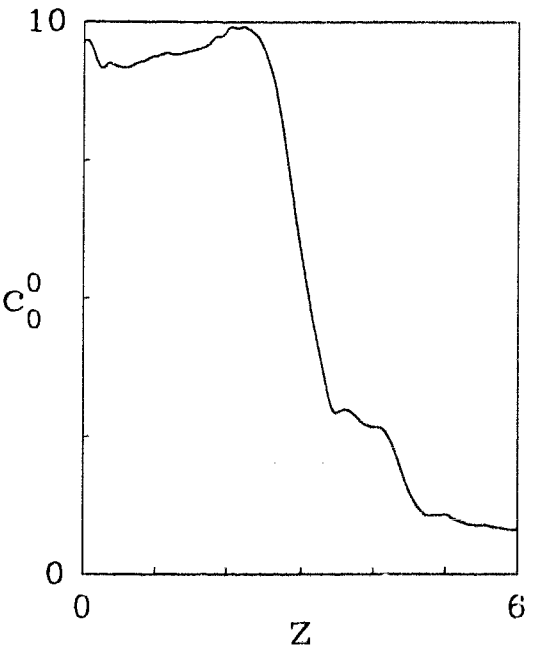

Figure 6.10: Harmonic content of the DC component.

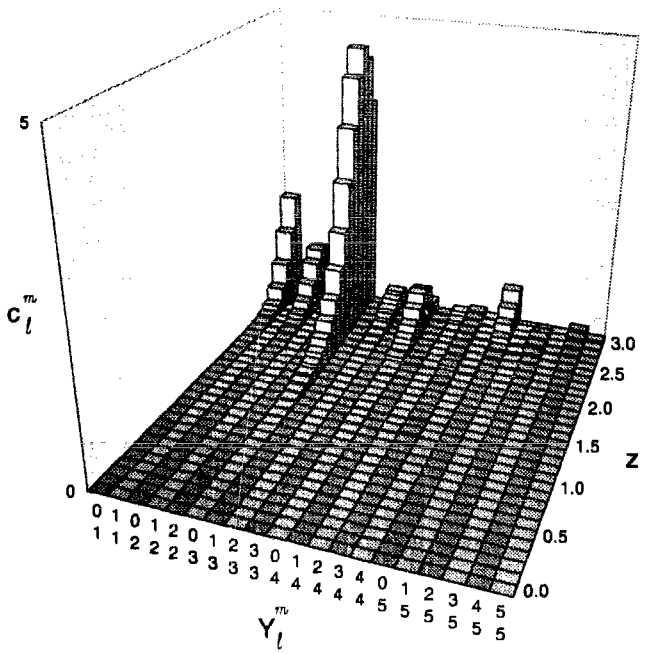

Figure 6.11: z evolution of the spherical harmonic components (rotated pole).

figure is *not* the vertical in the volume rendered frame. Rather, the data has been rotated such that the bright band in the southern hemisphere corresponds to the torus while the bright spot at the north pole corresponds to the lowermost bullet in Figure 6.4(c). This being the case, the correspondence between the simulation data and P_3^0 becomes rather obvious. At θ locations where P_3^0 is positive, the field grows. Thus, energy will gather at both the north pole and in the vicinity of $5\pi/8$. Due to the axial symmetry, the latter case results in the formation of a tube at the given latitude. At θ locations where P_3^0 is negative, the intensity decreases resulting both in a dark band in the northern hemisphere and a dark south-pole.

As in the two-dimensional case, the dynamics following the formation of the torus (frames (d)–(f) in Figure 6.4) are complicated. For example, our analysis does not predict the subsequent uneven pinching at four azimuthal angles. This should not be particularly surprising as the theoretical predictions are based on a perturbation treatment about the original symmetric state and not this new metastable torus. The propagation constants of the final states can be determined by least-squares fitting the

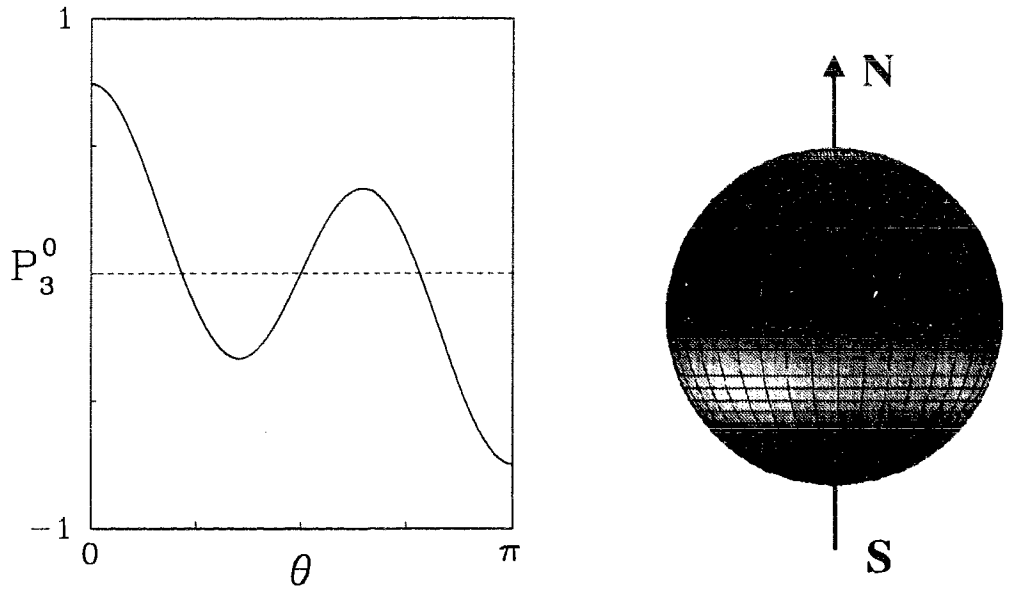

(a) Associated Legendre function $P_3^0(\theta)$.

(b) Interpolated and rotated simulation data.

Figure 6.12: Comparison between stability analysis and numerical experiment. (See accompanying text.)

radial profiles (not shown), after which it is seen that a mere 17% of the original one-halo energy content is unaccounted for and has thus been radiated away. Although the long-term dynamics are complicated, the recurrent theme that with sufficient localization of energy, saturable media naturally form stable light bullets is clearly evident.

Of course, because we are witnessing an instability, the results of a specific simulation will depend on the realization of the noise term. That is, different "seed" values for the random number generator used to numerically perturb the initial state can cause the system to choose a different axis of symmetry with respect to our fixed frame. In addition, one often finds that azimuthal decay of the torus occurs while it is still in the process of formation. Nonetheless, empirically we find that a torus-like structure always forms revealing that, in answer to our earlier question, the Y_3^0 mode

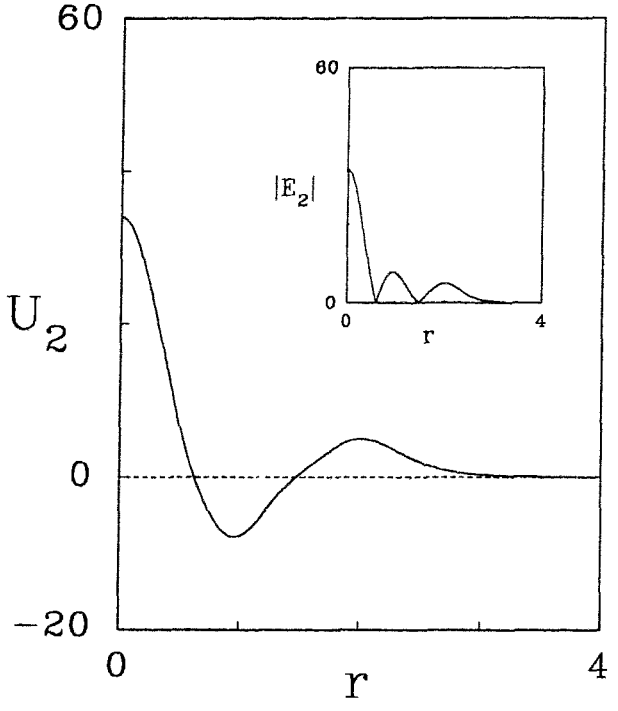

Figure 6.13: Radial field profiles of the $\beta = 6$ two-halo state. Inset: Corresponding $|E|$ curve.

consistently dominates the one-halo evolution.

6.5 The plot thickens: two-halo analysis

To conclude this chapter, let us consider the more complicated two-halo case. As a concrete example, Figure 6.13 depicts the radial field profiles for $\beta = 6$. Carrying out a procedure similar to that performed for the one-halo case, the growth rate curves as determined by numerical linear stability analysis are plotted in Figure 6.14.

The first striking feature of this plot is that in moving from the single-halo case to dual-halo profiles, a significant increase in the number of unstable modes occurs. For the $\beta = 6$ case indicated by the vertical dashed line, at first glance one might infer that this state will simply be dominated by a Y_6^m instability; in fact, the dynamics are somewhat more complicated. Recall that in the single-halo case, we observed that $g(r)$ was localized at the radius of the first halo. With two halos present, knowledge of the localization of the various radial perturbation functions is crucial to an understanding of the dynamics of the inner and outer halos. In order of decreasing size, Figure 6.15

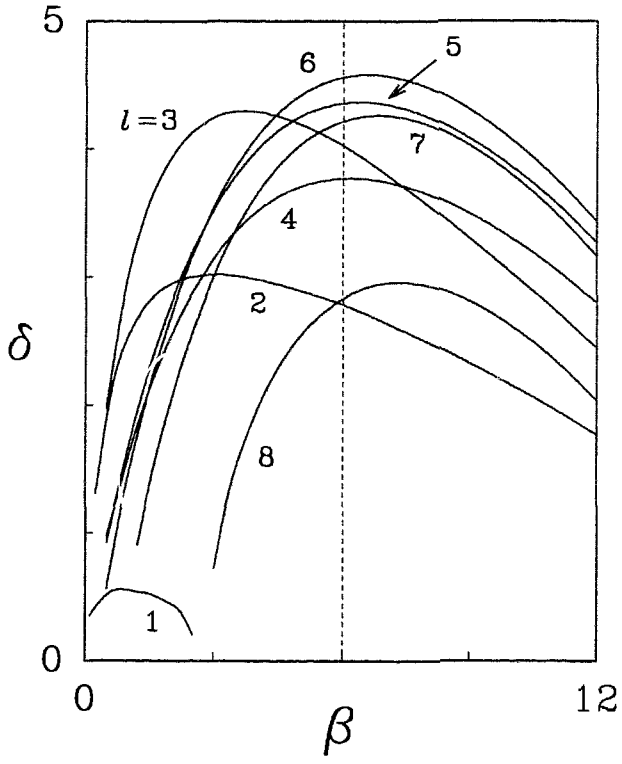

Figure 6.14: Summary of unstable growth rates for all two-halo bullets. The vertical dashed line indicates the $\beta = 6$ profile of Figure 6.13. (The horizontal scale stops at $\beta = 12$ to facilitate viewing of the various growth rate curves.)

shows the normalized $g(r)$ of the four largest growth modes. The largest three radial eigenmodes are all localized about the outer halo and have negligible effect on both the inner halo and the central core. The first growth mode that does effect the inner halo is the familiar $\ell = 3$ mode. We therefore expect markedly different behaviour for the inner and outer shells, these halos displaying a Y_3^m and Y_6^m type instability respectively.

Figure 6.16 shows the result of numerically propagating the $\beta = 6$ two-halo state in the presence of a small amount of numerical noise at six interesting stages of the evolution. In frame (a), an octant has been removed in order to visualize both the central core and the inner halo. Between $z = 0$ and $z = 1.3$ (not shown), little change occurs in the initial two-halo state. By frame (b), the outer halo has decomposed into what looks like a "soccer ball," the faces of this structure having an apparent hexagonal symmetry. Note, however, that although the symmetry breaking of the outer halo is well advanced, the spherical inner shell is still intact. By frame (c), the soccer-ball has completely disintegrated resulting in the formation of a multitude

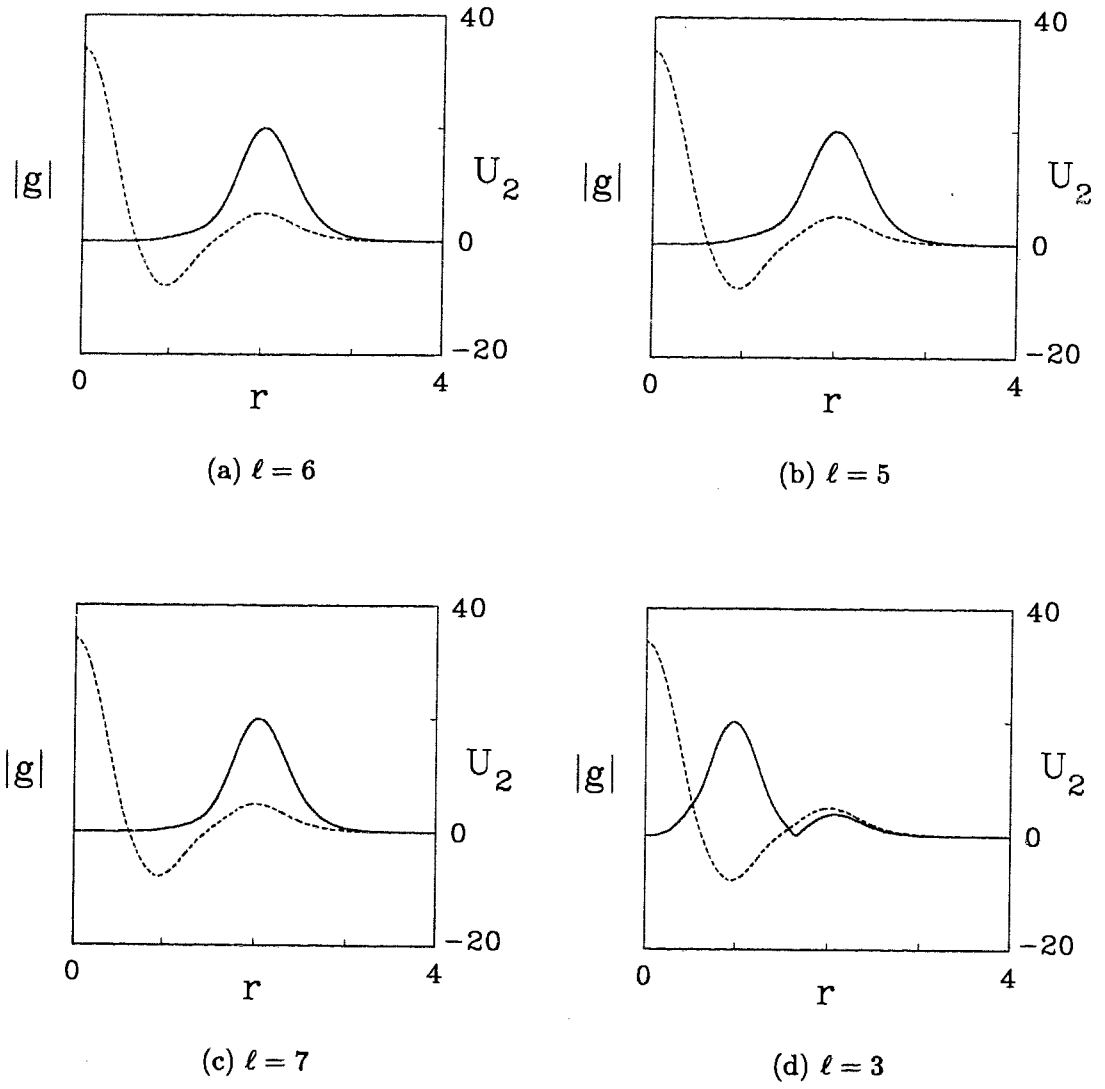

Figure 6.15: Solid curves: calculated radial perturbation functions of the four largest growth modes for the $\beta = 6$ two-halo case. Dashed curves: $U_2(r)$ profile.

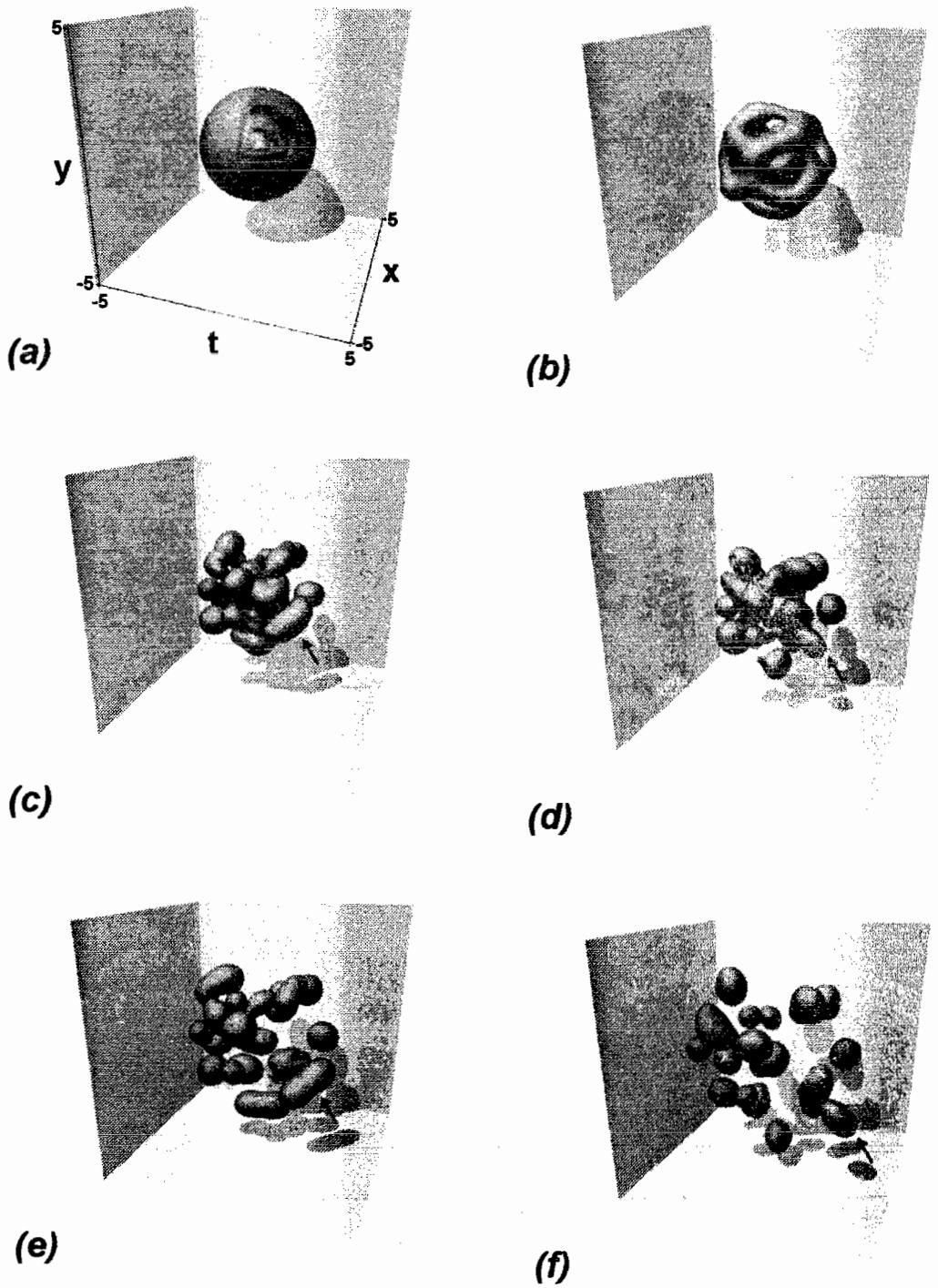

Figure 6.16: Simulation of the $\beta = 6$, $n = 2$ halo state. (a) $z = 0$, (b) $z = 1.95$, (c) $z = 2.20$, (d) $z = 2.40$, (e) $z = 2.85$ and (f) $z = 3.30$. Peak $|E| = 33.9$.

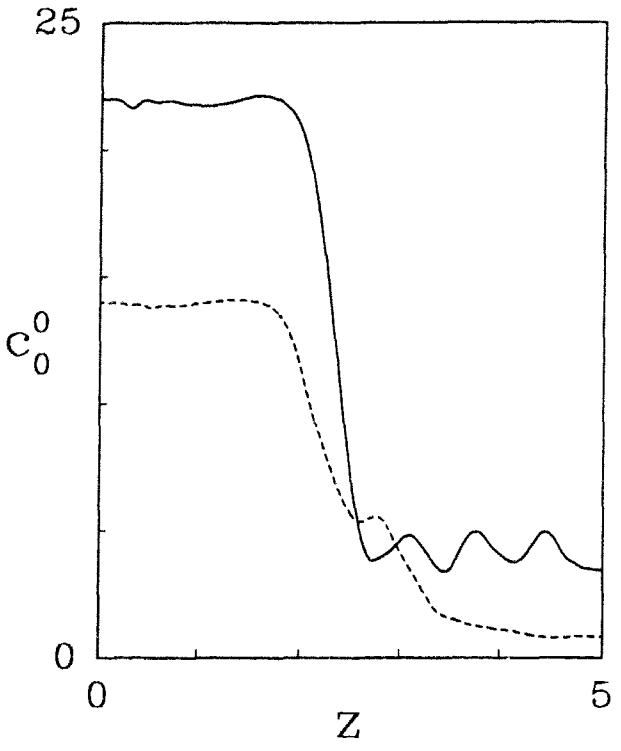

Figure 6.17: Harmonic content of the DC component. Solid curve: inner halo at $r^* = 0.95$. Dashed curve: outer halo at $r^* = 2.0$.

of interacting light bullets moving radially outwards towards the mesh boundaries; meanwhile, the decomposition of the inner halo is well underway. In the remaining frames, the decay continues and all resemblance to the initial state is lost as the bullets fly apart while undergoing complicated dynamical interactions.

As an aside unrelated to our analysis (which will only be able to predict the symmetry of the initial decay), consider the two fusing bullets indicated by the arrow in frame (c). By frame (d), these overlapping envelopes have apparently coalesced to form a single pulse. However, in frame (e) the original states reemerge, this oscillatory behaviour analogous to one-dimensional breather modes repeating two complete periods before the simulation terminates.

In Figure 6.17, the harmonic content of the DC mode at the radius of both halos is plotted versus the propagation distance revealing that beyond $z = 2.0$, the energy content drops off quickly as the decomposing shells move outwards.

Let us begin by considering the outer halo. Figure 6.18 is a volume rendered image corresponding to frame (b) but with the inner shell and central core removed, allowing us to peer through to the opposite side of this remarkable structure. The z evolution

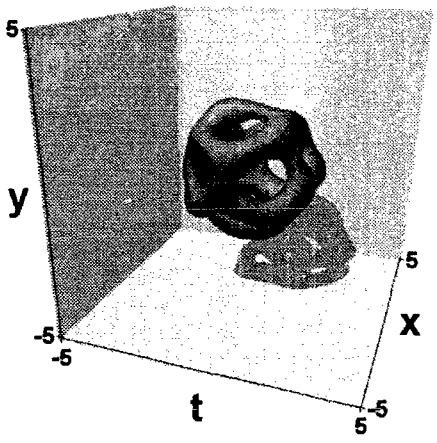

Figure 6.18: Volume rendering corresponding to frame (b) of Figure 6.16 with the inner halo and central core removed.

of the harmonic components is depicted in Figure 6.19 where the symmetry axis defining the north-pole has been taken to pierce through the middle of the gap in the hexagon closest to the front-right corner of the image. As predicted by our numerical stability analysis, the two largest components present are members of the $\ell = 6$ family of modes, the large Y_6^5 component resulting in the observed hexagonal pattern. Unfortunately, this state possesses other sizeable harmonic components making a pictorial comparison analogous to that presented for the one-halo case (where we observed a single dominant mode) difficult. In addition, while the modal analysis corroborates the theoretical prediction in terms of the specific dominant family of modes, we had no *a priori* knowledge that a hexagonal structure would form. This is in marked contrast to Soto-Crespo *et al.*'s two-dimensional problem where specific predictions could be made about the final outcome.

Finally, Figure 6.20 depicts the spherical harmonic analysis at the radius of the inner halo where the symmetry axis has been chosen to pierce the evolving tube structure in the usual way (not shown). As expected, the inner halo is dominated by the $\ell = 3$ family of modes, the sizeable Y_3^3 component revealing that the torus is pinched symmetrically as it forms at three equispaced azimuthal angles.

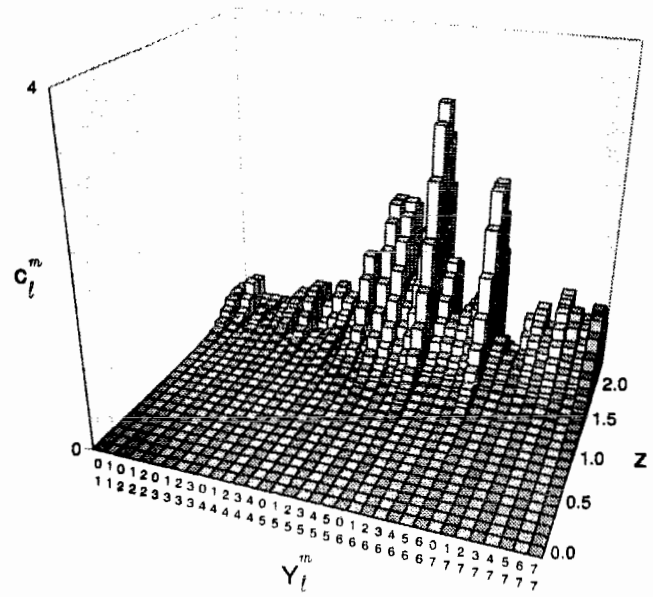

Figure 6.19: z evolution of the spherical harmonic components for the outer halo (rotated pole).

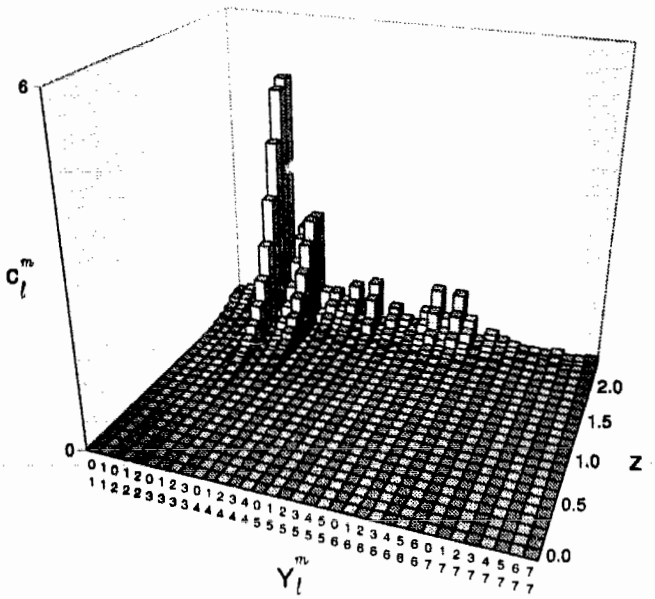

Figure 6.20: z evolution of the spherical harmonic components for the inner halo (rotated pole).

Chapter 7

Conclusions

In this thesis, we have considered spherical solitary wave solutions to the (3+1)-dimensional generalized nonlinear Schrödinger equation (GNLSE)

$$i\frac{\partial E}{\partial z} + \frac{1}{2}\nabla^2 E + f(I=|E|^2)E = 0$$

which governs the propagation of picosecond timescale plane-polarized optical envelopes in a bulk anomalously dispersive medium possessing an intensity dependent refractive index $f(I)$.

Making use of the simple stability criterion that the solitary wave's propagation constant reside on a positive slope branch of the associated energy curve, three saturable models were introduced and, through extensive numerical simulations, subsequently shown to support stable non-diffracting non-dispersing self-trapped pulses - light bullets.

A number of novel collision simulations were presented including soliton tunnelling, spiralling light bullets, and soliton fusion. These results, several of which have no one-dimensional analogue, serve to emphasize the inherent richness of the previously unexplored light bullet problem.

Of special interest are repulsive collisions at non-zero impact parameter between bullets possessing a π mutual phase difference. For the case of a simple saturable model, a comprehensive set of such scattering simulations acted as a probe of the

interaction potential, allowing us to determine the precise structure of the force law under the valid assumption of elastic scattering. The interaction potential was found to be of the Yukawa form which is consistent with an asymptotic expansion of the light bullet radial profile. Furthermore, the scattering data was found to scale correctly with velocity and the energy content was shown to play the role of an effective mass with the caveat that there exists a minimum energy for light bullet formation.

More of a theoretical curiosity than of practical importance, in Chapter 6 we considered the stability of the so-called spherical halo states of the GNLSE. That is, in addition to the regular Gaussian-like profiles discussed above, there exist higher bound states consisting of a central core surrounded by a number of bright spherical shells. A linear stability analysis in terms of spherical harmonic modes predicted these solitary wave solutions to be transversely unstable and we hypothesized that the growth and symmetry of the broken state would be dominated by the largest exponentially unstable family of modes. These predictions were corroborated by direct simulation of the GNLSE for both one and two-halo profiles.

To conclude, we wish to stress the following two recurrent themes. First, while the refractive index models studied are quantitatively dissimilar - possessing only the common trait of saturation - the qualitative simulation results appear to be largely model independent. Thus, the applicability of this research does *not* rely on the existence of a single exotic material possessing a very specific nonlinear refractive index. Second, light bullets appear to be extremely stable entities, often succeeding in surviving massive perturbations in the form of collisions. When quasi-soliton behaviour does not occur, one typically finds that a *new* soliton state is reached rather than a dispersal of the original confined energy into the surrounding volume. This behaviour is closely tied to the natural tendency of saturable media to form light bullets given sufficient localization of energy. (Dramatic evidence for this assertion include the switching between bistable soliton states achieved via amplification in Chapter 4 and the formation of a multitude of light bullets during decay of the halo state solutions of Chapter 6.) Thus, practically, it is often *not* necessary to begin with an exact solitary wave profile, light bullets acting as attractor states in the space of all possible envelope functions.

Our understanding of three-dimensional self-trapped pulses - light bullets - has progressed enormously over the past five years, from a flippant conjecture to the optimistic suggestion that they form the fundamental building block of an all-optical digital switch. As of the writing of this thesis, however, they remain a theoretical prediction, unverified by experiment.

Bibliography

[Ag89] G. P. Agrawal. *Nonlinear Fiber Optics* (Academic Press, San Diego, 1989).

[Ai90] J. S. Aitchison, Y. Silberberg, A. M. Weiner, D. E. Leaird, M. K. Oliver, J. L. Jackel, E. M. Vogel, and P. W. E. Smith, "Spatial optical solitons in planar glass waveguides," J. Opt. Soc. Amer. B **8**, 1290 (1990).

[Ak92] N. N. Akhmediev, V. I. Korneev, and R. F. Nabiev, "Modulation instability of the ground state of the nonlinear wave equation: optical machine gun," Opt. Lett. **15**, 393 (1992).

[Ak93a] N. N. Akhmediev and J. M. Soto-Crespo, "Generation of a train of three-dimensional optical solitons in a self-focusing medium," Phys. Rev. A **47**, 1358 (1993).

[Ak93b] N. N. Akhmediev, A. Ankiewicz, and J. M. Soto-Crespo, "Does the nonlinear Schrödinger equation correctly describe beam propagation?" Opt. Lett. **18**, 411 (1993).

[An86] S. V. Antipov, M. V. Nezlin, E. N. Snezhkin, and A. S. Trubnikov, "Rossby autosoliton and stationary model of the Jovian Great Red Spot," Science **323**, 238 (1986).

[At94] J. Atai, Y. Chen, and J. M. Soto-Crespo, "Stability of three-dimensional self-trapped beams with a dark spot surrounded by bright rings of varying intensity," Phys. Rev. A **49**, R3170 (1994).

[Ba85] A. Barthelemy, S. Maneuf, and C. Froehly, "Propagation soliton et auto-confinement de faisceaux laser par non linearité optique de Kerr," Optics Commun. **55**, 201 (1985).

[Ba95] S. Baluschev, A. Dreischuh, I. Velchev, S. Dinev, and O. Marazov, "Odd and even two-dimensional dark spatial solitons," Appl. Phys. B. **61**, 121 (1995).

[Bl91] A. B. Blagoeva, S. G. Dinev, A. A. Dreischuh, and A. Naidenov, "Light bullet formation in bulk media," IEEE J. Quantum Electron. **QE-27**, 2060 (1991).

[Bo92] R. W. Boyd. *Nonlinear Optics* (Academic Press, Boston, 1992).

[Ca91] T. Catunda, A. M. Cansian, and J. C. Castro, "Saturation effects in degenerate four-wave mixing in ruby and $GdAlO_3$:Cr^{+3}," J. Opt. Soc. Amer. B **8**, 821 (1991).

[Ch64] R. Y. Chiao, E. Garmire, and C. H. Townes, "Self-trapping of optical beams," Phys. Rev. Lett. **13**, 479 (1964).

[Ch66] R. Y. Chiao, M. A. Johnson, S. Krinsky, H. A. Smith, C. H. Townes, and E. Garmire, "6A1 - a new class of trapped light filaments," IEEE J. Quantum Electron. **QE-2**, 467 (1966).

[Ch95] Y. Chen and J. Atai, "Dark optical bullets in light self-trapping," Opt. Lett. **20**, 133 (1995).

[Co65] J. W. Cooley and J. W. Tukey, "An algorithm for machine computation of complex Fourier series," Math. Comput. **19**, 297 (1965).

[Co91] J. L. Coutaz and M. Kull, "Saturation of the nonlinear index of refraction in semiconductor-doped glass," J. Opt. Soc. Amer. B **8**, 95 (1991).

[Cr94] L. Cruzeiro-Hansson, "Two reasons why the Davydov soliton may be thermally stable after all," Phys. Rev. Lett. **73**, 2927 (1994).

[Ed92] D. E. Edmundson and R. H. Enns, "Bistable light bullets," Opt. Lett. **17**, 586 (1992).

[Ed93] D. E. Edmundson and R. H. Enns, "Fully 3-dimensional collisions of bistable light bullets," Opt. Lett. **18**, 1609 (1993).

[Ed95] D. E. Edmundson and R. H. Enns, "Particle-like nature of colliding 3-dimensional optical solitons," Phys. Rev. A **51**, 2491 (1995).

[Ed96] D. E. Edmundson, "Unstable spherical halo states of a 3-dimensional nonlinear Schrödinger equation," Phys. Rev. A. (submitted for publication).

[Ei93] S. L. Eix and R. H. Enns, "Optical switching between bistable soliton states of the second kind," Phys. Rev. A **47**, 5009 (1993).

[Ei96] S. L. Eix and R. H. Enns, "Bistable optical soliton logic gates," J. Opt. Soc. Amer. B. (submitted for publication).

[Em87] P. Emplit, J. P. Hamaide, F. Reynaud, C. Froehly, and A. Barthelemy, "Picosecond steps and dark pulses through nonlinear single mode fibers," Optics Commun. **62**, 374 (1987).

[En87a] R. H. Enns, S. S. Rangnekar, and A. E. Kaplan, "'Robust' bistable solitons of the highly nonlinear Schrödinger equation," Phys. Rev. A **35**, 466 (1987).

[En87b] R. H. Enns, S.S. Rangnekar, and A. E. Kaplan, "Bistable soliton pulse propagation: stability aspects," Phys. Rev. A **36**, 1270 (1987).

[En89] R. H. Enns and L. J. Mulder, "Bistable holes in nonlinear optical fibers," Opt. Lett. **14**, 509 (1989).

[En92a] R. H. Enns and S. S. Rangnekar, "Bistable spheroidal optical solitons," Phys. Rev. A **45**, 3354 (1992).

[En92b] R. H. Enns, D. E. Edmundson, S. S. Rangnekar, and A. E. Kaplan, "Optical switching between bistable soliton states: a theoretical review," Opt. and Quantum Electron. **24**, S1295 (1992).

[En93] R. H. Enns and D. E. Edmundson, "Guide to fabricating bistable soliton supporting media," Phys. Rev. A **47**, 4524 (1993).

[Fe78] M. D. Feit and J. A. Fleck, Jr., "Light propagation in graded-index optical fibers," Appl. Opt. **17**, 3990 (1978).

[Fe88] M. D. Feit and J. A. Fleck, Jr., "Beam nonparaxiality, filament formation, and beam breakup in the self-focusing of optical beams," J. Opt. Soc. Amer. B **5**, 633 (1988).

[Fo92] J. Ford, "The Ferma-Pasta-Ulam problem: paradox turns discovery," Physics Reports **213**, 271 (1992).

[Ga67] C. S. Gardner, J. M. Greene, M. D. Kruskal, and R. M. Miura, "Method for solving the Korteweg-de Vries equation," Phys. Rev. Lett. **19**, 1095 (1967).

[Ga91] S. Gatz and J. Herrmann, "Soliton propagation in materials with saturable nonlinearity," J. Opt. Soc. Amer. B **8**, 2296 (1991).

[Go83] J. P. Gordon, "Interaction forces among solitons in optical fibers," Opt. Lett. **8**, 596 (1983).

[Go86] J. P. Gordon, "Theory of the soliton self-frequency shift," Opt. Lett. **11**, 662 (1986).

[Ha73a] A. Hasegawa and F. Tappert, "Transmission of stationary nonlinear optical pulses in dispersive dielectric fibers. I. Anomalous dispersion," Appl. Phys. Lett. **23**, 142 (1973).

[Ha73b] A. Hasegawa and F. Tappert, "Transmission of stationary nonlinear optical pulses in dispersive dielectric fibers. II. Normal dispersion," Appl. Phys. Lett. **23**, 171 (1973).

[Ha92] K. Hayata and M. Koshiba, "Solution of self-trapped multidimensional optical beams by Galerkin's method," Opt. Lett. **17**, 841 (1992).

[Ha93] K. Hayata and M. Koshiba, "Bright-dark solitary wave solutions of a multi-dimensional nonlinear Schrödinger equation," Phys. Rev. E **48**, 2312 (1993).

[In90] E. Infeld and G. Rowlands. *Nonlinear Waves, Solitons and Chaos* (Cambridge University Press, Cambridge, 1990).

[Is81] M. Israeli and S. Orszag, "Approximation of radiation boundary conditions," J. Comput. Phys. **41**, 115 (1981).

[Ka75] P. K. Kaw, K. Nishikawa, Y. Yoshida, and A. Hasegawa, "Two-dimensional and three-dimensional envelope solitons," Phys. Rev. Lett. **35**, 88 (1975).

[Ka85a] A. E. Kaplan, "Bistable solitons," Phys. Rev. Lett. **55**, 1291 (1985).

[Ka85b] A. E. Kaplan, "Multistable self-trapping of light and multistable soliton pulse propagation," IEEE J. Quantum Electron. **QE-21**, 1538 (1985).

[Ke65] P. L. Kelley, "Self-focusing of optical beams," Phys. Rev. Lett. **15**, 1005 (1965).

[Ki93] Y. S. Kivshar, "Dark solitons in nonlinear optics," IEEE J. Quantum Electron. **QE-28**, 250 (1993).

[Ki94] Y. S. Kivshar and X. Yang, "Ring dark solitons," Phys. Rev. E **50**, R40 (1994).

[Ko73] A. A. Kolokolov, "Stability of the dominant mode of the nonlinear wave equation in a cubic medium," J. Appl. Mech. Tech. Phys. **3**, 426 (1973).

[Ko75] A. A. Kolokolov and A. I. Sykov, "Instability in the higher modes of a nonlinear equation," J. Appl. Mech. Tech. Phys. **4**, 519 (1975).

[Ko87] Y. Kodama and A. Hasegawa, "Nonlinear pulse propagation in a monomode dielectric guide," IEEE J. Quantum Electron. **QE-23**, 510 (1987).

[Kr88] D. Krokel, N. J. Halas, G. Giuliani, and D. Grischkowsky, "Dark-pulse propagation in optical fibers," Phys. Rev. Lett. **60**, 29 (1988).

[Kr91] J. A. Krumshansl, "Unity in the science of physics," Physics Today. (March, 1991).

[Ku88] E. A. Kuznetsov and S. K. Turitsyn, "Instability and collapse of solitons in media with a defocusing nonlinearity," Sov. J. Theor. Phys. JETP **67**, 1583 (1988).

[La84] E. W. Laedke and K. H. Spatschek, "Stable three-dimensional envelope solitons," Phys. Rev. Lett. **52**, 279 (1984).

[La93] C. T. Law and G. A. Swartzlander, Jr., "Optical vortex solitons and the stability of dark soliton stripes," Opt. Lett. **18**, 586 (1993).

[La94] B. L. Lawrence, M. Cha, W. E. Toruellas, G. I. Stegeman, S. Etemad, G. Baker, and F. Kajzar, "Measurement of the complex nonlinear refractive index of single crystal *p*-toluene sulfonate at 1064 nm," Appl. Phys. Lett. **64**, 2773 (1994).

[Ma70] J. B. Marion. *Classical Dynamics of Particles and Systems* (Academic Press, Orlando, 2nd edition, 1970).

[Ma74] S. Maxon and J. Viecelli, "Spherical solitons," Phys. Rev. Lett. **32**, 4 (1974).

[Ma88a] S. Maneuf, R. Desailly, and C. Froehly, "Stable self-trapping of laser beams: observations in a nonlinear planar waveguide," Optics Commun. **65**, 193 (1988).

[Ma88b] S. Maneuf and F. Reynaud, "Quasi-steady state self-trapping of first, second, and third order sub-nanosecond soliton beams," Optics Commun. **66**, 325 (1988).

[Ma88c] J. T. Manassah, P. L. Baldeck, and R. R. Alfano, "Self-focusing, self-phase modulation, and diffraction in bulk homogeneous material," Opt. Lett. **13**, 1090 (1988).

[Mc93] G. S. McDonald, K. S. Syed, and W. J. Firth, "Dark spatial soliton break-up in the transverse plane," Optics Commun. **95**, 281 (1993).

[Mc95] R. McLeod, K. Wagner, and S. Blair, "(3+1)-dimensional optical soliton dragging logic," Phys. Rev. A **52**, 3254 (1995).

[Mo80] L. F. Mollenauer, R. H. Stolen, and J. P. Gordon, "Experimental observation of picosecond pulse narrowing and solitons in optical fibers," Phys. Rev. Lett. **45**, 1095 (1980).

[Mo88] L. F. Mollenauer, M. J. Neubelt, S. G. Evangelides, J. P. Gordon, J. R. Simpson, and L. G. Cohen, "Experimental study of soliton transmission over more than 10,000 km in dispersion-shifted fibers," Opt. Lett. **15**, 1203 (1988).

[Ne92] A. C. Newell and J. V. Moloney. *Nonlinear Optics* (Addison-Wesley, Redwood City, California, 1992).

[Pi74] A. H. Piekara, J. S. Moore, and M. S. Feld, "Analysis of self-trapping using the wave equation with high-order nonlinear electric permittivity," Phys. Rev. A **9**, 1403 (1974).

[Po91] L. Poladian, A. W. Snyder, and D. J. Mitchell, "Spiralling spatial solitons," Optics Commun. **85**, 59 (1991).

[Pr86] W. H. Press, B. P. Flannery, S. A. Teukolsky, and W. T. Vetterling. *Numerical Recipes* (Cambridge University Press, New York, 1986).

[Sc1845] J. Scott-Russell. Report on waves. In *British Assn. Adv. Sci. Report* (London, 1845).

[Se88] G. Sewell. *The Numerical Solution of Ordinary and Partial Differential Equations* (Academic Press, San Diego, 1988).

[Sh89] Y. R. Shen. Theory of self-phase modulation and spectral broadening. In *The Supercontinuum Laser Source* (R. R. Alfano, editor, Springer-Verlag, New York, 1989).

[Si90] Y. Silberberg, "Collapse of optical pulses," Opt. Lett. **15**, 1282 (1990).

[Sn91] A. W. Snyder, D. J. Mitchell, L. Poladian, and F. Ladouceur, "Self-induced optical fibers: spatial solitary waves," Opt. Lett. **16**, 21 (1991).

[Sn92] A. W. Snyder, L. Poladian, and D. J. Mitchell, "Stable black self-guided beams of circular symmetry in a bulk Kerr medium," Opt. Lett. **17**, 789 (1992).

[Sn93] A. W. Snyder, D. J. Mitchell, and B. Luther-Davies, "Dark spatial solitons constructed from modes of linear waveguides," J. Opt. Soc. Amer. B **10**, 2341 (1993).

[Sn95] A. W. Snyder, D. J. Mitchell, and Y. S. Kivshar, "Unification of linear and nonlinear wave optics," Mod. Phys. Lett. B **9**, 1479 (1995).

[So91] J. M. Soto-Crespo, D. R. Heatley, E. M. Wright, and N. N. Akhmediev, "Stability of the higher-bound states in a saturable self-focusing medium," Phys. Rev. A **44**, 636 (1991).

[Sw91] G. A. Swartzlander, Jr., D. R. Andersen, J. J. Regan, and A. E. Kaplan, "Spatial dark-soliton stripes and grids in self-defocusing materials," Phys. Rev. Lett. **66**, 1583 (1991).

[Sw92] G. A. Swartzlander, Jr. and C. T. Law, "Optical vortex solitons observed in Kerr nonlinear media," Phys. Rev. Lett. **69**, 2503 (1992).

[Ta65] V. I. Talanov, "Self-focusing of wave beams in nonlinear media," Sov. J. Theor. Phys. JETP Lett. **2**, 138 (1965).

[Ta84] T. R. Taha and M. J. Ablowitz, "Analytical and numerical aspects of certain nonlinear evolution equations. II. Numerical, nonlinear Schrödinger equation," J. Comput. Phys. **55**, 203 (1984).

[We88] A. M. Weiner, J. P. Heritage, R. J. Hawkins, R. N. Thurston, E. M. Kirschner, D. E. Leaird, and W. J. Tomlinson, "Experimental observation of the fundemental dark soliton in optical fibers," Phys. Rev. Lett. **61**, 2445 (1988).

[Wi75] J. Z. Wilcox and T. J. Wilcox, "Stability of localized plasma model in two and three dimensions," Phys. Rev. Lett. **34**, 1160 (1975).

[Za65] N. J. Zabusky and M. D. Kruskal, "Interaction of 'solitons' in a collisionless plasma and the recurrence of initial states," Phys. Rev. Lett. **15**, 240 (1965).

[Za66] V. E. Zakharov. *On the nonlinear theory of surface waves.* (PhD thesis, Institute of Nuclear Physics, Siberian Division, USSR Academy of Sciences, 1966).

[Za72] V. E. Zakharov and A. B. Shabat, "Exact theory of two-dimensional self-focusing and one-dimensional self-modulation of waves in nonlinear media," Sov. J. Theor. Phys. JETP **34**, 62 (1972).

[Za73] V. E. Zakharov and A. B. Shabat, "Interaction of solitons in a stable medium," Sov. J. Theor. Phys. JETP **37**, 823 (1973).